Numerical modelling of dynamic continental collision: quantifying the slab rollback orogeny model for the Central Alps

Luuk van Agtmaal – 6377076

Master Thesis Earth Sciences

Utrecht University

Supervised by: Dr. Y. van Dinther
Second advisors: Dr. E. Willingshofer, Prof. Dr. L. Matenco

October 16, 2020

Abstract

The Central Alps are one of the continental collision zones that cannot be explained by conventional collision tectonics. The striking isostatic disequilibrium has inspired the formulation of the slab rollback orogeny (SRO) model. This concept revolves around the notion that vertical buoyancy forces dominate over horizontal forces. Recently it has been applied to the Central Alps in a mostly kinematic framework, but lacks supporting dynamic evidence. This research uses quantitative (seismo-)thermomechanical models of continental collision with a fixed lower plate to evaluate the SRO model, both in general terms and in application to the Central Alps. Specifically, the most important vertical and horizontal forces (i.e. slab pull and mantle tractions below the overriding plate) are monitored to explain the observed evolution of the collisional systems. The role of the lower continental crust in both continents is assessed as well in order to explore circumstances for lower crustal indentation as interpreted in the Central Alps.

Several models produce orogenic and sub-lithospheric architectures that resemble the Central Alps surprisingly well. The modelling results and dynamic analysis show that the SRO model underestimates the importance of mantle drag in driving motions of tectonic plates. Rollback after slab detachment does not occur, due to detachment-induced rebound and unbending of the slab which invariably generates mantle drag away from the trench. Extensive parameter studies revealed that ocean length and frictional strength ratios between various layers have a large influence on the modelling outcome. The lower crust of the overriding plate is found to be much more important than that of the down-going plate in controlling the geometry of the orogen. Indentation is favoured when the lithospheric mantle is somewhat weaker and the upper crust of the overriding plate decouples from its lower crust. These results demonstrate the effectiveness of thermo-mechanical models in producing structures similar to those observed in nature. Furthermore, they provide important insights into the parameters that control their development and they can be used to quantify the forces that effectuate the structures.

Contents

List of Figures

List of Tables

1 Introduction

The origin of the Central Alps has been a highly active area of research practically since the dawn of geology (e.g. Bonney, 1885; Argand, 1916). What started with descriptive field geology has evolved towards detailed geologic and tectonic maps (e.g. Schmid et al., 1996; Bousquet et al., 2012; Schmid et al., 2017; Van Hinsbergen et al., 2020, and Figure 1). These partly inspired the development of numerical geodynamic models of continental collision, because knowledge was insufficient to explain the geological features these tectonic maps presented.

Since the late seventies, such geodynamic numerical models have progressed to near-realistic levels of detail, having much in common with interpreted geological cross-sections (such as Dal Zilio et al., 2020; Liao et al., 2018; Duretz et al., 2011; Liao and Gerya, 2017; Vogt et al., 2017; Duretz et al., 2012; Duretz and Gerya, 2013; Duretz et al., 2014). Many of these models use the marker-in-cell approach with finite differences (Gerya, 2019, and references therein). In addition to numerical methods, continental collision has been the subject of analogue modelling studies as well ((For a review, see e.g. Graveleau et al., 2012). One advantage of those is the use of real physical materials. Both analogue and numerical models have significantly improved the understanding of the mechanisms and processes involved in continental collision. For example, slab dynamics have been extensively studied in recent years (Duretz et al., 2011, 2012; Duretz and Gerya, 2013; Duretz et al., 2014; Schellart and Moresi, 2013; Baumann et al., 2010; Andrews and Billen, 2009; Gerya et al., 2004a; Luth et al., 2013). Coupling between crustal layers, the crust and mantle and across the plate boundary have been actively researched as well (Gerbault and Willingshofer, 2004; Sokoutis and Willingshofer, 2011; Willingshofer and Sokoutis, 2009; Luth et al., 2010; Vogt et al., 2018). Nonetheless, much is still unknown about interactions between such processes. Changing one parameter can invoke complex feedback mechanisms that can result in surprising and counter-intuitive results. For instance, lower crustal indentation can still occur when it is rheologically weak (Gerbault and Willingshofer, 2004).

One of the main assumptions of plate tectonic theory is that far-field horizontal forces drive continental collision. This is expressed in models as constant prescribed convergence of continental plates (e.g. Beaumont et al., 1994; Vogt et al., 2017, 2018; Brouwer et al., 2004). While this classical continental collision theory with dominant horizontal forces applies well to some orogens, other mountain chains such as the Central Alps do not fit well into this theory. The Moho below the Central Alps is located quite deep, up to 60 km below the surface (e.g. Lombardi et al., 2008, and Figure 2) which is in agreement with thermo-rheological models (Vigano and Martin, 2007). This thick crustal root is accompanied by an average surface topography of 2 km and a maximum elevation of 4 km (Kissling and Schlunegger, 2018; Dal Zilio et al., 2020). Isostatic balancing revealed that the observed Moho depth would require double the present average surface elevation (Schlunegger and Kissling, 2015). Thus, the Central Alps are in isostatic disequilibrium.

These observations have led to the proposition of a new theoretical orogenesis model in which vertical instead of horizontal forces have the most considerable effects on the evolution of the orogen (Schlunegger and Kissling, 2015; Kissling and Schlunegger, 2018). This model is commonly referred to as the slab rollback orogeny (SRO) model. Recently, Dal Zilio et al. (2020) initiated a discussion of this model in a dynamic context and applied it to the Central Alps case. However, their results do not yet explain how the Adriatic lower crust can indent the Eurasian upper crust as shown in geological cross-sections through the Central Alps (Figure 2). This is counter-intuitive as lower continental crust is usually weak and ductile (e.g. Sokoutis and Willingshofer, 2011; Willingshofer and Sokoutis, 2009; Vigano and Martin, 2007) and would be more likely to flow into the orogenic core than rigidly indent it.

Previous studies have focused more on the role of the upper crust (e.g. Vogt et al., 2017; Liao and Gerya, 2017), although some have investigated the role of the lower crust (Faccenda et al., 2008). Others varied both the upper and lower crust simulataneously (Vogt et al., 2018). However, each of those studies used a kinematic modelling approach. The (semi-)dynamic approach (as in Duretz et al., 2011) used in this thesis provides an excellent opportunity to look into this more dynamically. To properly evaluate and understand the SRO model a more satisfying quantification of the SRO model in combination with a more extensive parameter study to explore the feasibility and likelihood of the SRO model are necessary. This way claims about the relative importance forces can finally be supported or disproved by dynamic analysis. This will contribute towards resolving the recent debate about the long-discussed evolution of the Central Alps.

This research aims to evaluate the SRO model by quantifying and analysing the most important horizontal and vertical forces (i.e. mantle drag (Alvarez, 2010) and slab pull (Kissling and Schlunegger, 2018)) in 2D

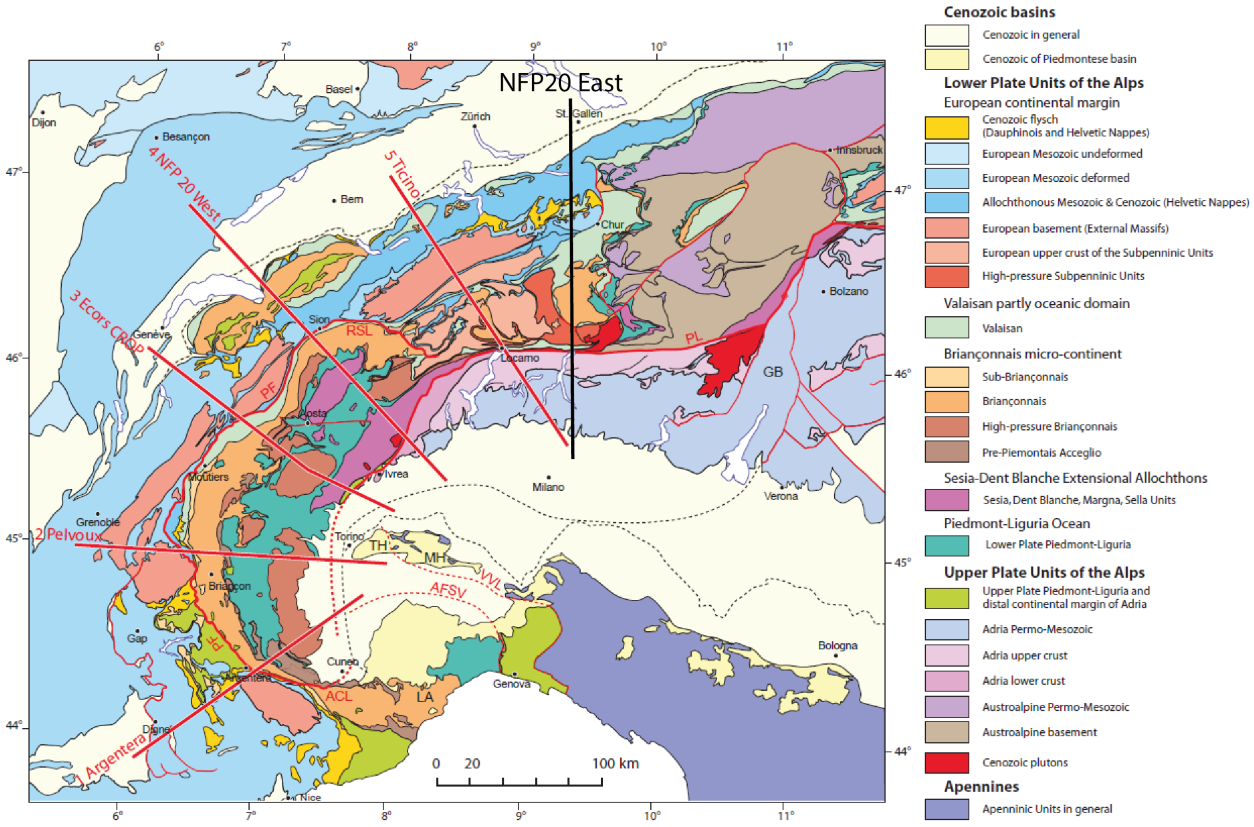

Figure 1: Tectonic map of the Western and Central Alps, after Schmid et al. (2017). North of the Periadriatic lineament are the Eurasian (lower plate) units, while the Adriatic (upper plate) units are found to the south. Note the remnants of the Piedmont-Ligurian and Valais oceans that were closed during convergence. Transects NSF20 East and 5 are shown in Figures 2 and 3, respectively.

numerical models of dynamic continental collision. Since it has been applied to the Central Alps, the SRO model evaluation is performed in the context of the Central Alps. In the analysis special attention is given to the relative roles of the lower crust of both continents, as well as the occurrence of post-detachment slab rollback. Furthermore, a large set of parameter studies with respect to the reference model is set up to explore the parameter space under which the SRO model can work and to test its feasibility. Finally, this study attempts to address circumstances for lower crustal indentation and its relation to e.g. exhumation of crustal units of the downgoing plate.

The plate tectonic and geological setting of the Central Alps is briefly summarised in the next section. Thereafter the numerical and model setup will be laid out. The reference model is then described and analysed, followed by a relatively large number of parameter studies. In the discussion, the models will be compared with each other and with existing literature. Finally, an assessment will be made how the modelling results fit within the evolution of the Central Alps.

2 Geological setting

The European Alps form a relatively young collisional orogen located in Southern-Central Europe. In terms of geometry, it can be divided into three areas. The Western Alps curve 180 degrees around the Po basin in North-western Italy, while the Central and Eastern Alps run straight in a WSW-ENE orientation. In the Western and Central Alps (Figure 1), the Eurasian plate subducts beneath the overriding Adriatic plate at a rate of 0.1-0.2 cm/yr (Handy et al., 2010; von Hagke et al., 2014). The Central Alps consist of a double-vergent orogen with an average topography of 2 km (Figure 2a) and maximum elevation of about 4 km (Dal Zilio et al., 2020). At a crustal scale, imbricate backthrusts are found in the Adriatic upper crust, south of the Insubric line. North of this pronounced retro-shear, the nappe stack in the Eurasian upper crust is deformed by a large backfold (Schmid

et al., 2004). Further to the north, the Molasse basin forms the foreland basin of the Central Alps, while the Po plain is interpreted as a retro-foreland basin.

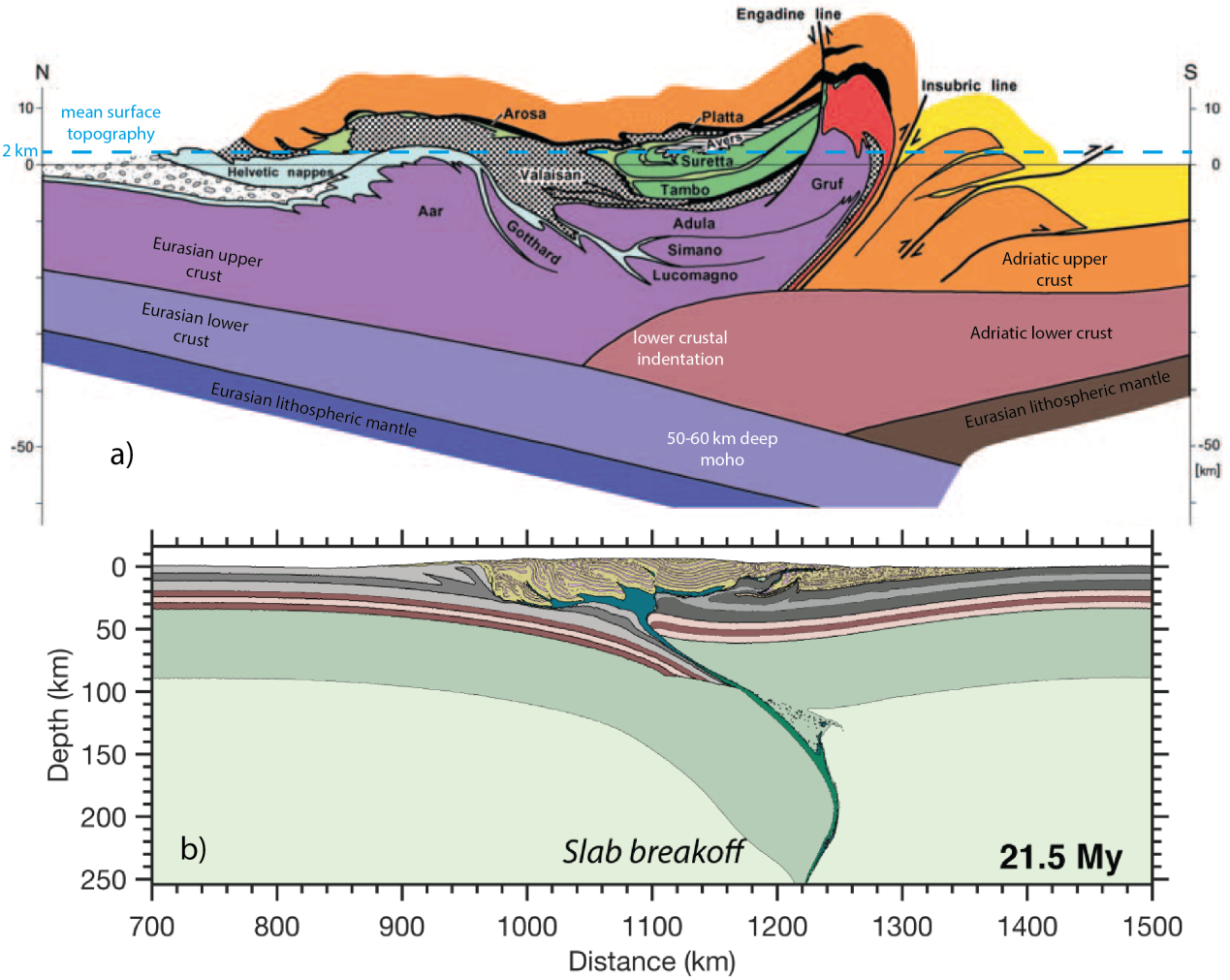

Figure 2: **a)** N-S geological cross-section through the Central Alps (including eroded units), modified from Schmid et al. (2004). **b)** Outcome of numerical modelling from Dal Zilio et al. (2020) showing slab detachment. The lower crust of the (tip of the) overriding plate is pushed upwards by the positive buoyancy exerted by the lower plate (Dal Zilio et al., 2020). The remains of the subducted oceanic plates separate the overriding from the down-going plate.

The NNW directed convergence between the Adriatic and Eurasian plate presumably occurred in several stages (Handy et al., 2010; Van Hinsbergen et al., 2020). Two partly or completely oceanic domains (the Piedmont-Ligurian and Valais), separated by one continental sliver, i.e. the Briançonnais unit was consumed during subduction. Most of the oceanic Piedmont-Ligurian units were subducted between 80-55 Ma, initially at a rate of 0.9 cm/yr and increasing to 1.5 cm/yr after 67 Ma. Parts of this oceanic domain did not subduct and are now observed as ophiolites in the highest parts of the Central and Western Alps (Van Hinsbergen et al., 2020; Handy et al., 2010). The subduction was 0.2 cm/yr faster than the Africa-Europe convergence, which is explained in part by rollback-induced suction at the plate interface. This is thought to have induced asthenospheric viscous mantle drag beneath Adria (Handy et al., 2010).

Subsequently, the Briançonnais continental sliver subducted between 55-45 Ma, followed by the Valais ocean in the period between 45-40 Ma (Van Hinsbergen et al., 2020). Thereafter, convergence was accommodated by continental subduction of the European passive margin, documented by the accretion of the Helvetic Nappes and External Massifs between 40-30 Ma. The onset of continental collision leading to a slowdown in subduction from 1.5 to 0.3 cm/yr occurred at about 35 Ma (Handy et al., 2010). Subduction of these units was succeeded by thrusting of the previously stacked continental and ophiolitic units over the Molasse foreland basin until 20 Ma, where the retro-wedge formed around 31-28 Ma (Rosenberg et al., 2015). After 20 Ma only minor (25 km)

N-S shortening occurred in the Western-Central Alps until present, which was taken up by the Molasse basin (Van Hinsbergen et al., 2020). At around 22-23 Ma the Adriatic lower crust started indenting the orogenic core (Malusà et al., 2016). Lower crustal indentation is more intense in the eastern Central Alps (70 km, Lombardi et al., 2008)) than in the western Central Alps where it is not present (Rosenberg and Kissling, 2013). This might be related to progressive curvature of the Western Alps (Van Hinsbergen et al., 2020; Handy et al., 2010) or interactions between European and Adriatic slabs (Malusà et al., 2016).

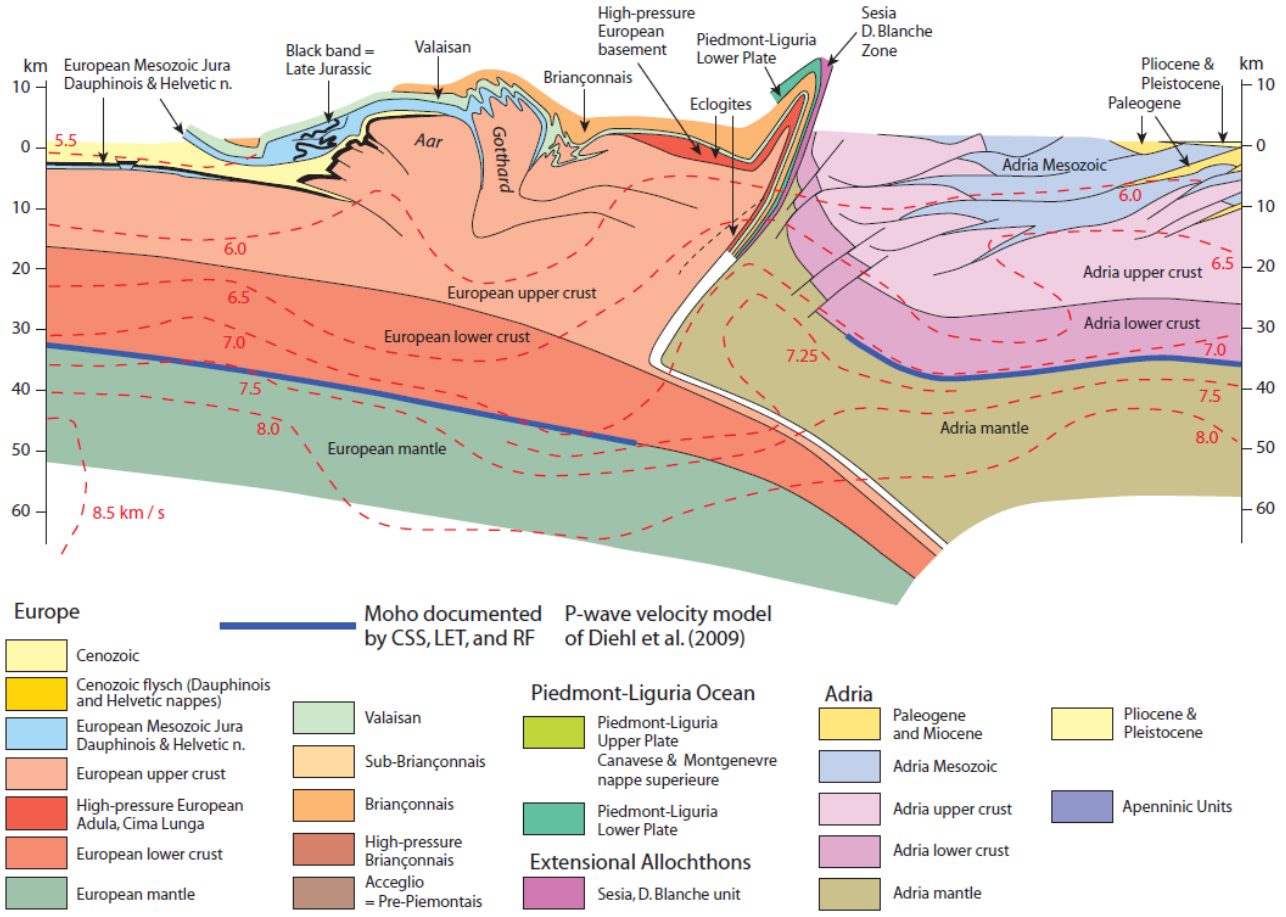

Figure 3: Transect 5 (Tincino transect) in Figure 1, modified after Schmid et al. (2017). Note the different location and orientation with respect to the NFP-20 East profile. The tip of the overriding plate is bent up in this cross-section, while it is straight in Figure 2. Furthermore, the Insubric line (here indicated as Sesia D. Blanche Zone) penetrates deeper than in the NFP-20 East profile

3 Methods

3.1 Numerical Setup

This research uses I2ELVIS (Gerya and Yuen, 2007) to simulate the long-term geodynamic evolution of two colliding continents. In addition, the seismo-thermo-mechanical approach is used (Dinther, 2013; Van Dinther et al., 2013; Dal Zilio et al., 2020) to incorporate short-term deformation in the reference model. I2ELVIS is the visco-elasto-plastic version of the thermo-mechanically coupled code I2VIS, which is even more widely used and benchmarked (Gerya and Yuen, 2003). Most of the numerical studies referenced in this research use either I2VIS (e.g. Gerya et al., 2004b; Burg and Gerya, 2005; Faccenda et al., 2008, 2009; Duretz et al., 2011; Duretz and Gerya, 2013; Duretz et al., 2012; Vogt et al., 2017, 2018; Liao and Gerya, 2017) or I2ELVIS code (Gerya et al., 2008) or even 3D versions (Liao et al., 2018).

The method is based on conservative finite differences within a combined Eulerian-Lagrangian reference frame. The Eulerian nodes are stationary and contain information used by numerous Lagrangian markers

that can move through this immobile grid (Gerya, 2019). The code can be used to solve the momentum and continuity equations, as well as the heat or temperature equation, on a fully staggered grid. The continuity equation for the mobile Lagrangian markers can be written as

$$\frac{D\rho}{Dt} + \rho\nabla \cdot \vec{v} = 0 \tag{1}$$

In this research, the medium is assumed to be incompressible, meaning that the temporal change of density of a Lagrangian marker is negligible (Gerya, 2019), i.e.

$$\frac{D\rho}{Dt} = \frac{\partial\rho}{\partial t} + \vec{v} \cdot \nabla(\rho) = 0 \tag{2}$$

.

This reduces equation 1 to

$$\nabla \cdot \vec{v} = \frac{\partial v_x}{\partial x} + \frac{\partial v_y}{\partial y} = 0 \tag{3}$$

for both the Lagrangian and the Eulerian cases. Whereas temporal change is ignored due to the incompressible flow approximation, the density is still temperature- and pressure-dependent as (Gerya, 2019)

$$\rho(T, z) = \rho_0 \cdot \frac{1 + \beta(P - P_0)}{1 + \alpha(T - T0)}. \tag{4}$$

Here the reference density ρ_0 is a material constant, P_0 is the reference pressure at the surface, i.e. 0.1 MPa, T_0 is a reference temperature (298.15°K). In addition, β and α represent thermal compressibility and expansivity coefficients in MPa/K and K^{-1}, respectively. Usually this ratio is slightly larger than 1, therefore density increases with depth.

The equation of motion, also known as the momentum equation, couples deformation to forces and works to conserve the momentum in the gravity field. Like the continuity equation, it has an expression for both Eulerian and Lagrangian points of reference, but the code uses the Eulerian expression:

$$\frac{\partial\sigma_{ij}}{\partial x_j} + \rho g_i = \rho\left(\frac{\partial v_i}{\partial t} + v_j\frac{\partial v_i}{\partial x_j}\right) \tag{5}$$

in the compact form. They can be written in full by inserting $i = x$, $j = x, y$ to get the x-momentum equation, and $i = y$, $j = x, y$ to obtain the y-momentum equation. From this general equation, the relationship between deviatoric and total stress is used to incorporate pressure (defined as mean stress) into the momentum equation such that it becomes the deviatoric Navier-Stokes equation of motion

$$\frac{\partial\sigma'_{ij}}{\partial x_j} - \frac{\partial P}{\partial x_i} + \rho g_i = \rho\frac{Dv_i}{Dt}, \tag{6}$$

where Dv_i/Dt stands for the material or substantive derivative of v_i, as in similar to equation 2. The inertial force on the right hand side of the Navier-Stokes equation of motion ($\rho Dv_i/Dt$) is ignored in I2(EL)VIS because the change of velocity with time in the mantle is over twenty orders of magnitude smaller than the ρg_i term (Gerya, 2019). However, in seismo-thermo-mechanical modelling this does not hold for short-term deformation. As such, the inertial term is included here. Moreover, the horizontal component of the gravity field is assumed to be zero. Therefore, the final forms of the x- and y-Navier-Stokes equations are written as (Dinther, 2013)

$$\frac{\partial\sigma'_{xx}}{\partial x} + \frac{\partial\sigma'_{xy}}{\partial y} - \frac{\partial P}{\partial x} = \rho\frac{Dv_x}{Dt} \tag{7}$$

$$\frac{\partial\sigma'_{yy}}{\partial y} + \frac{\partial\sigma'_{yx}}{\partial x} - \frac{\partial P}{\partial y} = \rho\frac{Dv_y}{Dt} - \rho g_y \tag{8}$$

which are identical to those used in (Dal Zilio et al., 2020). Equations 3, 7 and 8 are solved for the velocity components at each basic node. Subsequently, equations 7 and 8 are solved for pressure such that three variables are calculated from three equations.

Finally, conservation of heat is achieved through the temperature equation. The code uses its Lagrangian expression (Gerya and Yuen, 2007; Gerya, 2019)

$$\rho C_p \frac{DT}{Dt} = -\frac{\partial q_i}{\partial x_i} + H \tag{9}$$

where C_p is the material-dependent specific heat capacity, $q_i = -k\frac{\partial T}{\partial x_i}$ is the heat advection and H represents heat production terms, i.e. radiogenic heat production H_r which is constant for each material, shear heating H_s and adiabatic heating H_a. $DT/Dt = \partial T/\partial t + \vec{\nabla} \cdot \nabla T$ is the substantial time derivative of temperature. The shear heating term essentially converts mechanical energy to heat as materials deform in an inelastic manner and relates deviatoric stresses and strain rates as (Gerya, 2019)

$$H_s = \sigma'_{ij}\dot{\varepsilon}'_{ij}. \tag{10}$$

Adiabatic heating is produced by compression and decompression of a material and can therefore be negative as well as positive

$$H_a = T\alpha\frac{DP}{Dt} \tag{11}$$

For more details on the numerical methods, such as further argumentation behind the choice of equation forms, see (van Dinther et al., 2013) and (Gerya, 2019). The latter also describes in more detail how the equations are derived and solved, while the former contains details on the seismo-thermo-mechanical components. The thermo-mechanical part is also well documented in Gerya and Yuen (2007).

3.2 Rheology

To achieve a realistic representation of the deformation in the model rock units a visco-elasto-plastic rheology was adopted. This rheology is inserted into the conservation of mass and momentum equations through a time-dependent stress and density (Gerya and Yuen, 2007) which are locally calculated at each time step. The total (deviatoric) strain rates in the model are built up of viscous, elastic and plastic components

$$\dot{\varepsilon}'_{ij} = \dot{\varepsilon}'_{ij,visc} + \dot{\varepsilon}'_{ij,el} + \dot{\varepsilon}'_{ij,pl} \tag{12}$$

in which the various components are given by (Gerya, 2019)

$$\dot{\varepsilon}'_{ij(visc)} = \frac{\sigma'_{ij}}{2\eta} \tag{13}$$

$$\dot{\varepsilon}'_{ij(el)} = \frac{1}{2G}\frac{D\sigma'_{ij}}{Dt} \tag{14}$$

$$\dot{\varepsilon}'_{ij(pl)} = 0 \text{ for } \sigma_{II} < \sigma_{yield} \tag{15}$$

$$\dot{\varepsilon}'_{ij(pl)} = \chi\frac{\partial G_{pl}}{\partial \sigma'_{ij}} = \chi\frac{\sigma'_{ij}}{2\sigma_{II}} \text{ for } \sigma_{II} = \sigma_{yield} \tag{16}$$

Where η indicates viscosity and G represents the elastic shear modulus which relates deviatoric stress to deviatoric strain. The elastic component takes into account local variability of stress orientation due to rotation of Lagrangian markers through the objective co-rotational time derivative $D\sigma'_{ij}/Dt$ of the deviatoric stress tensor which also depends on G. The plastic deviatoric strain rate follows the plastic flow rule Gerya (2019) (eqs. 15-16). The second invariant of the deviatoric stress tensor is $\sigma'_{II} = \sqrt{\sigma'_{xx}{}^2 + \sigma'_{xy}{}^2}$ and the plastic flow potential $G_{pl} = \sigma'_{II}$ is an expression of how much volumetric energy mechanically supports plastic deformation. Finally, $\chi = 2\dot{\varepsilon_{II}}_{,pl}$ is called the plastic multiplier which is activated when the Drucker-Prager yield condition is reached:

$$\sigma'_{II} = \sigma_{yield} \tag{17}$$

Here, the plastic yield strength σ_{yield} is calculated according to 2D Drucker-Prager plasticity and depends on cohesion C, static friction μ, the pore fluid pressure ratio Pf/Ps and pressure P :

$$\sigma_{yield} = C + \mu \cdot \left(1 - \frac{P_f}{P_s}\right) \cdot P \tag{18}$$

In the case of a seismo-thermo-mechanical (STM) simulations, friction is strongly slip rate-dependent to simulate frictional instabilities (van Dinther et al., 2013) according to spontaneously evolving geometries (Dinther, 2013; Van Dinther et al., 2014). The slip rate is calculated as the visco-plastic strain rate times the fault width assuming a fault localizing to one cell, as typically occurs when simulating plasticity (Buiter et al., 2006). This is calculated from the previous local viscosity η_m and the local horizontal grid step Δx as $V = (\sigma_{yield}/\eta_m) \cdot \Delta X$. This horizontal grid step dependence limits the accuracy of seismic events to the high-resolution area where $dx = dy$. The friction coefficient is then calculated as

$$\mu = \mu_s \cdot (1 - \gamma) + \mu_s \cdot \frac{\gamma}{1 + \frac{V}{V_c}} \tag{19}$$

The static friction μ_s decreases with increasing strain in cases where strain weakening is implemented (Table 2). Within a predefined accumulated strain interval (i.e. 0.3-0.5 for the sediments in Table 2), the friction coefficient decreases linearly from its maximum to its minimum value. The friction coefficient at the time of calculation lies between the static friction μ_s and the minimum dynamic friction μ_d depending on the slip rate. Finally, the characteristic velocity V_c represents when the friction coefficient has undergone half of the maximum change of μ_s to μ_d.

For the visco-plastic deformation an effective viscosity has to be used, which incorporates weakening by plastic yielding. Yielding materials have a decreased viscosity. If the material is not undergoing plastic deformation, the effective viscosity is the same as the ductile viscosity and deformation is thus ductile. The viscosity representative of purely ductile deformation is calculated as the harmonic average of the contributions by thermally activated diffusion creep and stress-activated dislocation creep:

$$\frac{1}{\eta_{eff}} = \frac{1}{\eta_{diff}} + \frac{1}{\eta_{disl}} \tag{20}$$

where the respective components are given by (Gerya and Yuen, 2007)

$$\eta_{diff} = \frac{1}{2} A_d \tau_{tr}^{1-n} \exp\left(\frac{E_a + PV_a}{nRT}\right) \tag{21}$$

$$\eta_{disl} = \frac{1}{2} A_d {\sigma'_{II}}^{1-n} \exp\left(\frac{E_a + PV_a}{nRT}\right) \tag{22}$$

In these equations, A_d is the pre-exponential factor, τ_{tr} corresponds to the change from dislocation creep at elevated stresses to diffusion creep at higher temperature, and is set to 30 kPa following Turcotte and Schubert (2002). E_a, V_a and n represent the activation energy, activation volume and stress exponent, respectively. R indicates the universal gas constant.

The equations above are for the case of the reference model ER (Figure 5, Table 2). In model FP (Table 1), the influence of Peierls creep is briefly investigated. This plastic deformation mechanism occurs in olivine in the lithospheric mantle at high pressure / low temperature (HP/LT) conditions (Katayama and Karato, 2008; Evans and Goetze, 1979) and acts as a stress-limiter through

$$\eta_{Peierls} = \frac{1}{2A_{Peierls}{\sigma_{II}}^2} \exp\left\{-\frac{E_a + PV_a}{RT}\left[1 - \left(\frac{\sigma_{II}}{\sigma_{Peierls}}\right)^k\right]^q\right\}. \tag{23}$$

The experimentally determined values for the material parameter $A_{Peierls}$ and the maximum plastic strength $\sigma_{Peierls}$ are $10^{-4.4}\mathrm{Pa}^{-2}\mathrm{s}^{-1}$ and 9.1 GPa, respectively (Evans and Goetze, 1979). Additionally, p and q are shape- and geometry-dependent parameters that are assumed 1 and 2 (Dal Zilio et al., 2020). When included in the model, $1/\eta_{Peierls}$ is added to equation 20.

Table 1: Overview of parameter studies with respect to the reference model which has layering as in Table 2 and a setup described below. The reference parameter value in each model series is given in parentheses. For the results, the reader is referred to Section 4.3

Model ID	Parameter changed (reference value)	Value
ES	Slab age (70 Ma)	40 Ma
FV	Slab age	50 Ma
FW	Slab age	60 Ma
ET	Slab age	100 Ma
EU	T_{Moho} (450°C)	350°C
EV	T_{Moho}	400°C
EW	T_{Moho}	500°C
EX	T_{Moho}	550°C
EY	Low-viscosity zone on left boundary (absent)	present
EZ	Lower crustal thickness (15 km)	20 km
FA	Lower crustal thickness	25 km
FB	Lower crustal rheology (mafic granulite)	plagioclase
FC	Lower crustal rheology	wet quartzite
FD	Right lower crustal rheology	plagiolcase
FE	Right lower crustal rheology	wet quartzite
FF	$\mu_{eff,UC}$ (0.06)	0.12
FG	$\mu_{eff,UC}$	0.18
FH	$\mu_{eff,UC}$	0.24
FI	Ocean length (610 km)	510 km
FJ	Ocean length	410 km
FK	Ocean length	310 km
FL	Convergence setup (one-sided 10 cm/yr)	two-sided, both 5 cm/yr
FP	Peierls creep (disabled)	enabled
FQ	Lithospheric mantle P_f/P_s ratio (ref 0.0)	0.25
FR	Lithospheric mantle P_f/P_s ratio	0.50
FS	Lithospheric mantle P_f/P_s ratio	0.75
FT	Ocean length and LM P_f/P_s	510 km and 0.50, i.e. FI + FR

3.3 Model setup

The reference model domain has dimensions of 3000 km x 800 km (Figure 4). The pre-reference models at the end of section 4.3 have a vertical size of 700 km. In contrast to e.g. Dal Zilio et al. (2020), the transitions between different resolution areas are not abrupt. Instead, gradual transitions were calculated using a parabola fitting script written during this research. The resulting horizontal grid resolution varies smoothly from 10 km along the first 700 km to 500 m beginning at 800 km. The high-resolution area spans from 800 km to 1500 km, after which a gradual transition to 2 km occurs at 1530 km. Between 1850 km and 1900 km, there is another transition to 10 km which continues up to the right boundary of the box. The vertical resolution varies between 500 m for the first 100 km, reaching 1 km at a depth of 103 km. The resolution then changes from 1 to 5 km between 300 and 345 km, after which it remains constant. The temporal resolution of the models is 1 kyr in case of long-term modelling. This is gradually reduced to a constant 5 yr in the STM simulation of the reference model.

Continental convergence setup and kinematic boundary conditions

The reference model consists of two continents separated by a 610 km long oceanic plate. The continents are divided into 15 km of felsic upper crust, as well as 20 km of strong, mafic granulite lower crust (Table 2). The oceanic crust consists of 2 km of basaltic upper crust and 8 km of gabbroic lower crust (Figure 5). To initiate subduction and convergence a semi-dynamic approach is used in which an initial constant velocity is imposed (e.g. Duretz et al., 2011; van Dinther et al., 2013; Dal Zilio et al., 2020). In this method a constant convergence rate is imposed to initiate subduction and continental convergence. It is switched off after a predefined moment

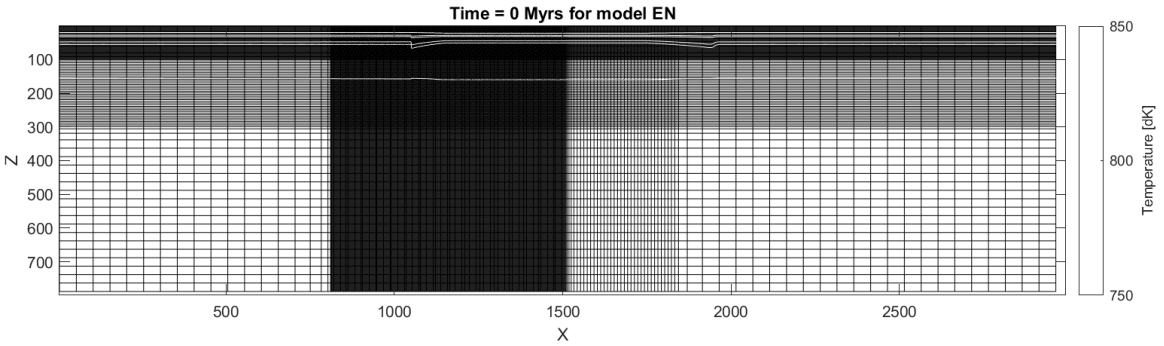

Figure 4: Grid resolution showing every fifth grid line in both directions. Note the gradual transitions between lower and higher resolution areas, which were calculated using a quadratic function fitting program written for this thesis. White lines are isotherms at 0, 150, 350, 450 and 1300°C (also in all figures below).

in time. After this period (referred to as the initial or kinematic stage), the geodynamic system has enough driving forces to evolve further on its own without externally applied kinematic boundary conditions.

In the case of this study a kinematic convergence period of 5 Myr is used. The right continent is pushed to the left at a rate of 10 cm/yr, such that at the end of the initial stage 500 km of convergence has been accommodated. The viscosity within the push area is increased to prevent artificial deformation. All mechanical boundaries are free slip (Figure 5). Since the model has elasticity, materials have stress memory. The push introduces stress anomalies in the overriding plate. To reduce propagation of these anomalies around the push area, stress relaxation is applied in an area around the push location (Figure 5). A small low-viscosity zone is present on the right side, allowing the overriding plate to decouple from the model boundary without inducing strong extension. This low-viscosity zone is not present on the left, such that the lower plate is fixed. This best represents the situation in the Central Alps, where the small Adriatic plate overrides the much larger Eurasian plate which has moved very little since the Late Cretaceous (Dewey et al., 1989). The effects of having one plate move towards the other (i.e. one-sided convergence) instead of two plates moving towards each other (i.e. two-sided convergence) are often assumed to be small (e.g. Duretz et al., 2011; Vogt et al., 2018). They are briefly investigated in Section 3.4. Finally, the 660 km discontinuity is implemented in a simplified way by an increase in density of mantle material to represent the phase changes to perovskite (Ito et al., 1990). This is enough to prevent slabs from crossing the boundary, even while there is no predefined change in viscosity across this boundary.

Table 2: Rheological parameters used for the reference model. All materials have a specific heat capacity C_p of 1000 $\mathrm{Jkg^{-1}K^{-1}}$, thermal expansion $\alpha = 3 \cdot 10^{-5}\mathrm{K^{-1}}$ and thermal compressibility $\beta = 10^{-5}\mathrm{MPa^{-1}}$.

Material	Sediments	Continental Upper Crust	Continental Lower Crust	Oceanic Upper Crust	Oceanic Lower Crust	Mantle
flow law	wet quartzite	wet quartzite	mafic granulite	wet qtz	Plg/An 75%	Dry olivine
ρ_0 [kg/m^3]	2600	2750	3000	3000	3300	3300
A_d [Pa^{-n}s]	$1.97{\cdot}10^{17}$	$1.97{\cdot}10^{17}$	$1.25{\cdot}10^{21}$	$1.97{\cdot}10^{17}$	$4.80{\cdot}10^{22}$	$3.98{\cdot}10^{16}$
E_a [kJ/mol]	154	154	445	154	238	532
V_a [J/bar]	1.2	0.8	0.8	0.8	0.8	0.8
n	2.3	2.3	4.2	2.3	3.2	3.5
$\frac{1}{A_d}$ Pa^{-n}s	$1.97 \cdot 10^{17}$	$1.97 \cdot 10^{17}$	$1.25 \cdot 10^{21}$	$1.97 \cdot 10^{17}$	$4.8 \cdot 10^{22}$	$3.98 \cdot 10^{16}$
H_r [μW/m^3]	1.5	0.25	1.5	0.25	0.022	0.022
k [W/(mK)]	$\left(0.64 + \frac{807}{T+77}\right) exp(4 \cdot 10^{-6} P)$	$\left(0.64 + \frac{807}{T+77}\right) \exp(4 \cdot 10^{-6} P)$	$\left(0.64 + \frac{807}{T+77}\right) \exp(4 \cdot 10^{-6} P)$	$\left(1.18 + \frac{974}{T+77}\right) \exp(4 \cdot 10^{-6} P)$	$\left(1.18 + \frac{974}{T+77}\right) \exp(4 \cdot 10^{-6} P)$	$\left(0.73 + \frac{1293}{T+77}\right) \exp(4 \cdot 10^{-6} P)$
G [GPa]	25	34	34	38	38	67
μ_s	0.35-0.20	0.15	0.20	0.03	0.06	0.6
λ	0.4	0.4	0.4	0	0	0.4

Temperature setup

The temperature distribution in the oceanic plate is governed by the cooling half-space model (Turcotte and Schubert, 2002)

$$T(z) = T_a + (T_0 - T_a) \cdot \left(1 - \mathrm{erf}\left[\frac{z}{2\sqrt{\kappa\tau}}\right]\right), \tag{24}$$

where T_a is the temperature at the lithosphere-asthenosphere boundary (LAB), T_0 is the temperature at the surface, z is the depth below the surface, $\kappa = 1.0 \cdot 10^{-6}\mathrm{m^2/s}$ corresponds to thermal diffusivity ($\kappa = k/(\rho C_p)$)and $\tau = 70$ Ma is the age in seconds of the oceanic lithosphere (Turcotte and Schubert, 2002). The initial geotherm of

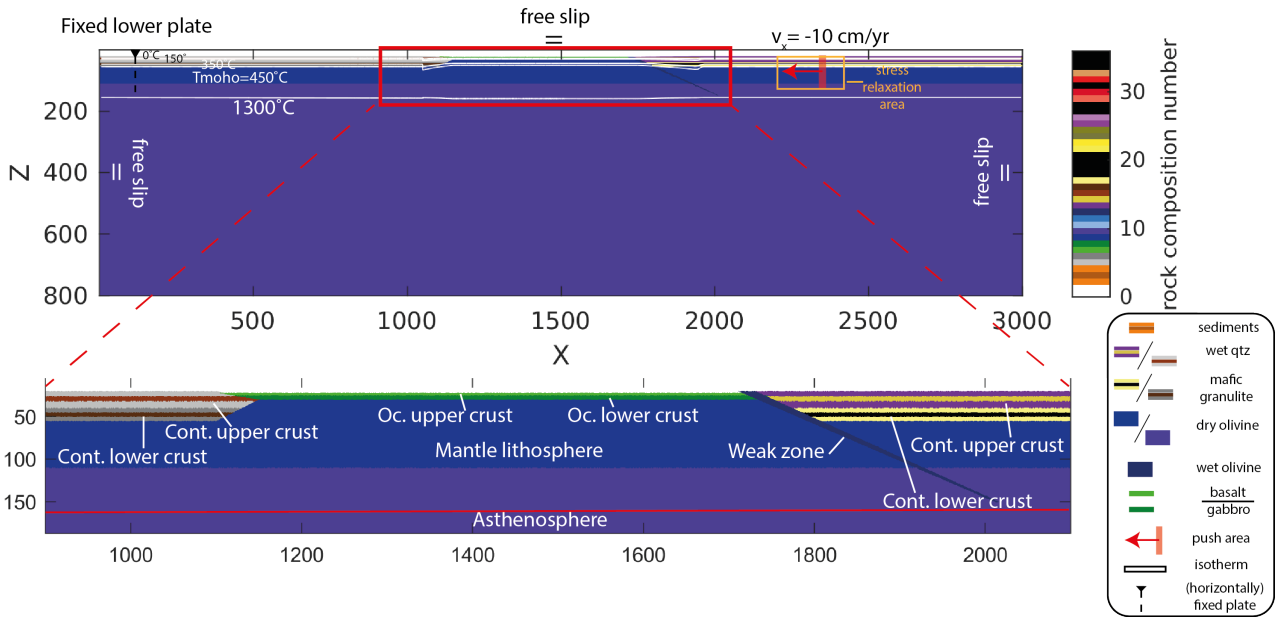

Figure 5: Reference model setup displaying boundary conditions (high-viscosity push area, free slip and fixed lower plate), lithological stratification and isotherms (white lines). The push of 10 cm/yr from the right is applied only during the first 5 Myr, after which the model can sustain itself dynamically. Stress changes are relaxed in an area around the push location. Rheological parameters are displayed in Table 2.

the continental lithosphere is constrained by the Moho and the LAB temperatures. Therefore it initially consists of two linear segments. The first evolves linearly from the surface (0°C) to the Moho (450°C at 35 km below the surface). The second segment starts from the crust-mantle boundary and ends at the lithosphere-asthenosphere boundary (LAB) at 1617.6 K or 1347.45°C. The LAB is located at z = 160 km (140 km subsurface). Henceforth, all mentioned depths are minus the free surface. The asthenosphere itself follows a thermal gradient of 0.5 °C/km to an external boundary far below the lower margin of the model (Gerya, 2019).

3.4 Initial conditions

3.4.1 Weak zone

Within the reference parameter space, it is important to know how the initial conditions define the model behaviour. The weak zone for example is wedge-shaped and defines the boundary between the right continent and the ocean (Figure 5). At the surface it is 20 km wide and its central axis plunges through the lithosphere at an angle of 20 degrees. The weak zone is used in this case to initiate subduction and is justified because we are not interested in solving the challenge of subduction initiation (e.g. Stern and Gerya, 2018; Auzemery et al., 2020; Beaussier et al., 2019). Varying it by 5 degrees up and down yields important information for this kind of semi-dynamic geodynamic models. A gentle dipping weak zone results in flat slab subduction where the subduction interface is relatively long and subduction is thus resisted over a larger domain. Only a small portion of slab hangs freely in the asthenosphere. The slab pull is not sufficient to sustain further convergence of the model and subduction stalls (Figure 6). Therefore, one could choose to push for longer. However, this means that the dynamics of the model would be more determined by kinematic pushing than by internal forces. A 25 degree weak zone, i.e. slightly steeper than reference, promotes a faster accumulation of slab during early stages. A steeper subduction angle also increases the frictional resistance of the overriding continental crusts to subduction once it has been initiated. When the kinematic push is switched off, subduction was found to accelerate more than in the reference model, increasing the chance of sediments to be subducted. The presence of a thick layer of sediments in the subduction channel lead to plate decoupling in many models, which is why these weak zone angle experiments were initially set up. The experiments demonstrate that the modelling outcome is rather sensitive to changes in such initial conditions, due to the way subduction initiation is triggered.

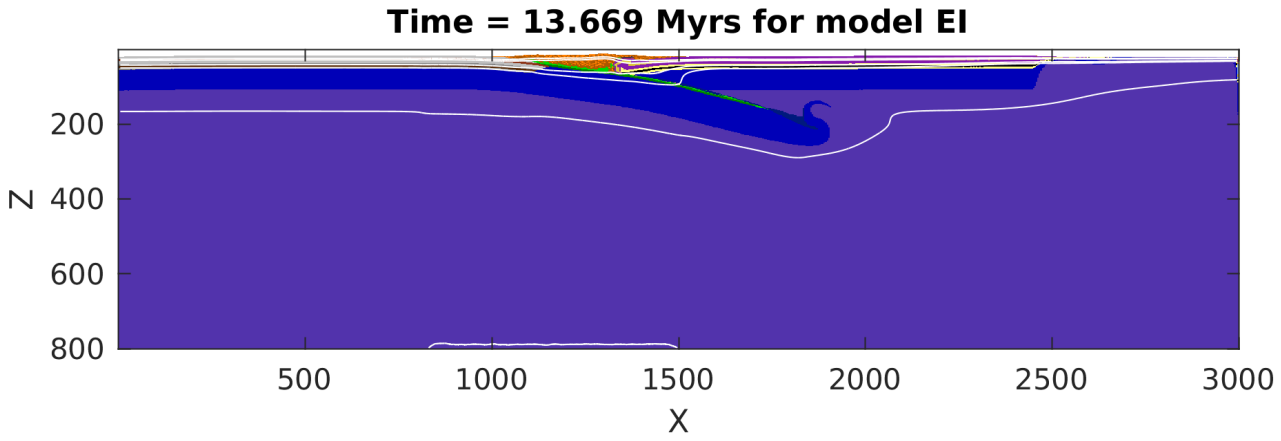

Figure 6: Model EI with a weak zone dipping 15° at an advanced timestep. The slab does not steepen due to the strong coupling along the relatively long plate interface. A negligible amount of convergence has been accommodated since the push stopped at 5 Myr.

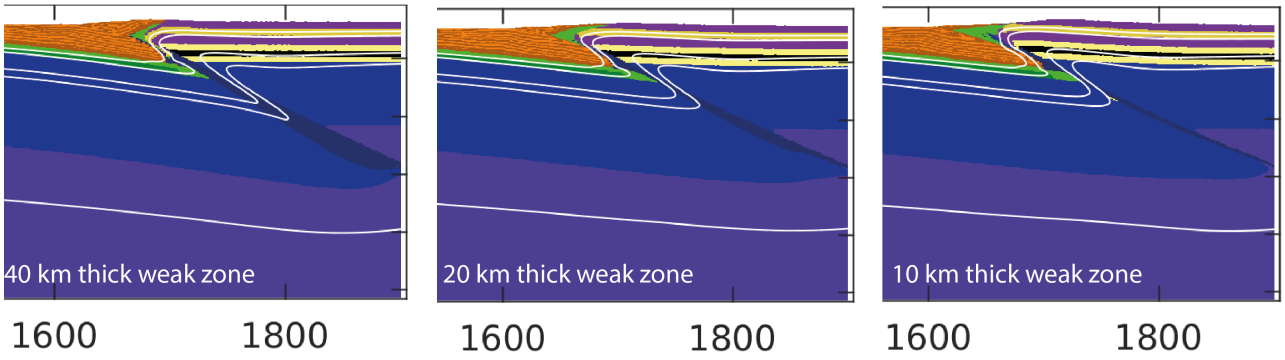

Figure 7: Different weak zone thicknesses were tested for pre-reference models EH (40 km), EL (20 km) and EM (10 km). A too thick weak zone promotes upward tilted upper plate tips, while a too thin weak zone makes subduction initiation harder, resulting in double subduction in cases with low Moho temperatures (< 400°C, Figure 26)

3.4.2 Convergence rate

The kinematic boundary conditions were also investigated before the current reference model was established. Different convergence rates were tested in an early stage of this research. Models BA (2.5 cm/yr for 20 Myr), AM (5.0 cm/yr for 10 Myr) and BC (10 cm/yr for 5 Myr). The rheological parameters used in these models are slightly different from those in Table 2. However, the convergence setup is the same, i.e. one-sided convergence with a fixed lower plate. A slow initial convergence rate was found to hinder slab detachment due to regular dripping from the slab tip. The resulting smaller slab decreases the magnitude of driving forces slab pull and/or mantle drag promoting trench advance instead of retreat. The 5 cm/yr and 10 cm/yr models display rather similar evolutions (Figure 8).

Differences between 5 and 10 cm/yr convergence rates are relatively limited. A faster convergence gives less time to the slab to bend, resulting in steeper slabs during the initial stage (Figure 8a,d). However, this difference is largely removed during the trench retreat stage (Figure 8b, e). The final model results are similar enough to justify the use of 10 cm/yr convergence rates for the other models (Figure 8c, f). The fast convergence rate leads to a 10% wider orogen more deformation towards the foreland. Fewer backthrusts form, giving less space to oceanic crust to rise from below.

3.4.3 One-sided vs two-sided convergence

In models with the semi-dynamic approach, i.e. a period of forced convergence until some fixed amount of convergence is achieved and fully dynamic afterwards, it is often assumed that one-sided convergence produces

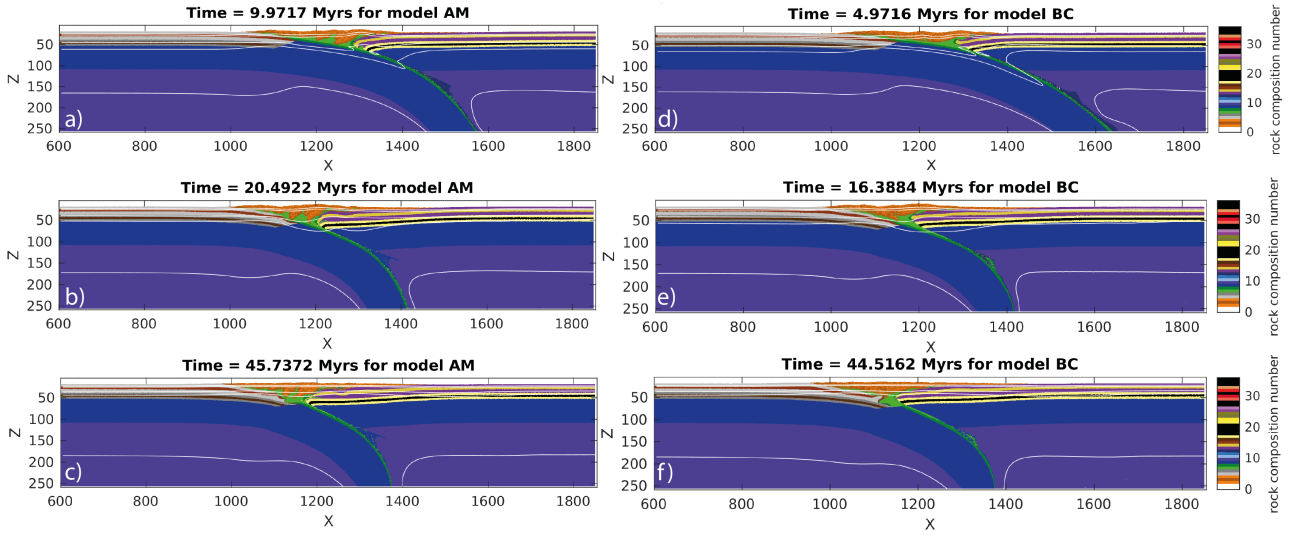

Figure 8: Key stages in the model evolution of pre-reference models AM (5cm/yr) and BC (10 cm/yr) to illustrate the effect of intermediate and fast initial convergence rates. From top to bottom, these stages are end of kinematic stage, moment of slab detachment and the end of the simulation.

similar results as two-sided convergence. In two test runs with one-sided convergence without a fixed lower plate, the left continent accelerated to extreme velocities as soon as the push stopped, leading to complete crustal subduction (the high strain rates make deformation elastic). Due to the speed by which this occurred (75 cm/yr), the slab overturned after reaching the 660 km discontinuity and detached at the ocean-continent transition. To test the effect of including the fixed lower plate, model BT was set up. It has an identical setup to model BS, but for a one- instead of two-sided convergence in combination with a fixed lower plate, impairing horizontal movement of the down-going plate.

The kinematic stages are extremely similar (Figure 9), indicating that the convergence direction by itself has a limited influence on the modelling outcome. Instead, the fixed lower plate condition is more important. The fixed lower plate condition makes sure that the left continent does not accelerate after the push is released. This has a large influence on the further evolution of the model. While the left continental crust subducts in model BS, it does not in model BT (Figure 9). Furthermore, the large slab of model BS lies down at the 660 km discontinuity and detaches close to the continent-ocean transition at a depth of 260 km after fast (0.15 Myr) necking. On the other hand, the slab in model BT is much smaller and contains no continental crust. The slab dip remains stable at 60 degrees, which is gentler than the 75 degrees of model BS. A portion of the slab detaches at a depth of approximately 380 km after 0.15 Myr of necking, at a time of 16.13 Myr. This is 5.8 Myr later than in model BS. However, after rollback little happens except for barely noticeable rollback (20 km in 28 Myr). The end result is a well-developed double-vergent, wide orogen (Figure 9). Notably, the plates are strongly coupled throughout the simulation and no crustal flow is observed, in contrast with model BS (Figure 9). Since the Central Alps are a double-vergent orogen, one-sided collision with a fixed lower plate is thus preferred over two-sided collision.

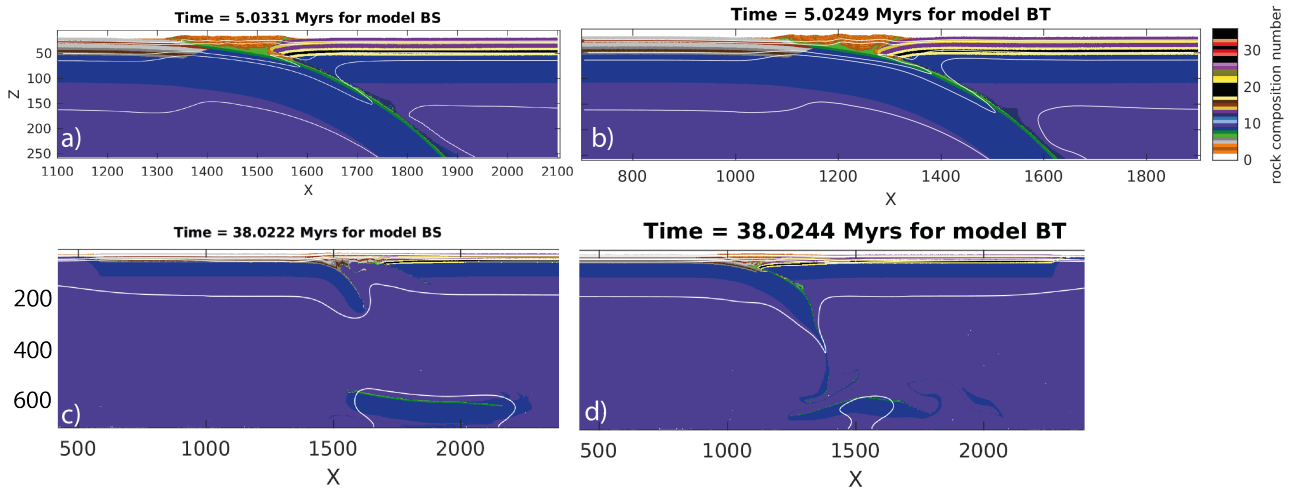

Figure 9: Comparison of two-sided convergence (**a, c**) with single-sided convergence (**b, d**) models. Two-sided convergence leads to extensive continental subduction, delamination and plate decoupling, as well as shallower detachment. Single-sided convergence with a fixed lower plate results in a double-vergent orogen. The slab detaches later and deeper, and little continental material subducts.

4 Results and analysis

4.1 Reference model

4.1.1 Kinematic evolution

During the initial stage of the model the overriding plate is pushed, such that the oceanic plate is consumed by the subduction zone. The entire oceanic lower crust and part of its upper crust are subducted, but the sediments are scraped off to build an accretionary wedge. The upper plate's upper and lower crust act as a backstop in this process of accretion and a wide retro-foreland basin develops (Figure 10a-b). At depth, the slab steepens rapidly from 33 to 58 degrees between 4.5 and 5.0 Myr (Movie S1). The intra-wedge deformation starts with in-sequence frontal accretion of thrust sheet-like structures. Growth of the wedge increases normal stresses at the basal décollement, which triggers basal accretion, i.e. development of back-thrusts that allow the development of several pop-down structures (Figure 10b).

Immediately after the constant velocity push is released at 5 My, the upper plate accelerates due to a strong horizontal mantle traction which in turn was induced by rapid slab steepening between $t = 4.5$ and $t = 5.0$ Myr (section 4.1.2). The wedge is emplaced on top of the left continent, pressing the down-going plate down. This effectively causes subduction of the upper and lower continental crust (Figure 10c-d). The result is significantly accelerated subduction (160 km in 0.6 Myr, i.e. 26.7 cm/yr) until the drag force recedes, slowing down trench retreat. The stiff, straight slab starts to lie down on the 660 km discontinuity at 6.0 Myr where-after slab steepening from 45 to 65 degrees occurred between 6.0 and 8.0 Myr. Slab steepening results in slightly accelerated trench retreat. Simultaneously, downward corner flow of asthenosphere along the right side of the slab pulls the weak and hot slab tip to the right. Together these two processes induce extension in the flat-lying slab portion, causing two small slab segments to be "convectively separated" from the main slab. This has no effect on the slab pull magnitude (section 4.1.2) and is hence not qualified as "slab detachment". In the wedge, shortening is accommodated between 5 and 6 Myr in its central area by thickening. Subsequently , downward suction in the subduction channel pulls the overriding lithospheric mantle into the orogenic core (Figure 11), rotating the overriding plate-wedge contact from a left-dipping to a right-dipping position. This contact now forms a pronounced retro-shear (Figure 10c-d). Between 6 and 10 Myr shortening is accommodated predominantly by pure-shear thickening of the upper crust of the overriding plate evidenced by a distributed deformation pattern in addition to low stress and viscosity (Figure 12). The upper crust is being pushed by relatively strong sediments in the wedge top. The strong lower crust is unaffected by this process. Eroded orogenic material ends up in the retro-foreland area, resulting in asymmetric deepening of the retro-foreland basin as well as a curved up tip of the overriding plate upper crust (Figure 10c-d). When the positively buoyant continental material from the lower plate reaches 140 km depth, it is pressed between both mantle lithospheres.

Although the coupling between the downgoing and upper plate decreases due to the high viscosity contrast between the downgoing continental crust and the lithospheric mantles (e.g. upper panel of Figure 12), strong tectonic underpressures form in the lithospheric mantles (Gerya, 2015) that make the subduction interface more coupled 11). As the slab pulls the lower plate further down the overriding plate is pulled down slightly over a length of 200 km, enhanced by downward suction across the subduction interface (Figure 11). The downward motion of the overriding plate promotes asymmetric deepening and narrowing of the retro-foreland basin.

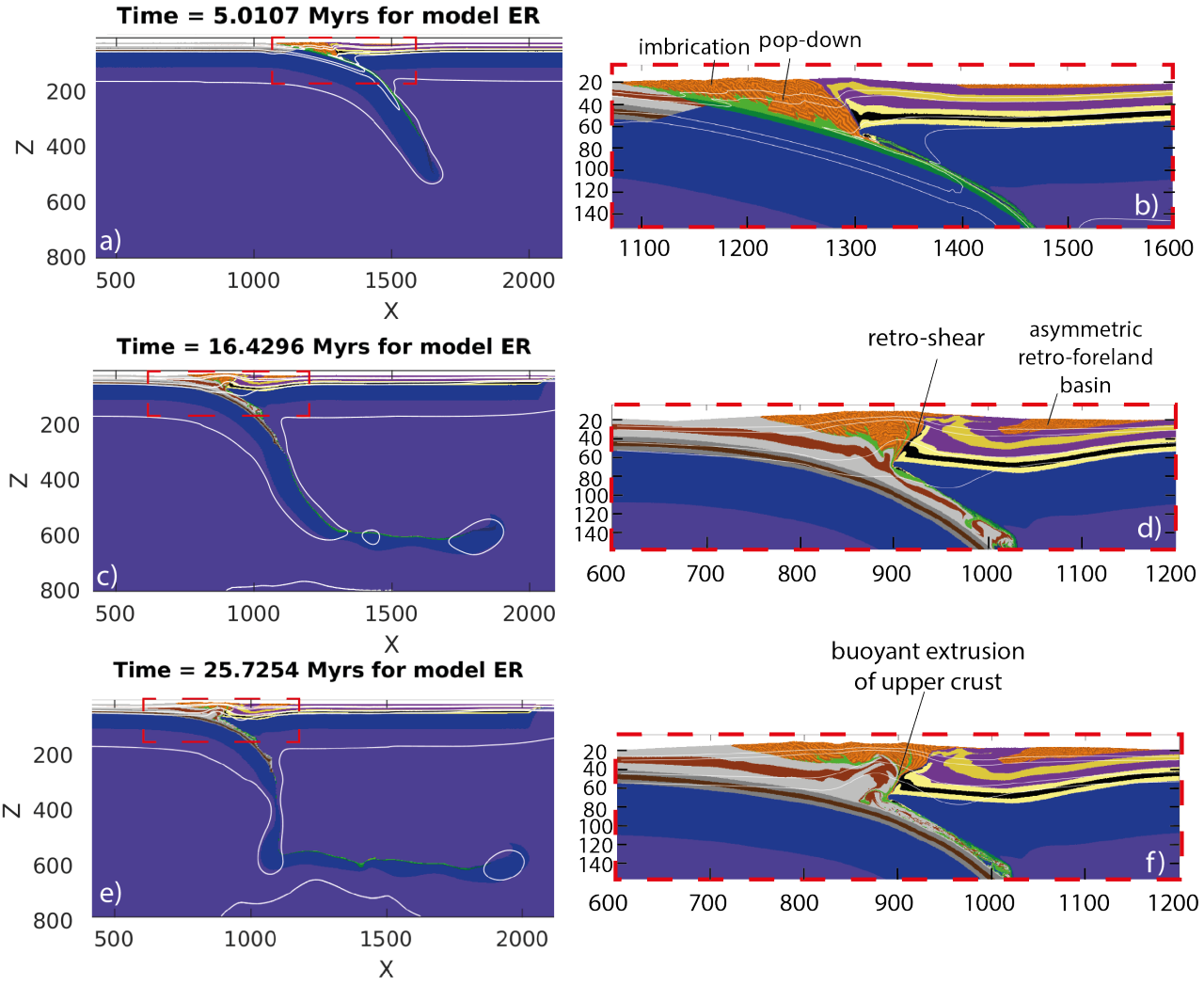

Figure 10: Snapshots of the reference model at three key moments in time: **a-b)** end of kinematic convergence stage where the accretionary wedge builds up, consisting of an imbricate sequence in the fore-wedge and pop-down structures in the back of the wedge **c-d)** a stage with active continental subduction and formation of a retro-shear. The down-going upper crust starts to decouple from its corresponding lower crust **e-f)** Viscous necking and slab detachment, followed by rebound without rollback.

Between 17 and 21 Myr, trench retreat slows down and stops. Instead, the lower plate upper crust decouples from the subducting lower crust (Figure 10e-f) through the process of buoyancy-driven delamination (Bird, 1979). After t = 21 Myr no further rollback is observed. The upper crust slowly flows back into the core of the orogen, proceeding to move upward along the retro-shear. Around the same time, the slab detaches at around 25.7 Myr at a depth of 330 km following a 2 Myr period of viscous necking. The remaining slab rebounds 40 km upward while slowly unbending during a period of 14 Myr (Figure 13) generating compression below the orogen (Figure 14). No slab or trench rollback along with upper plate advance is observed during this time. Instead the orogen moves to the right by 40 km leading to upper plate movement away from the trench, and extension of the orogen (Figures 13 and 14). This is also readily observed in the topography signature of the reference model (Figure 15). The peak topography decreases from 9 to 6 km while the orogen width increases from 600 to 650 km. Furthermore, the retro-shear is visible as a valley within the orogen (Figure 15).

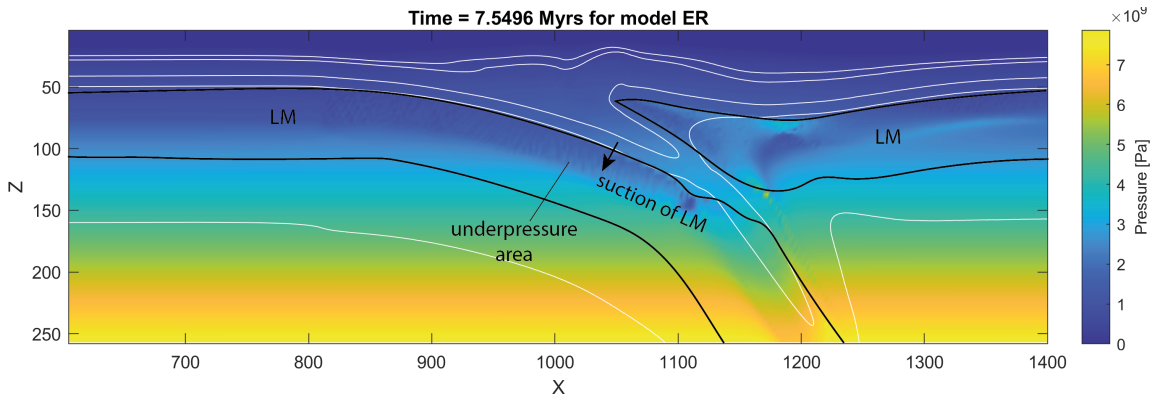

Figure 11: Dynamic pressure plot of the reference model showing downward suction induced by tectonic underpressures in the top of the down-going lithospheric mantle. Both lithospheric mantle contours are drawn for reference.

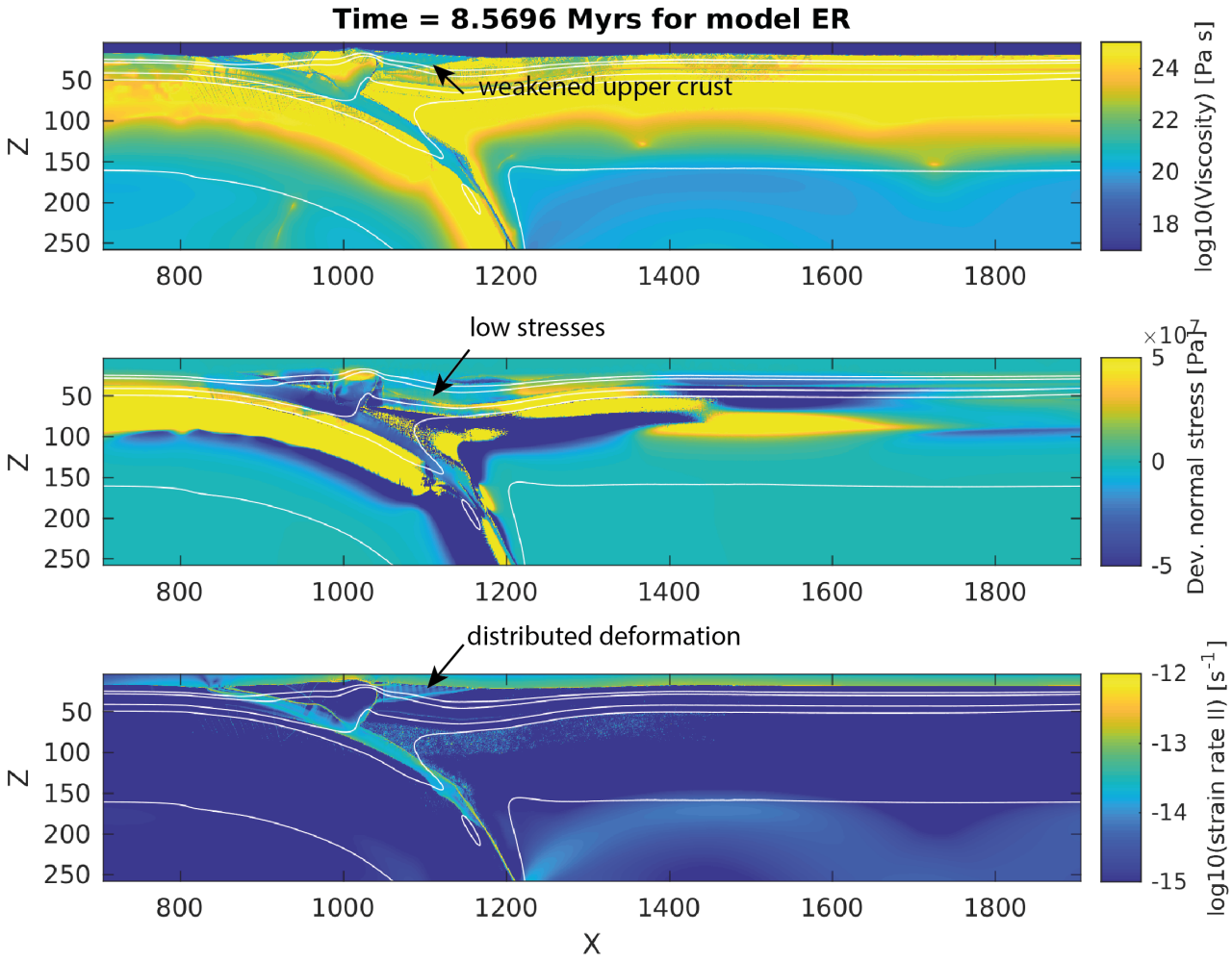

Figure 12: Zoomed-in snapshot of effective viscosity, normal stresses and total strain rate for the reference model during thickening of the overriding plate upper crust. The low viscosity and stresses in combination with a relatively distributed strain rate pattern suggest that the thickening occurs through pure-shear.

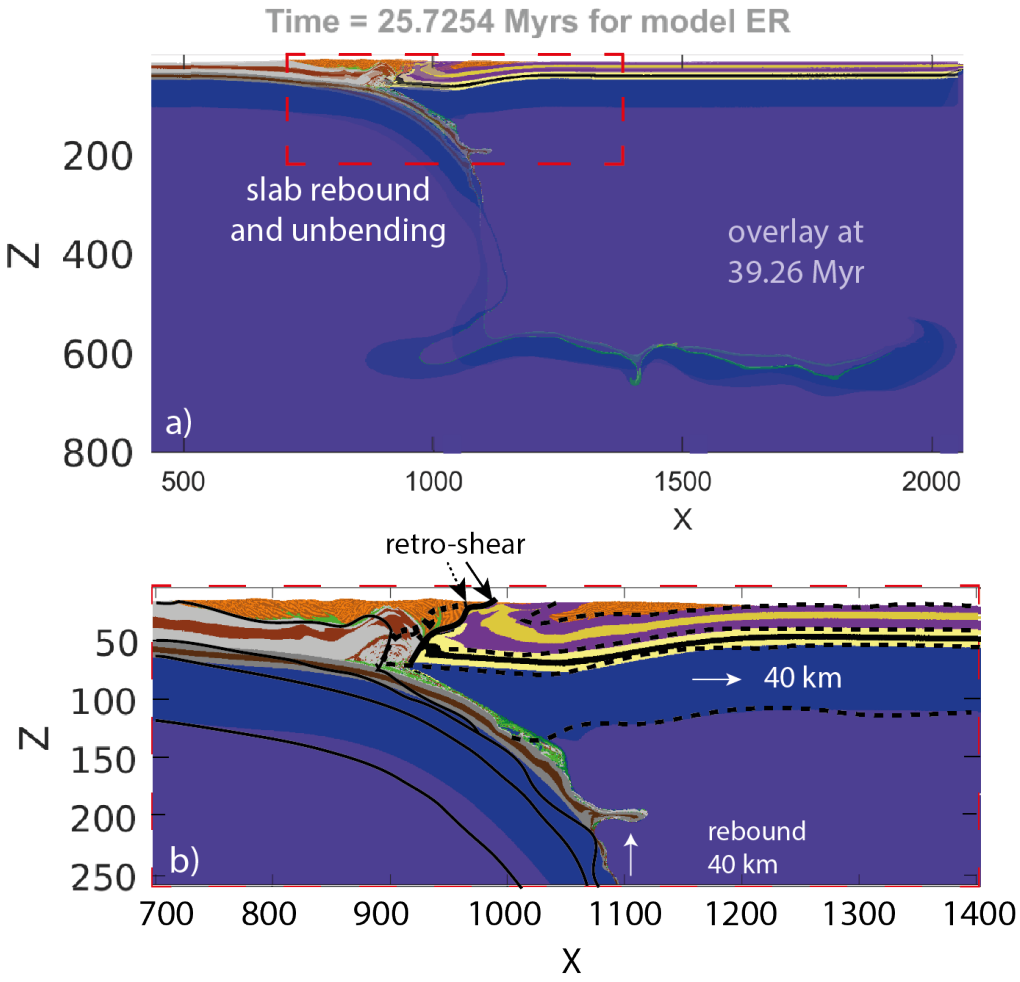

Figure 13: Visualisation of the rebounding remaining slab after detachment. **a)** The slab rebounds and unbends slowly between 25.7 Myr (transparent) and 39.3 Myr (more opaque overlay). The foreland changes very little, as it is not blurred by the overlay. **b)** Compositional layer contours at 25.72 Myr are drawn in continuous (down-going plate) and dashed (overriding plate) lines. The filled composition contours are taken at t = 39.26 Myr. All of the vertical shortening is accommodated by orogenic extension, causing backward movement of the overriding plate. The pre- and post-detachment locations of the retro-shear are also indicated for reference.

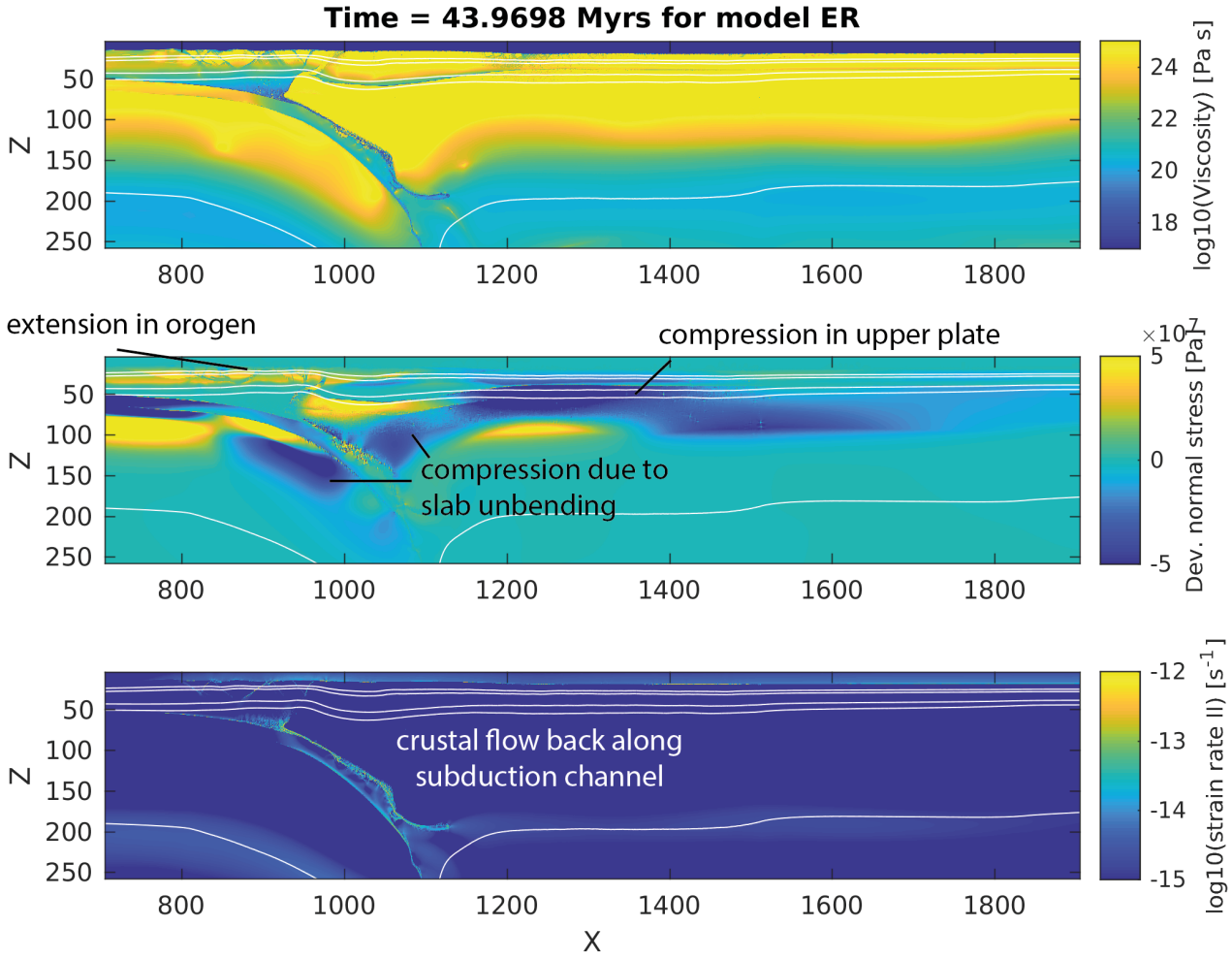

Figure 14: Viscosity (top), deviatoric normal stress (middle) and total strain rate at the end of the reference model simulation. The right continent is largely under compression (blue colours), while the orogen top and part of the indenting lower crust are under extension.

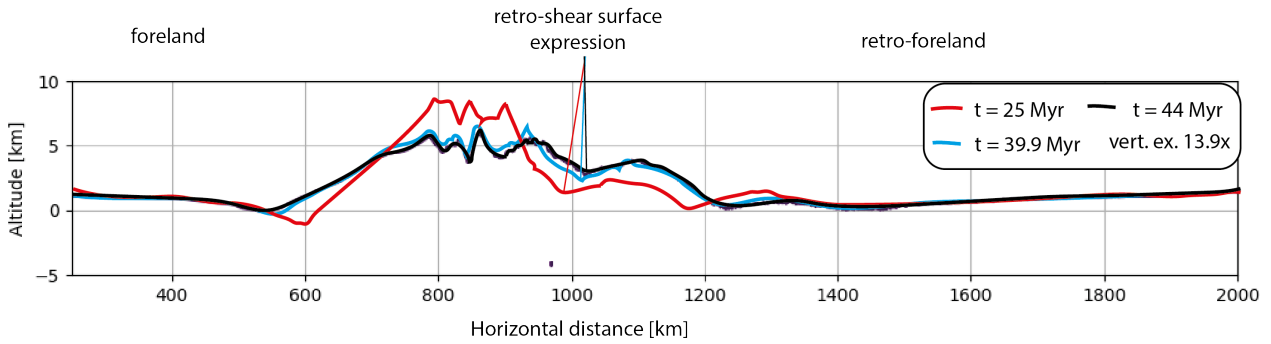

Figure 15: Topographic signature of the reference model at the moment of slab detachment (in red), at the end of the rebound (in blue) and at the end of the simulation (in black). The orogen widens and flattens after slab detachment as a result of extension.

4.1.2 Dynamic analysis

To understand why this kinematic evolution occurs, a dynamic analysis of the forces at play is set up here. Subduction and continental collision are driven by different forces. The purpose of this dynamic analysis is to infer if horizontal or vertical forces are more important (Section 1). Here, the two most important forces are quantified and compared. The most important horizontal force is assumed to be basal drag from the upper mantle which acts on the upper plate (Duretz and Gerya, 2013; Alvarez, 2010). This force is calculated as the integral of the shear stress along the part of the upper plate that overlies asthenosphere (Dal Zilio et al., 2020)

$$\int_{x_{trench}}^{L} \sigma_{xy} dx \tag{25}$$

However, the governing equations in this research are expressed in terms of *deviatoric* components (Section 3). Here, the shear stress is estimated as the product of the vertical gradient of horizontal velocity and the effective viscosity (Dal Zilio et al., 2020), i.e. equation 25 becomes

$$\int_{x_{trench}}^{L} \frac{\partial v_x}{\partial y} \cdot \eta_{eff} dx. \tag{26}$$

The most important vertical force in the model is slab pull, i.e. the buoyancy force exerted by the density difference between the down-going plate and the surrounding mantle. Depending on the degree of coupling across the plate interface it can affect the orogen and overriding plate as well. It is quantified here in the following way:

$$g_y \iint_A (\bar{\rho}_{slab} - \bar{\rho}_{surr}) dx dy \tag{27}$$

where $\bar{\rho}_{slab}$ and $\bar{\rho}_{surr}$ are the horizontally averaged slab and surrounding material densities. In practise, the slab is identified using the rock composition identifier taken from the nearest Lagrangian marker at every Eulerian node. In addition, a node is part of the slab if its temperature is below the LAB temperature of 1617.6 K (Section 3). To detect slab detachment, the number of elements with slab temperatures is counted at each depth interval. If fewer than 100 nodes (50-70 km total width) satisfy this condition, the area below that point is no longer taken into account in the calculation. The slab pull evolution figures in the next sections often display a sharp change in slab pull following detachment. This is a direct result of the above thickness threshold being no longer met, not of the speed of necking or shearing. Flat-lying (detached) portions of slab at the 660 km discontinuity are not taken into account as slab portions below 600 km depth are ignored. This approximation is justified as the deepest part of slab has the smallest temperature and therefore density anomaly. A slab identification plot of the reference model at $t \approx 30$ Myr is shown in Figure 16.

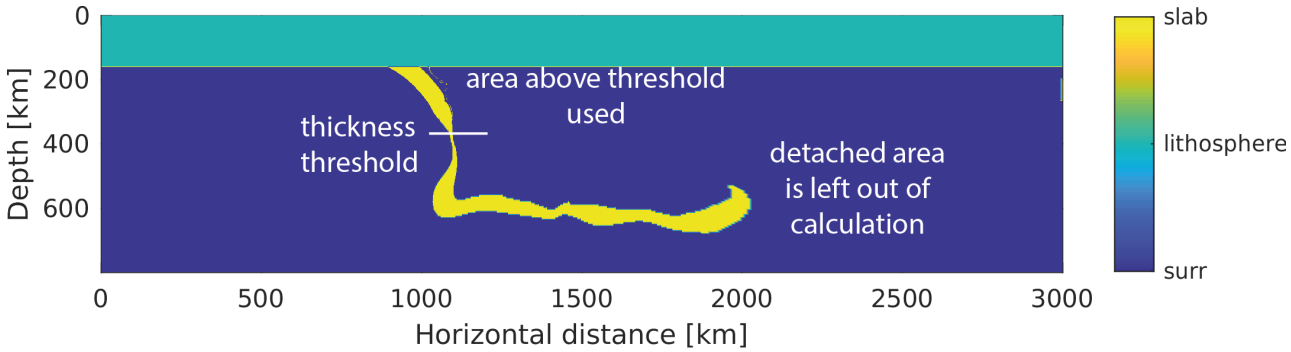

Figure 16: Slab identification result of the slab pull calculation program for the reference model. The algorithm excludes everything below the necking level (which no longer has lithospheric temperatures) where the slab detaches, and everything above the LAB at a depth of 140 km. The resulting force estimate provides reasonable size estimate (e.g. Sandiford et al., 2005), despite these approximations.

The slab pull force follows a distinct evolution (Figure 17). During the subduction stage, the negative buoyancy force increases as the slab area grows with subduction. As the kinematic boundary conditions are

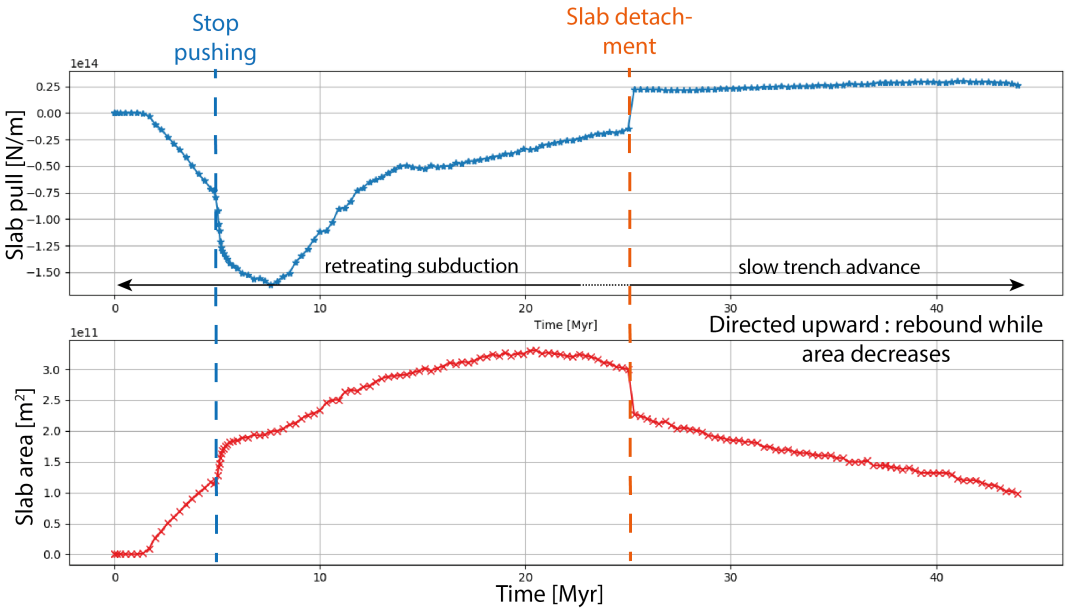

Figure 17: Evolution of the slab pull force and the slab area with time for the reference model ER. Moments of sharp in- and decrease are linked to the cessation of forced convergence and slab detachment.

stopped at t = 5.0 Myr, a sudden increases in the slab area and pull indicates a period of accelerated subduction. The rate of increase then diminishes while the overriding plate pushes the accretionary wedge on top of the lower plate. The peak slab pull force of about $-1.6 \cdot 10^{14}$ N/m is reached at $t = 7.8$ Myr, followed by an extended period of trench retreat until 16.5 Myr during which two small segments of slab are convectively removed from the slab. The retreat stops at around 21 Myr. During the retreat period the slab slowly heats up, rendering it unable to sustain subduction. The slab pull force has diminished to $-1.6 \cdot 10^{13}$ N/m by 25 Myr (Figure 17). At this point, a large portion of the slab detaches. The removal of a large negatively buoyant component makes the net slab pull positive, causing a polarity switch of the slab pull force. Immediately, the slab starts to rebound upward, expressed by a steady decrease in slab area (Figure 17). This rebound lifts relatively more subducting lower crust above the LAB than lithospheric mantle. Therefore, the positive buoyancy decreases. However, the slab pull force changes little during the rebound period. This is attributed to the simultaneous heating of the slab.

The most important horizontal force is the mantle drag exerted by the viscous asthenosphere on the base of the overriding plate. This flow is driven by slab motions (, e.g. subduction, slab steepening, slab rebound and trench retreat) that displace mantle material. When asthenospheric material flows underneath lithosphere, it exerts a traction on the overlying lithosphere, determined by the viscosity contrast between the two. The drag force is quantified for the reference model in Figure 18, where the slab pull magnitude is overlain for comparison. Because both the vertical gradient of horizontal velocity and the effective viscosity are highly variable around the LAB, the force is calculated at 4 close depths to give an impression of the uncertainty range. The narrow spread of these four lines suggests that the drag does not decrease immediately within the lithosphere. A positive drag force indicates a push to the right.

The peak mantle drag of $4 \cdot 10^{15}$ N is reached at the moment the push is switched off at 5 Myr (Figure 18), causing the overriding plate to accelerate and overcome the frictional resistance between the upper crust of the left continent and the base of the accretionary wedge. The lower plate is thus overthrust by the accretionary wedge. The subsequent subduction slowdown decreases flow velocities, causing the mantle drag to gradually diminish until 18.5 Myr. After this moment the drag decreases much more rapidly and switches polarity. This is linked to an acceleration of upper crustal flow from the subduction channel into the orogenic core, changing flow velocity gradients in the nose of the mantle wedge and pushing against the overriding plate. In response the overriding plate slows down and stops. It starts to move slowly in the opposite direction 3 Myr after the polarity switch at LAB depth (Figure 18 and Movie S2). The upper crustal exhumation occurs faster than the mantle flows (1-2 cm/yr vs 0.05-0.10 cm/yr), implying a lesser role of mantle drag in the upper plate movement reversal. In addition, the viscous necking at depth starts at $t = 23$ Myr as well, marking the onset of slow slab rebound

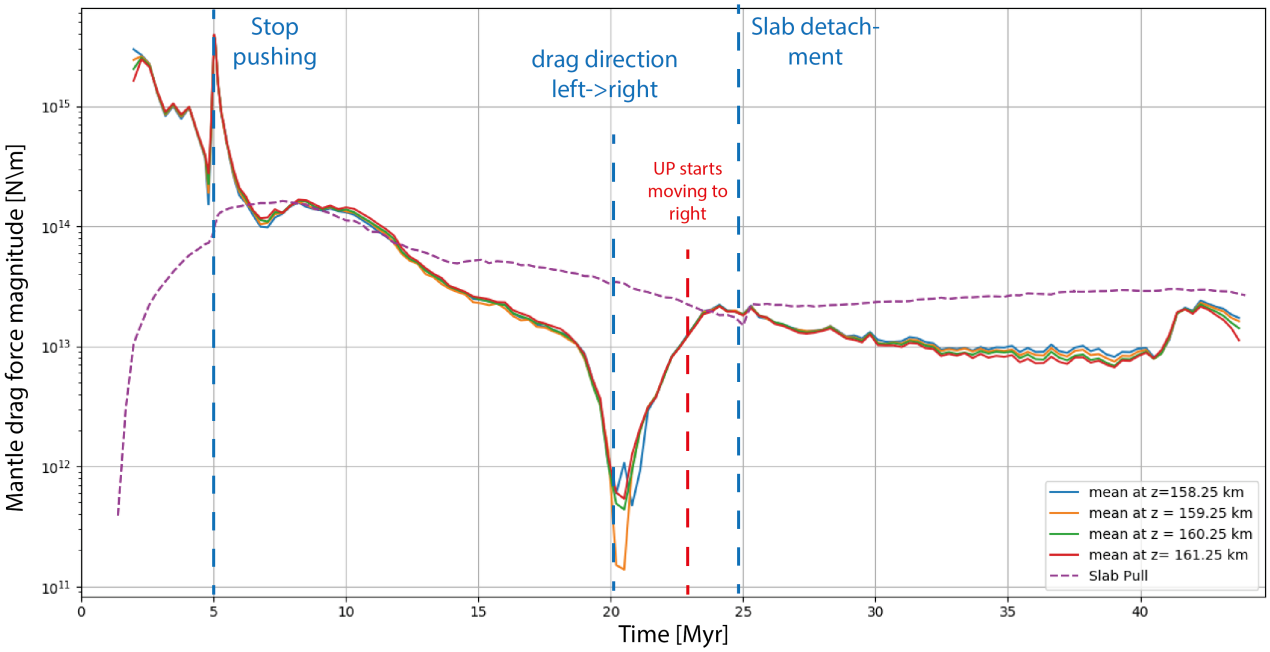

Figure 18: Temporal evolution of the horizontal drag force below the overriding plate. Due to the logarithmic nature of the drag, negative values would not be visible. Therefore the absolute values are shown here. In addition, the absolute slab pull force is dashed in purple.

and unbending which starts 2 Myr before the slab actually detaches. The rebound increases the rightward drag and backward movement of the overriding plate.

4.2 Short-term deformation

At the end of the long-term run of the reference model ER the orogenic system is assumed to represent the current state of the Central Alps. The simulation of seismicity adds an extra means of comparison between model and nature to evaluate how well the model dynamics and rheological behaviour resembles nature. The time step is reduced to 5 years to study the spontaneous spatio-temporal occurrence of friction instabilities representative of earthquakes (e.g., van Dinther et al., 2013; Dal Zilio et al., 2020). Using the event detection algorithm of Dal Zilio et al. (2018)), Lagrangian markers within the high resolution area are evaluated according to thresholds of stress drop (0.4 MPa) and velocity ($9 \cdot 10^{-9}$ m/s). They are grouped when close together in both space and time, i.e. within one grid cell and one time step of each other. Moment magnitudes are estimated using the empirical scaling law $M_w = a + b\log(W)$ of Wells and Coppersmith (1994) where the a and b values differ slightly with normal or reverse faulting and W is the rupture width in km. Here, $a = 3.80$ and $b = 2.44$ were used, corresponding to the average value of 203 events regardless of the structural style (Blaser et al., 2010). For reliable seismic events the rupture width needs to cover at least two grid cells, i.e. $W > 1$ km. This limits the magnitude of events that are theoretically well resolved to about 4. Hence, only events with magnitudes ¿ 4 are shown in Figures 19 and 21.

The simulated events can be characterized by a few key features. First, most events occur in the subduction channel, i.e., from 80 to 100 km depth (Figure 19). The composition figure shows that these events take place in a mixture of oceanic crust and continental lower crust and to a lesser extent in the upper crust. While the thresholds are passed, most of these events are likely not actual earthquakes. A detailed analysis of the displacements in the reference model (Movie S2) shows that they occur where the lower crust is delaminating from the down-going plate while the weak, ductile upper crust moves along the retro-shear (middle panel in Figure 14). Additionally, a plot of the spatio-temporal evolution of the recorded events shows some events that keep slipping on the same location for thousands of years continuously (e.g. X $\approx$ 950 km and Z = 80 km in Figure 20). In theory these could be frequently repeating small earthquakes, but considering their location in the fast domain at the edge of the largely ductile deformation regimes it is more likely to represent ductile deformation at very high visco-plastic strain rates that exceed the selected threshold (Figure 21). The origin

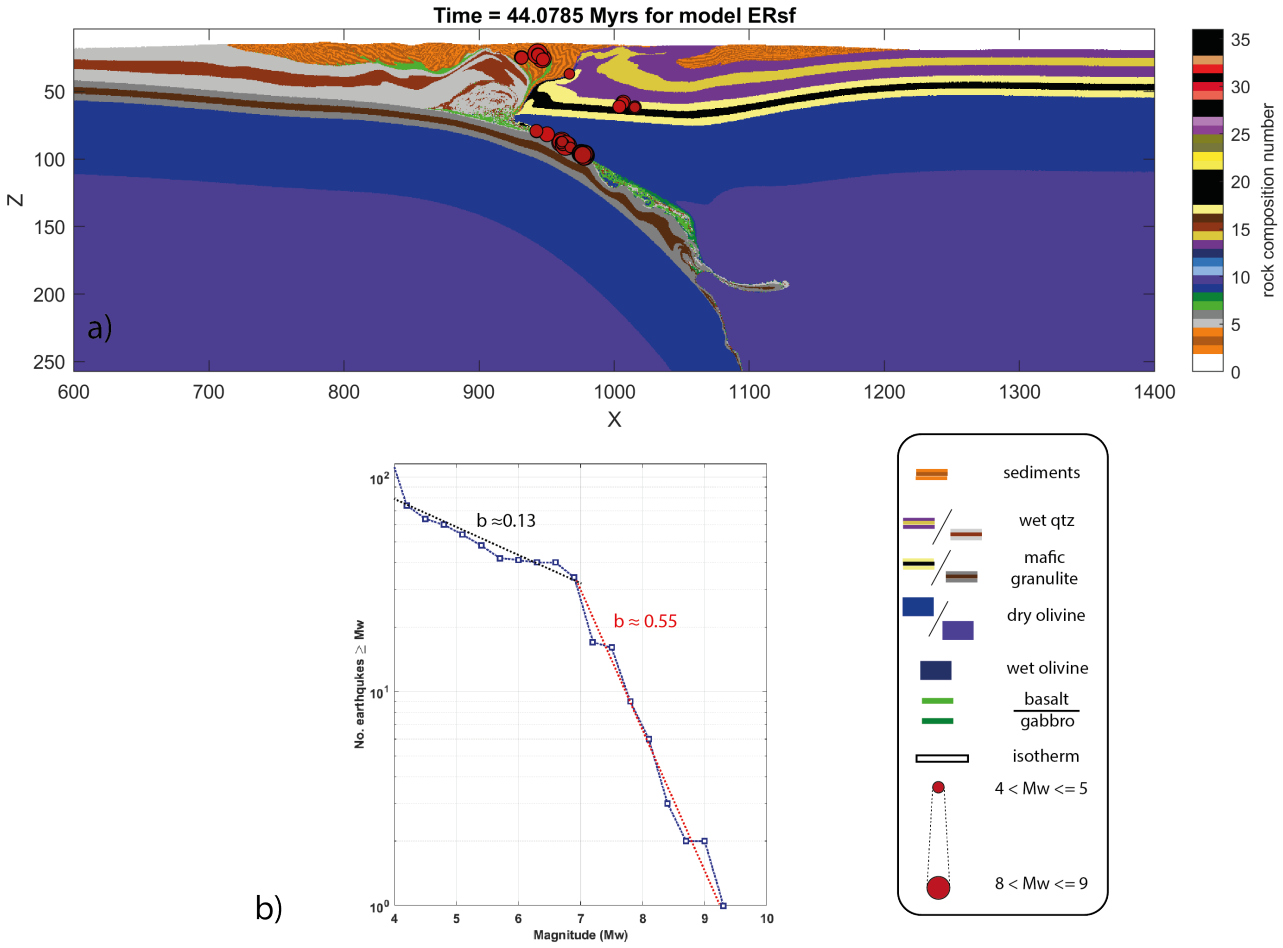

Figure 19: **a)** Hypocenters of simulated events with a magnitude 4 and larger on top of lithological composition. Darker tints of red indicate older events. Dot sizes reflect earthquake magnitudes, where the largest dot represents a magnitude 9 event. Large events seem to be related to slow ductile flow of lower crust and remnants of oceanic crust inside the subduction channel. **b)** Magnitude distribution of the events, with corresponding logarithmic slopes. Two segments are observed, but both are too flat for a Gutenberg-Richter distribution of events.

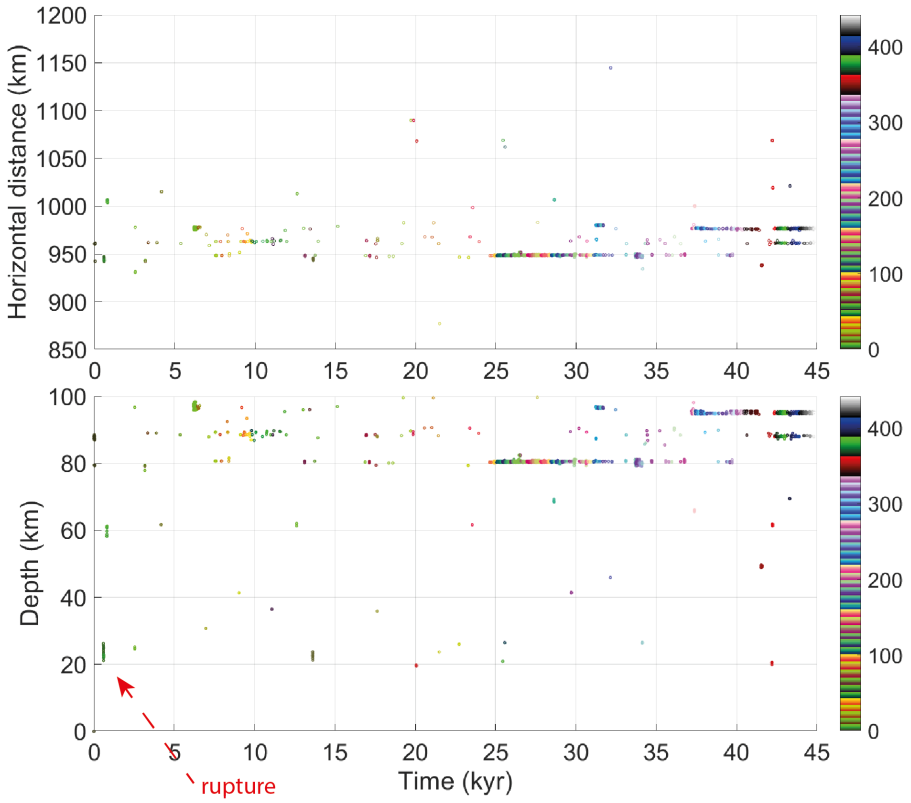

Figure 20: Spatio-temporal evolution of all events registered in the short-term run. The vertical axis depicts both horizontal **(a)** and vertical **(b)**coordinates are both shown. Colours indicate Shallow earthquakes at high elevation have a relatively large vertical rupture component, while many horizontal sequences of "events" are interpreted as slow ductile flow.

of the group of events at X $\approx$ 1020 km and Z $\approx$ 60 km is also unclear, as there is no localised shear zone at that location (Figure 21). However, this area is under extension due to the retreating overriding plate. Only the events in the orogenic wedge top are lined up with a plastic shear zone, directly above the mobile core of the orogen. The ruptures of these faults are largely vertical and the hanging wall is moving down (i.e. normal faults). In addition, the highest parts of the orogen are under extension (Figure 14).

Clearly, deformation in the shallow parts of the simulated orogen and adjacent areas is too ductile to accurately resemble the seismic pattern observed below the Central Alps. This inhibits development of clear plastic shear bands and rapid slip events (i.e. earthquakes). This implies that the upper crust may be either viscously too weak or frictionally too strong. Since the effective friction of the upper crust is already low (Table 2, the former is likely the case.

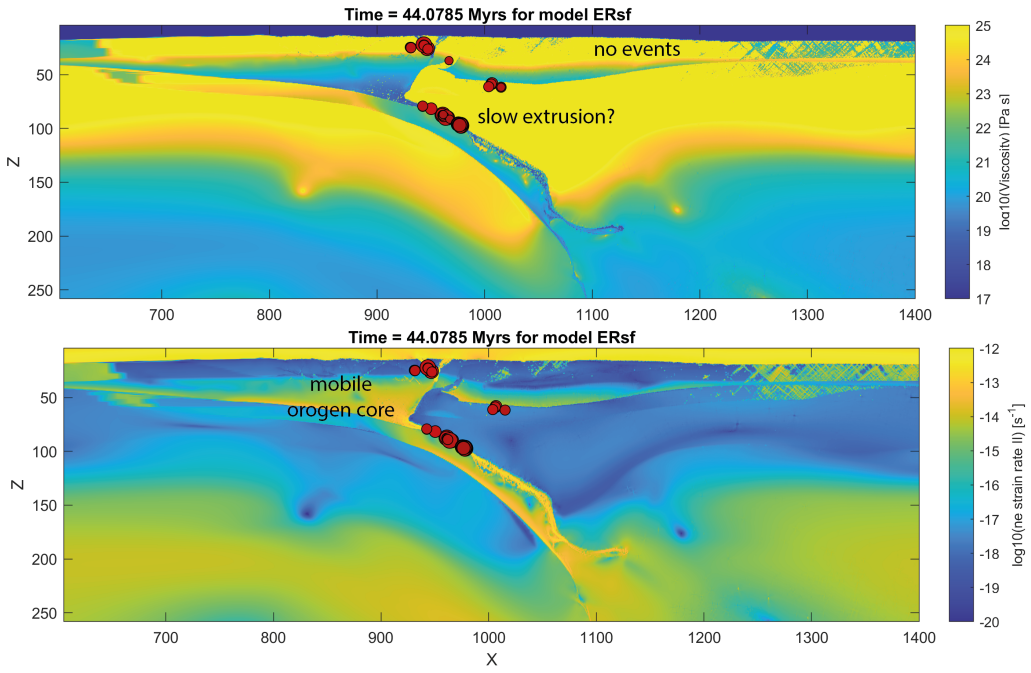

Figure 21: Viscosity and non-elastic strain rates overlain with the seismic events with $M_w > 4$. Strikingly few events occur in the fore- and hinterland.

4.3 Parameter studies

To study the sensitivity of this reference model we systematically investigate the role of various key parameters through making a single change with respect to the reference model ER (Section 4.1). Table 3 provides a brief overview of the parameters studied here. Besides gaining of better understanding of the dynamic controls of continental collision, this parameter study will provide insights into the feasibility and likelihood of the slab roll back orogeny model.

Table 3: Key parameters varied with respect to the reference model ER with brief indication of what how they are different with respect to the reference results. See the respective subsections for details. SVO - single vergent orogen, LC - lower crust, LM - lithospheric mantle

Parameter	reference value	tested values	effects
Slab age	70 Ma	40 (ES), 50 (FV), 60 (FW) and 100 (ET) Ma	younger slabs: lower detachment depth, older slab: detachment at surface
T_{Moho}	450°C	350 (EV), 400 (EU), 500 (EW), 550°C(EX)	only 400-450°C give consistent results
Sed/UC frictional strength	2.1	1.15 (FF), 0.79 (FG), 0.6 (FH)	>> 1: wide retro-shear, ¿ 1: sharp retro-shear, ¡ 1 no retro-shear (i.e. SVO)
LC rheology (both)	mafic granulite	wet plag (FB), wet qtz (FC)	plag: tilted-up overriding LC results in SVO, qtz: early and shallow detachment following near-closure of the subduction channel
LC rheology (overriding)	mafic granulite	wet plag (FD), wet qtz (FE)	plag: like ER, qtz: decoupled behaviour of continental crust and LM
LC thickness	15 km	20 (EZ), 25 km (FA)	Increasingly early and shallow slab detachment
Ocean length	610 km	510 km, 410 km, 310 km	510 km: more indentation, 410 km: early upper crustal delamination, 310 km: asthenosphere window
LM P_f/P_s	0	0.25, 0.50, 0.75	0.25: lower crustal indentation, later detachment, 0.50: early shallow detachment, 0.75: detachment at the surface
Peierls creep	not included	included	shallower, earlier detachment
Weak zone angle	20°	15, 25°	low angle requires longer push, high angle promotes plate decoupling
Weak zone width	20 km	10 and 40 km	≥ 20 km needed for proper subduction initiation
Decoupled boundaries	fixed lower plate	both plates free	accelerated subduction, plate decoupling

4.4 Slab age

Slab age is a crucial parameter to systematically investigate, since it determines the slab temperature distribution and thereby its negative buoyancy. Its clearest effect is on the timing and depth of detachment. A ”young” slab (i.e. 50 Ma or less) results in shallow and early detachment, while 60 Ma or older slabs lead to deep and late detachment (Figure 22). The younger slabs are also warmer and therefore weaker than older slabs. During wedge emplacement, some shear deformation occurs at the ocean-continent transition, as the heavy oceanic slab pulls on the sub-horizontal passive margin (Figure 23). While older slabs are strong enough to maintain their integrity, it seems that young slabs are too weak to resist this shearing (Figure 23). As a consequence, once this threshold has been passed timing and depth of slab detachment change little between models with young slabs. For example, a 40 Ma and a 50 Ma give very similar results, i.e. detachment at 100 and 108 km depth, with a respective timing of 5.8 Myr and 6.4 Myr. The accretionary wedge in these young slab models displays more

regular, in-sequence thrusting than the reference model. Interestingly, a 60 Ma oceanic plate yields detachment dynamics comparable to the 70 Ma reference model, i.e. convective separation at the 660 km discontinuity and late detachment at about 380 km depth. However, the upward rebound occurs simultaneously with detachment, instead of afterwards. Secondly, rebound-induced upward flow of upper crust inside the orogen occurs in the vertical direction due to heavier oceanic material at the base of the retro-shear. Therefore, the push on the overriding plate is smaller and the orogen advances only 10 km instead of 40 km.

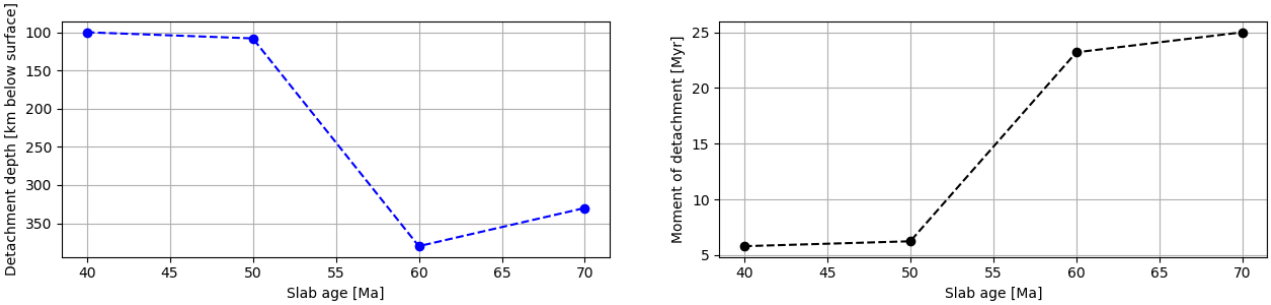

Figure 22: Depth and timing of detachment as a function of slab age, for the limited range tested here.

Surprisingly, increasing the slab age to 100 Ma leads to detachment at the surface. This could be a result of the fixed lower plate boundary condition that together with a heavy slab generates large extensional stresses in the lower plate for an extended period of time which lead to cross-lithosphere extension (Figure 24). It is left out of Figure 22, because this surface detachment is a consequence of boundary conditions and not of natural processes. Prior to detachment, the lower plate upper and lower crust show slightly more plastic yielding than the reference model. However, the largest difference is the symmetric distributed deformation, i.e. pure shear extension, in the lithospheric mantle that announces the surface detachment (Figure 24).

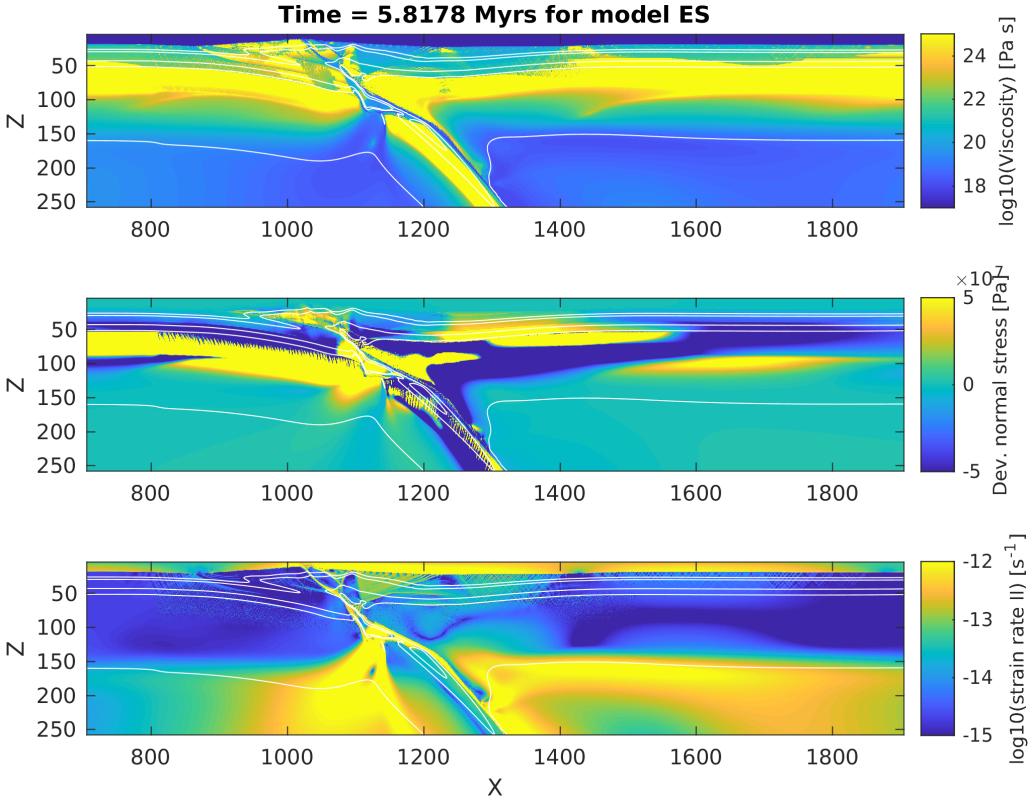

Figure 23: Model ES (slab age 40 Ma) at the moment of slab detachment. Detachment occurs through rapid plastic tearing at a shallow depth of 100 km. The remaining slab is too small to sustain convergence after detachment. A slab age of 50 Ma gives similar results.

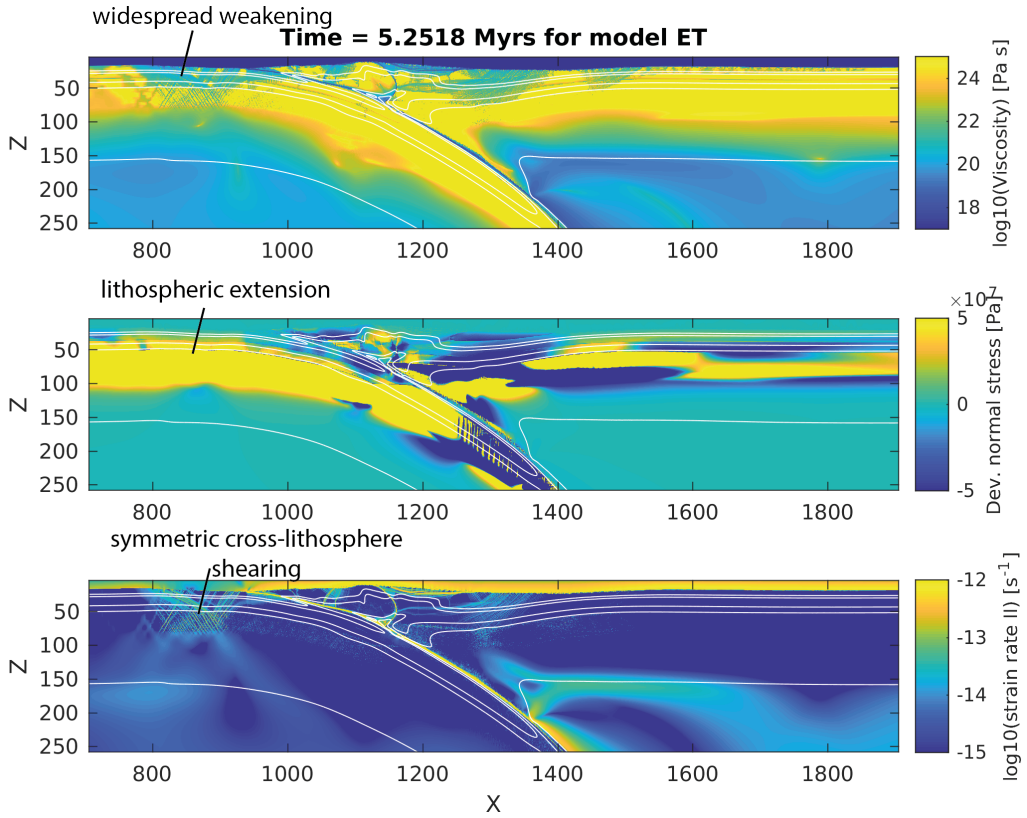

Figure 24: Model ET (slab age 100 Ma) shortly after the kinematic convergence stage, shortly before detachment at the surface to illustrate how the detachment occurs, i.e. symmetric lithospheric extension.

4.5 Moho temperature

Slab age influences the oceanic geotherm, and hence the ductile and elastic strength of the oceanic slab. In continents, more factors control the thermal structure, such as lithology-dependent radiogenic heat production and heat conduction. The continental geotherm is changed here using different Moho temperatures. A colder lithosphere through a reduced Moho temperature will lead to higher effective viscosities due to the temperature dependence of the dislocation and diffusion creep mechanisms (equations 15 and 16). The higher viscosity also increases the elastic strength, which makes slab bending more energy-consuming and potentially slowing down subduction (Fourel et al., 2014). Increasing crustal viscosities should result in more localised, brittle/plastic deformation and generally stronger continents. Vice versa, a hotter continental crust should decrease the effective viscosity, thereby promoting ductile and distributed deformation.

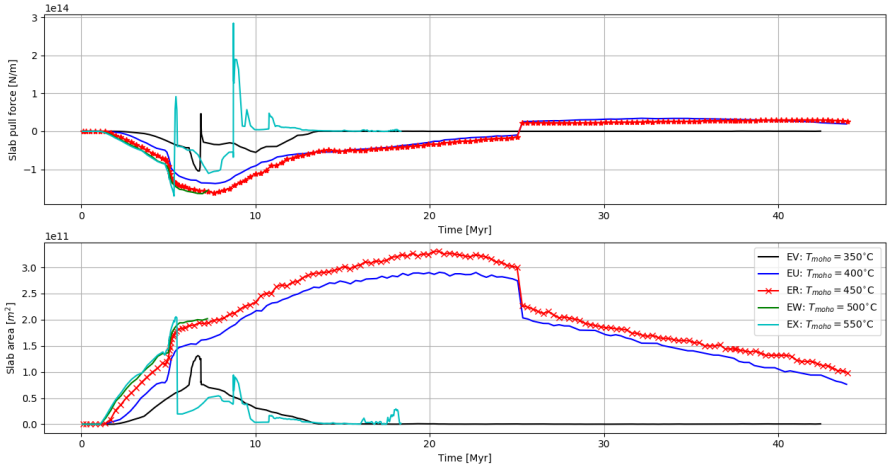

Figure 25: Slab pull and area evolution for models EV, EU, EW and EX with Moho temperatures of 350°C, 400°C, 500°C and 550 °C, respectively. They are compared to the reference model ER which has a Moho temperature of 450°C.

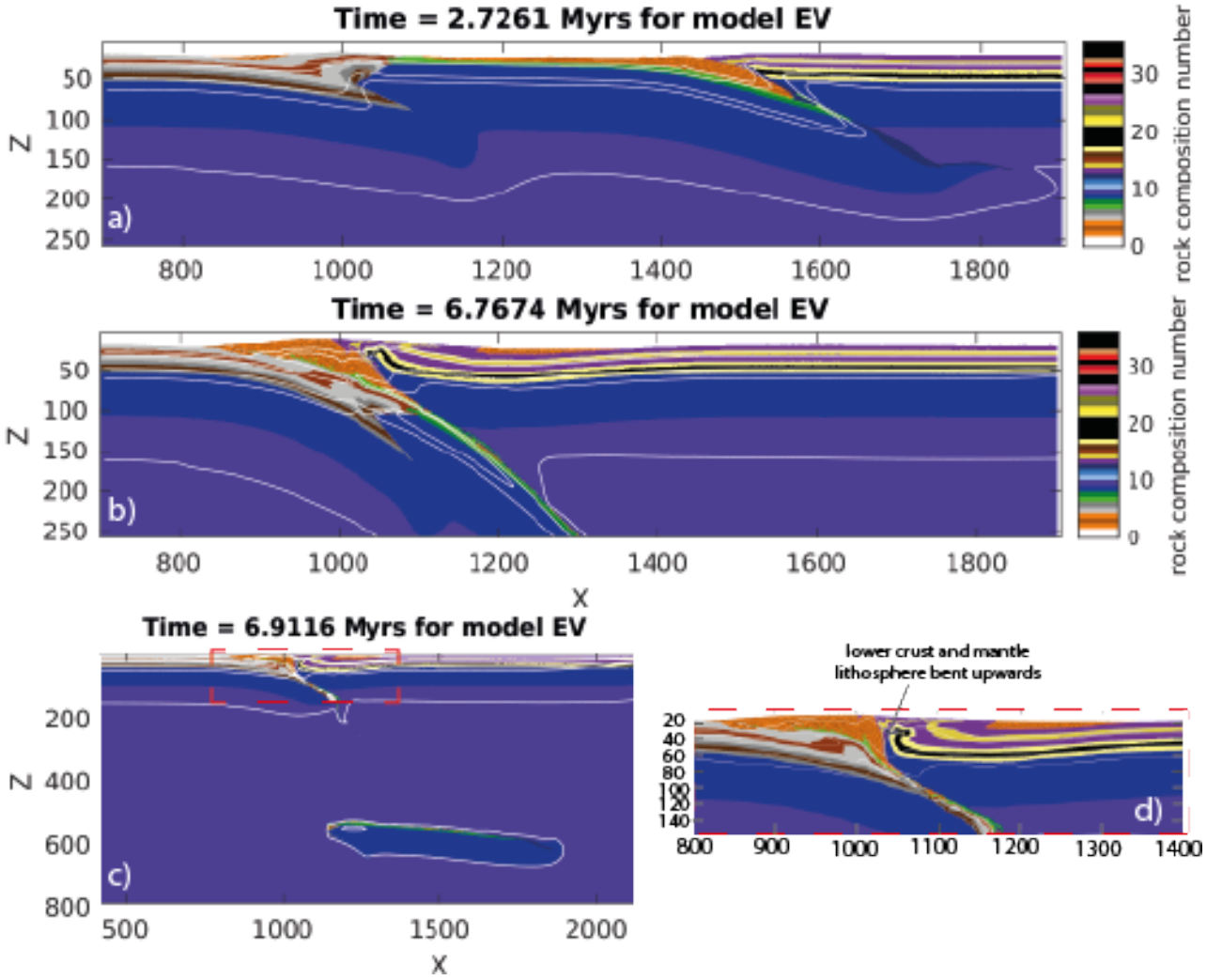

Figure 26: Temporal evolution of model EV, which shows double subduction **a)** The second subduction zone has taken over around 1.2 Myr **b)** The loading exerted by the accretionary wedge pushes the continental margin down. **c)** Shortly after, the slab has detached along the first subduction interface. **d)** The tip of the overriding plate is rotated to a vertical position. No pronounced retro-shear is visible.

The range of Moho temperatures investigated here shows highly variable slab dynamics (Figure 25). The coldest Moho model develops two subduction zones (Figure 26), resulting in a slow accumulation of slab pull and area. In this case the weak zone is not thick enough to initialise subduction (see section 3.4). In addition, the retro-foreland basin is much shallower compared to the reference model (Figures 10, 26b)

Increasing the Moho temperature to 400°C gives modelling results that resemble those of the reference model (T_{Moho} = 450°C, Figure 25). The results of the model with a Moho temperature of 500°C show that the overriding plate bends more easily leading to a deeper, narrower retro-foreland basin (Figure 27). Increasing the Moho temperature to 550°C lead to detachment at the surface, as the plate loses its integrity. As soon as the left continent is overthrust by the accretionary wedge, large extensional stresses dominate throughout the lower plate, swiftly followed by symmetric rifting and detachment. The highly oscillatory slab pull pattern after detachment at 5.3 Myr (Figure 25) is caused by dripping effects.

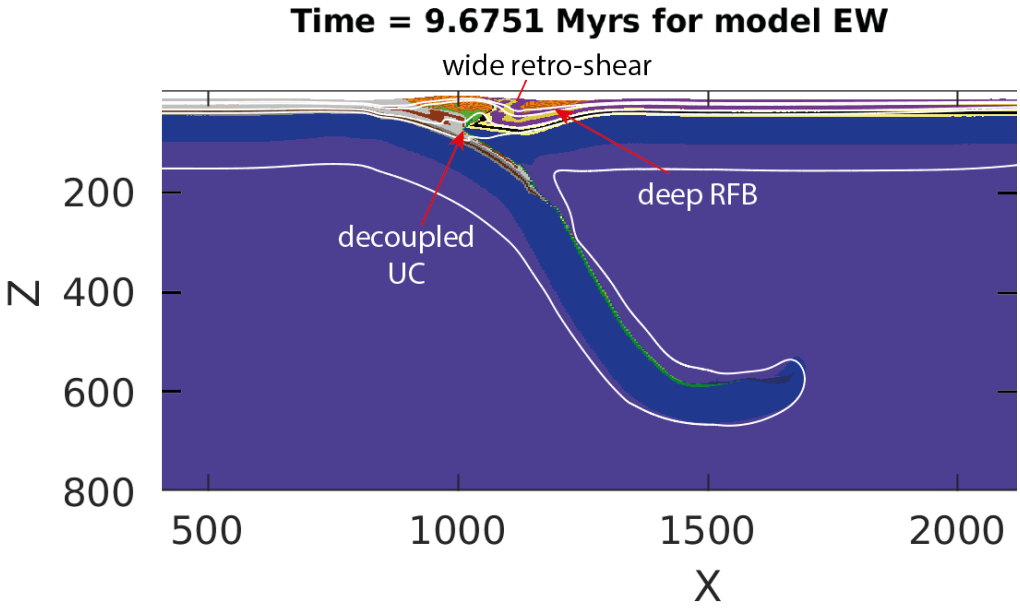

Figure 27: Model EW with a Moho temperature of 500°Cat its latest time step. A highly double-vergent orogen has developed with a wide but pronounced retro-shear. The retro-foreland basin (RFB) is deeper than in the reference model.

In particular, a Moho temperature of 500°C has some interesting characteristics that should be noted: as opposed to the reference 450°CMoho, the lower plate upper continental crust flows back along the subduction interface much easier. Much less continental crust enters the subduction zone during wedge emplacement. After reaching 100 km depth at 7.4 Myr, the positive buoyancy of the downgoing upper crust overcomes the weak coupling between the upper and lower crust, triggering delamination and generating a wide reverse shear zone (Figure 27). The decreased viscosity of the overriding plate also results in a deep and narrow retro-foreland basin, since it reduces the elastic strength and therefore the wavelength of deflection. A hotter lithosphere appears to counter upper crustal subduction and to promote a deep and asymmetric retro-foreland basin. The effect of the higher Moho temperature on the timing and depth of detachment remains speculative, but the early return flow of upper crust may postpone slab detachment by reducing the positive buoyancy component. Furthermore, the early upper crustal delamination results in a highly double-vergent orogen.

4.6 Upper crustal friction

The maximum frictional strength of sediments for a reference pressure of 100 MPa in the reference model is 2.1 times as high as that of the upper crust. This was first done to resolve an issue where too many sediments entered the subduction zone, which in turn weakened the plate interface significantly. In those cases the upper and lower plates decoupled and asthenosphere replaced the material below the orogen. This is referred to as an asthenosphere window. With respect to the current reference model ER, the upper crust effective friction coefficient was doubled (model FF), tripled (model FG) and quadrupled (model FH) to decrease the sediment/upper crust strength ratio. The resulting ratios are 1.15, 0.79 and 0.6, respectively. When the

sediments/upper crust frictional strength ratio is smaller than the threshold value of approximately 1, no retro-shear develops and a retro-foreland basin forms that is shallower and wider than in the reference model (Figure 28). On the other hand, the retro-shear is sharply defined when the sed/UC ratio slightly exceeds 1, i.e. in model FF (Table 3).

Decreasing the sediments/upper crustal frictional strength ratio by increasing the upper crustal friction results in relatively subtle differences with respect to the reference model. They are subtle, because the slab dynamics are only slightly affected by the varying upper crustal strength in the investigated model time (12 Myr). However, in earlier models an asthenosphere window invariably formed when the upper crust comes in extensive contact with asthenosphere. This can thus be expected to happen in models FG and FH as well. One subtle difference concerns the position of the upper crust of the overriding plate. The upper plate-accretionary wedge boundary, acting as a backstop, dips with $\approx 60^{\circ}$ at 5 Myr in the reference model. In the models with progressively stronger upper crusts, this interface is much gentler. The sharp retro-shear develops in model FF (sed/UC ratio 1.15) when the wedge is emplaced on top of the downgoing plate, as the sediments in the orogen are about as strong as the crust. This results in burial of the upper plate lower crust to about 60 km depth. In contrast, the lower crust is positioned much shallower in models with a relatively strong upper crust (Figure 28c-e). Furthermore, the overriding lithospheric mantle is not able to scrape the subducting, strong upper crust off in these models with a sed/UC ratio ¡ 1. This upper crustal resistance to indentation and off-scraping by the overriding lithospheric mantle suggests the existence of a threshold strength ratio between upper (continental) crust and lithospheric mantle of 0.3. The result is a single-vergent orogen with a shallow and wide retro-foreland basin.

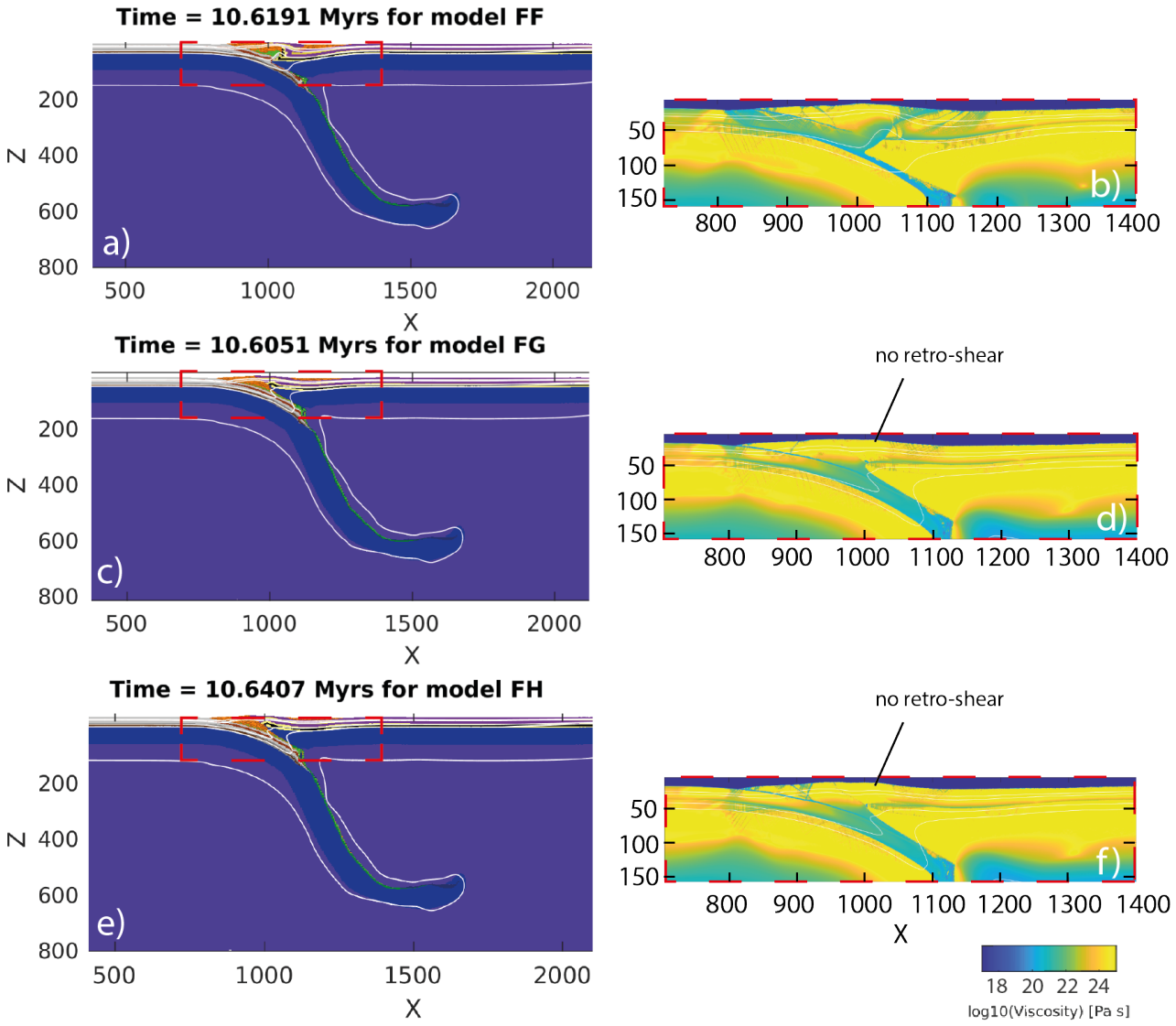

Figure 28: Role of sediment vs. upper crustal friction ratio. All three were run only to 12 Myr. Composition figures with viscosity insets (b, d and f) at $t \approx 10.6$ Myr for models with sediments/upper crust frictional strength ratios 1.15 **(a)**, 0.79 **(c)** and 0.60 **(e)**. The models with a relatively strong upper crusts(**(c-f)** lack a retro-shear, i.e. an inclined low viscosity zone on the right of the orogen is missing. In addition, upper crustal delamination has not happened (yet) in models FG and FH either.

4.7 Lower crustal rheology

The reference rheology of both continental lower crusts (mafic granulite, Table 2) is the strongest possible material for this layer. Replacing it by a weaker material such as plagioclase or wet quartzite is expected to affect the ductile behaviour of the lower crust (Figure 29). The decreased ductile strength will increase the coupling to the weak wet quartzite upper crust, but decrease the coupling to the lithospheric mantle.

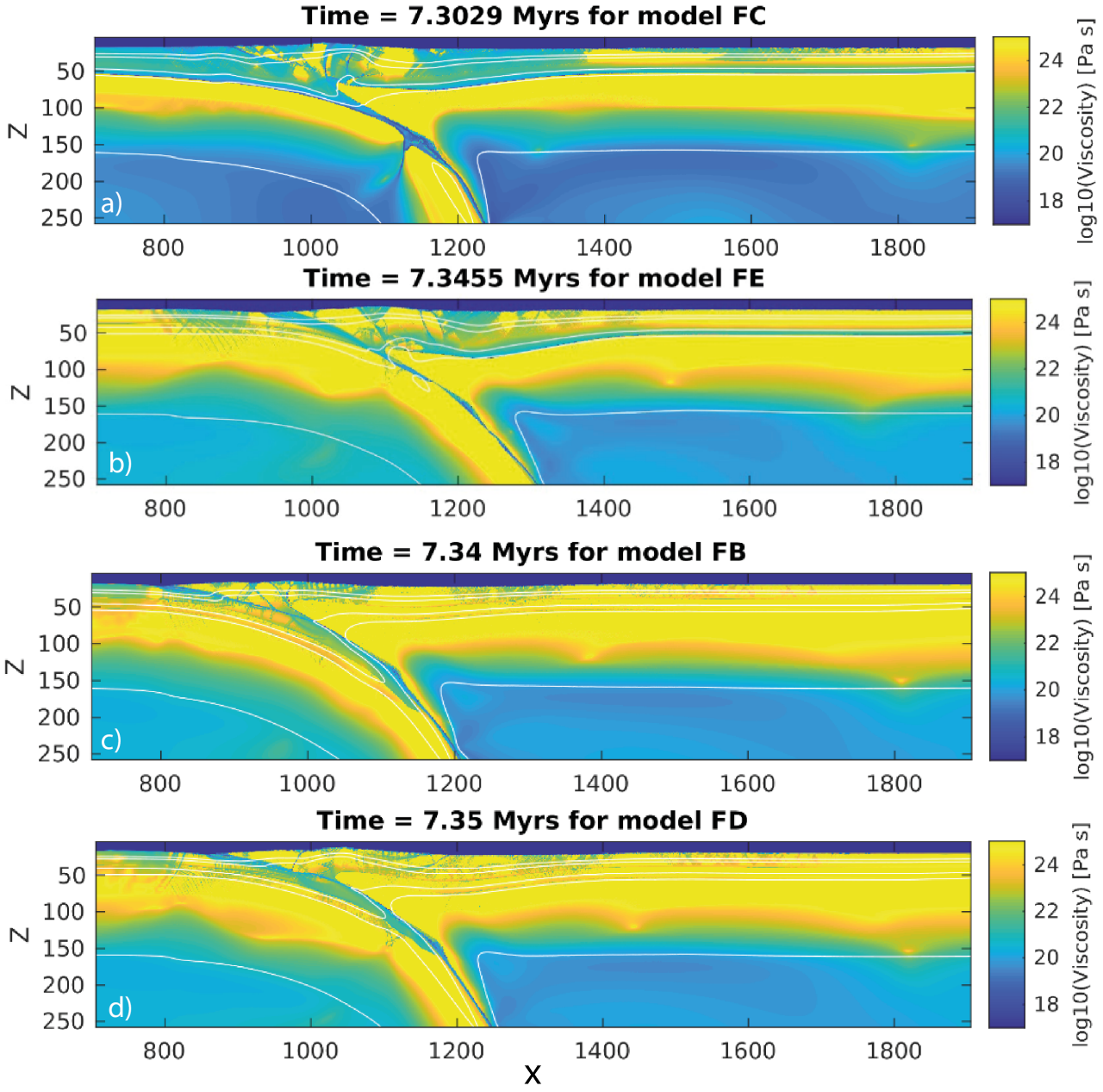

Figure 29: Role of lower crustal rheology. **a)** Wet quartzite in both continental lower crusts results in a very weak orogen. Note the on-going slab detachment, which occurs through fast plastic shearing. **b)** In case of wet quartzite lower crust only in the overriding plate, the orogen, downgoing plate and overriding plates are much stronger. **c)** If both lower crusts are made of plagioclase, the downgoing upper crust remains coupled to the lower crust while the hinterland is characterised by a shallow, wide retro-foreland basin. **d)** When only the upper plate lower crust consists of plagioclase, the dynamics and viscosity are very similar to the reference model.

In the case when the ductile strength of the lower crust is reduced from a mafic granulite flow law to a plagioclase flow law a number of differences arise (Figure 29). Firstly, in the initial stage the slab is more smoothly curved than in the reference model (compare Figure 10a and Figure 31a). A curved slab gives a larger contribution of lithospheric mantle material to the slab pull calculation than a kinked slab (as in the reference

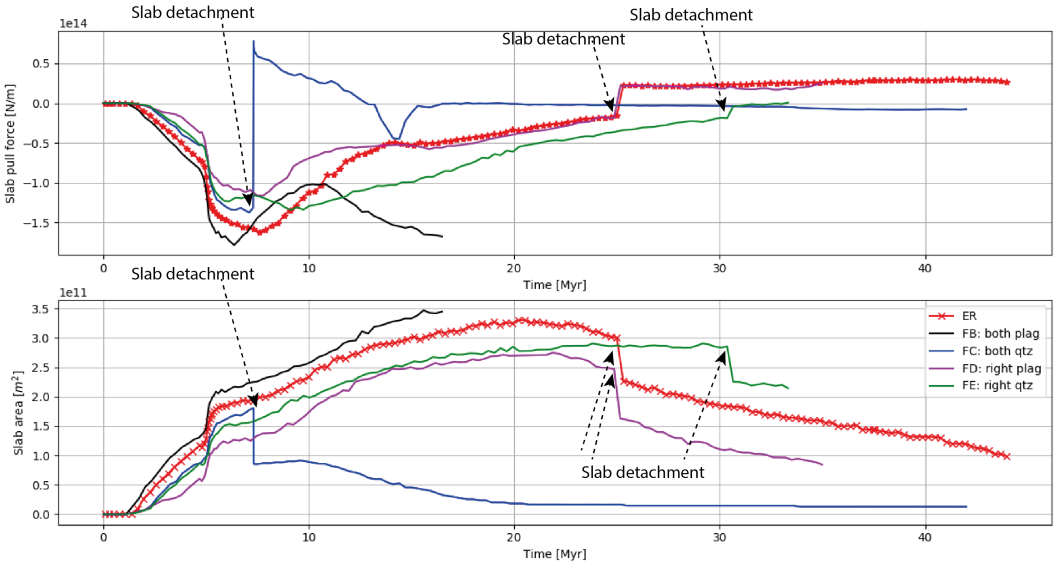

Figure 30: Slab pull evolution for different lower crustal rheologies. The slab detaches early in model FC. Strikingly, the slab pull force of model FD almost exactly follows that of the reference model after $t \approx 14$ Myr while the area is less. In the whole duration of model FE (right continent wet quartzite lower crust) the slab pull is negative.

model). The more curved slab seems to be a consequence of the upward tilted position of the lower crust of the overriding plate, which acts as a funnel for oceanic crust and wedge sediments into the subduction channel. The tilted crust also results in a single-vergent orogen (Figure 31a-b and 29c). The subduction of extra oceanic crust leads to a peak slab pull exceeding that of the reference model (Figure 30). Secondly, the slab pull first decreases after the push is released (as buoyant and upper continental crust subduct), but increases in magnitude again after $t = 11$ Myr (Figure 30) coeval with the onset of rapid delamination and upward flow of upper crust from the downgoing plate. This leads to an increased trench retreat in the intermediate stages of the model.

When the overriding continental lower crust is composed of plagioclase, the modelling results are extremely similar to the reference model (Figures 29d and 12a). While initially the subduction is slightly slower than in the reference model, the pattern of trench retreat followed by slab detachment at $t = 25$ Myr (Figure 30) including subsequent rebound of 40 km is the same in both cases. Only minor differences in geometry within the orogen can be distinguished. For example, the upper crust seems to stay in the core of the orogen, where it moves along the retro-shear in the reference model. These minor differences suggest that lower crustal rheology in the overriding plays a relatively minor role in dynamic continental collision.

In the weakest ductile strength configuration with both lower crusts consisting of wet quartzite the model dynamics are very different from the reference model. Since the ductile strength of wet quartzite is low, the lower plate has little resistance against the indenting strong lithospheric mantle. As a consequence, the lithospheric mantle nearly closes the subduction channel. In combination with the weak transition between continent and ocean, this strongly promotes slab detachment along this interface. The slab indeed detaches at 7.31 Myr at a depth of 130 km (Figure 29a). After detachment, the remaining slab immediately rebounds (Figure 30). At the same time, the overriding plate slides off the weak remains of the subduction channel. This induces slow extension inside the orogen, continuing to $t \approx 20$ Myr. A weak orogen can thus be characterised by a low surface topography and pervasive extension.

On the other hand, when only the right continental lower crust is composed of wet quartzite no early, shallow detachment occurs. The slab pull remains negative during almost the entire simulation (Figure 30). Interestingly, no retro-foreland basin forms, because the weak overriding crust is shortened in pure shear sense during the build-up of the accretionary wedge. As more shortening is accommodated by the overriding plate, the trench retreats less than in other models. In addition, the upper crust of the downgoing plate decouples easily from the downgoing plate when the continents collide at $t = 8$ Myr (Figure 32).

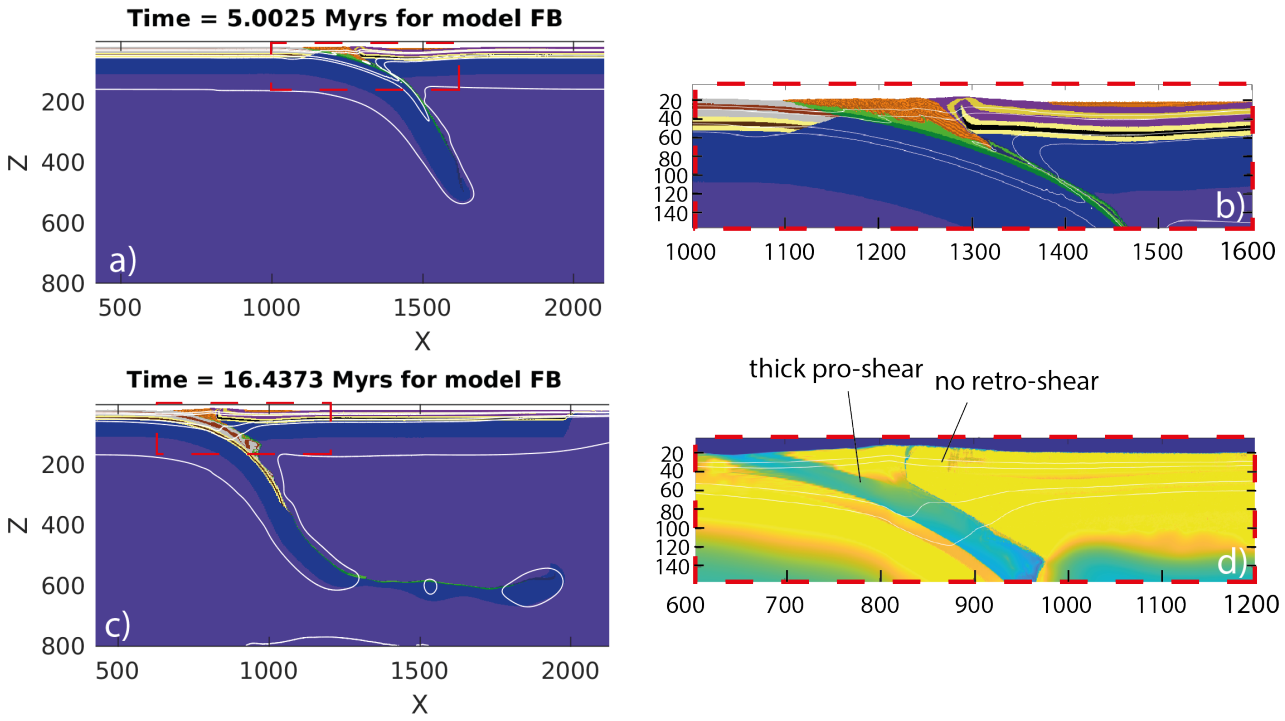

Figure 31: **a-b)** Model FB (both LC plagioclase) after the kinematic convergence stage. The upper plate lower crust is tilted upward resulting in a single-vergent orogen. **c-d)** Model FB at an intermediate stage. The viscosity inset shows that there is indeed no retro-shear as in Figure 12. The upper crust in the subduction channel has started to buoyantly flow upward.

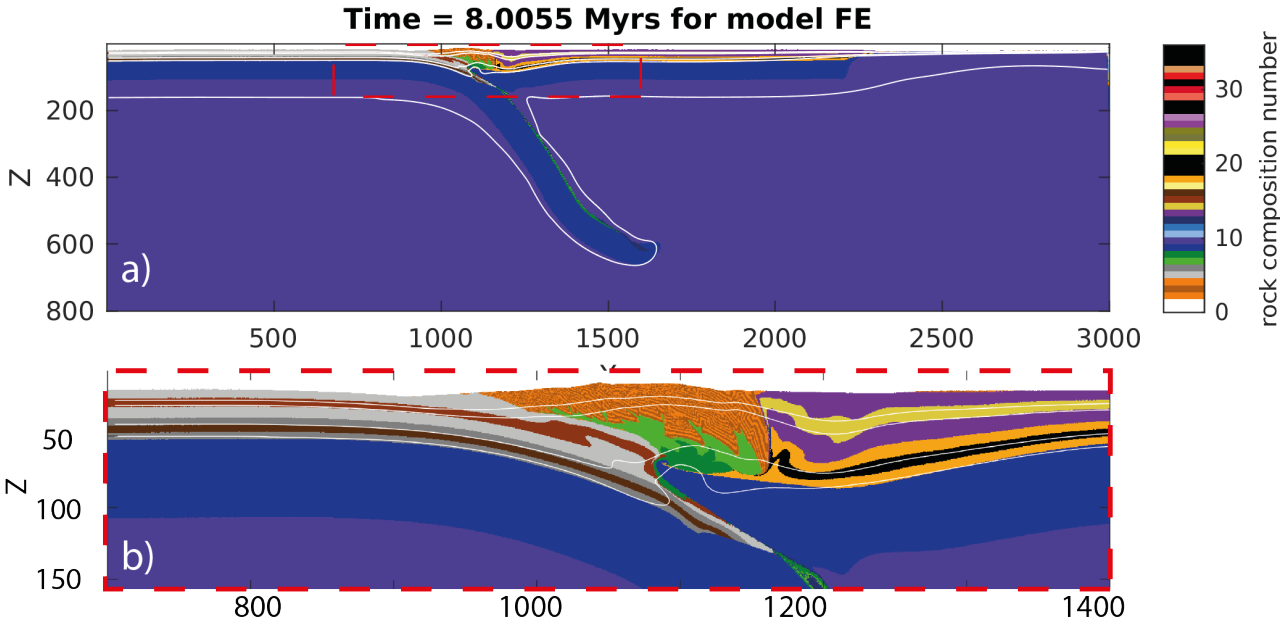

Figure 32: The continental crust is prevented from entering the subduction channel by the lithospheric mantle of the overriding plate. Secondly, the upper crust has accommodated some of the shortening by thickening.

The role of the lower crustal rheology in continental collision thus differs for the overriding and down-going plate. Lower crustal subduction only occurs if the lower crust is intermediate or strong, as it needs to resist the incoming lithospheric mantle of the overriding plate. The overriding plate lower crust needs to be strong to develop a double-vergent orogen. Both a plagioclase and a wet quartzite rheology in the overriding plate lower crust promote the development of a single-vergent orogen, but through completely different mechanisms (tilting versus pure-shear thickening of the overriding crust).

4.8 Lower crustal thickness

In addition to the rheology and corresponding material parameters, the thickness of the lower crust has an influence on the ductile and elastic strength of the continents. A thicker crust with an unchanged LAB depth means that the lower crust reaches higher depths (not temperatures, because the same T_{Moho} is used), where material is weaker through the dependence of dislocation creep on dynamic pressure (Equation 22). Therefore, increasing the thickness may lead to more decoupling between the crust and the strong lithospheric mantle. Models EZ (20 km lower crust) and FA (25 km lower crust) were set up to test this. One effect of increasing the lower crustal thickness is a slower build-up of slab pull and area (Figure 33). At the end of the kinematic stage, the slabs dip 60° (reference), 50° and 45°. In addition, the slab detaches much earlier and shallower than in the reference model (Figure 34). In case of a 20 km thick lower crust this occurs through very rapid tearing after 9.9 Myr at a depth of 150 km. When the lower crust is 25 km thick, the slab detaches at an even shallower depth of 90 km at $t \approx 5.6$ Myr. It is not fully clear why the slabs detach so soon and at such shallow depths in these models. Both models do not show significant differences in stresses in the period before detachment. The thicker lower crust effectively replaces a portion of strong lithospheric mantle with weaker lower crust (Figure 34). This reduces the effective viscosity, thereby reducing resistance to the shear stresses generated by 1) the slab steepening and 2) the trenchward motion of the overriding plate. Finally, the expected increase in decoupling between crust and mantle was not observed, possibly because the slabs detach before crustal delamination occurs. In summary, a thicker lower continental crust weakens the down-going plate resulting in early and shallow slab detachment.

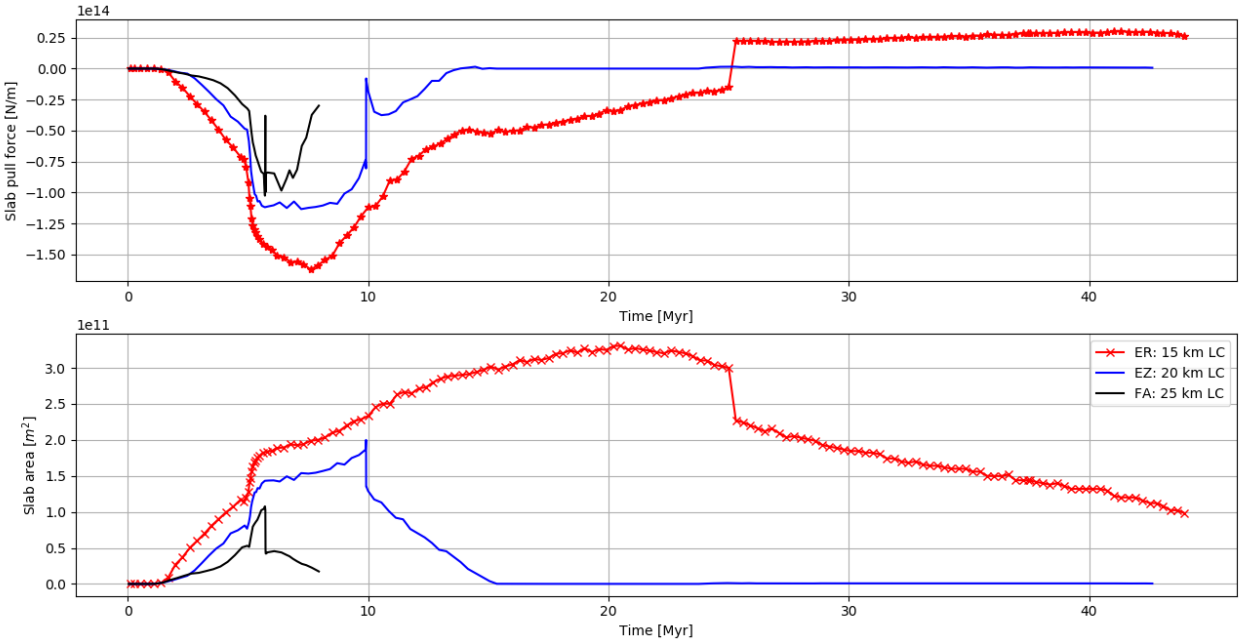

Figure 33: Slab pull evolution for models with lower crustal thickness of 15 km (reference), 20 km and 25 km. Increasing the lower crustal thickness leads to early and shallow slab detachment.

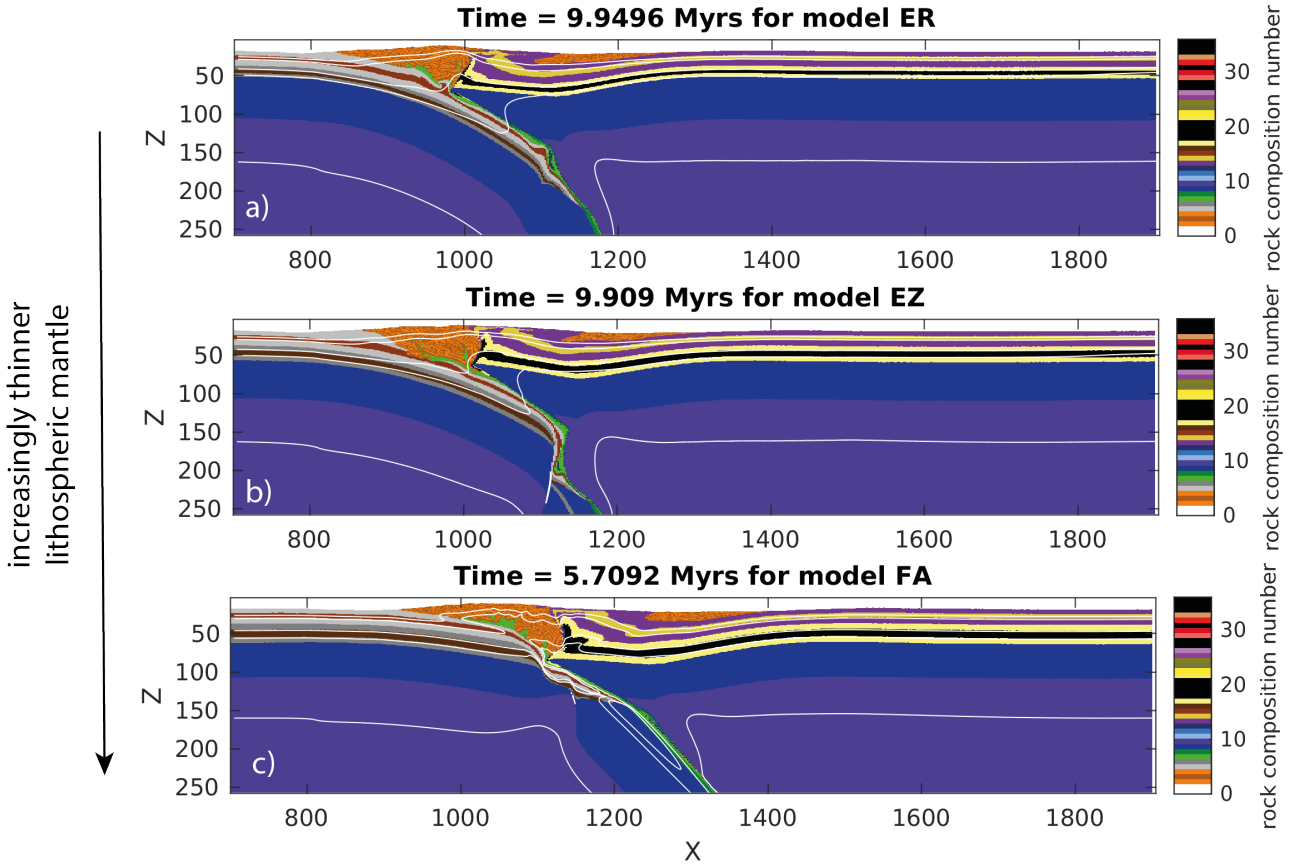

Figure 34: Role of lower crustal thickness on slab detachment. **a)** The reference model with a 15 km thick lower crust, **b)** A 20 km thick lower crust leads to slab detachment at 130 km depth. **c)** A 25 km thick lower crust results results in even earlier and shallower slab detachment

4.9 Ocean length

A very basic but vital parameter in continental collision setups is the length of the oceanic plate initially present between converging continents. It determines many things, among which are the negative component of slab pull, the timing of continental collision and the position of the relatively weak ocean-continent transition. The ocean length was decreased to 510 km, 410 km and 310 km (Table 3). Since a push is applied for 5 Myr in this research, a shorter ocean implies that continental collision and/or subduction is forced. Each case appears to have its own signature, as shown below.

In short, decreasing the ocean length while keeping the push duration unchanged gives insight in how imposed kinematic boundary conditions influence model dynamics. Increasingly early forced emplacement of the accretionary wedge on top of the overriding plate leads to more upper crustal subduction. This in turn changes the timing and depth of detachment (earlier and slightly shallower) and leads to different orogenic architectures (Figure 35). If the ocean is very short (310 km), upper crustal delamination and exhumation creates an asthenosphere window.

Decreasing the ocean length from the reference value of 610 km to 510 km produces similar results in terms of forces (Figures 36 and 37). Continental material enters the subduction zone earlier, so the magnitude of slab pull decreases earlier as well. However, the down-going upper crust is indented by the overiding lithospheric mantle, where it is compressed by the downgoing and overriding lithospheric mantles in the reference model (Figure 11). This promotes formation of a retro-shear and displacement of crustal material along it (Figure 35c-d), which induces uplift of the orogen and decoupling of the upper from the lower crust in the overriding plate. This in turn increases the topographic load and buries the indenting plate. By t = 19.5 Myr, the lower crust has indented the orogenic core as well (Figure 35c). Slab detachment occurs slightly later than in the reference model, but the behaviour after detachment is what distinguishes this model from the rest.

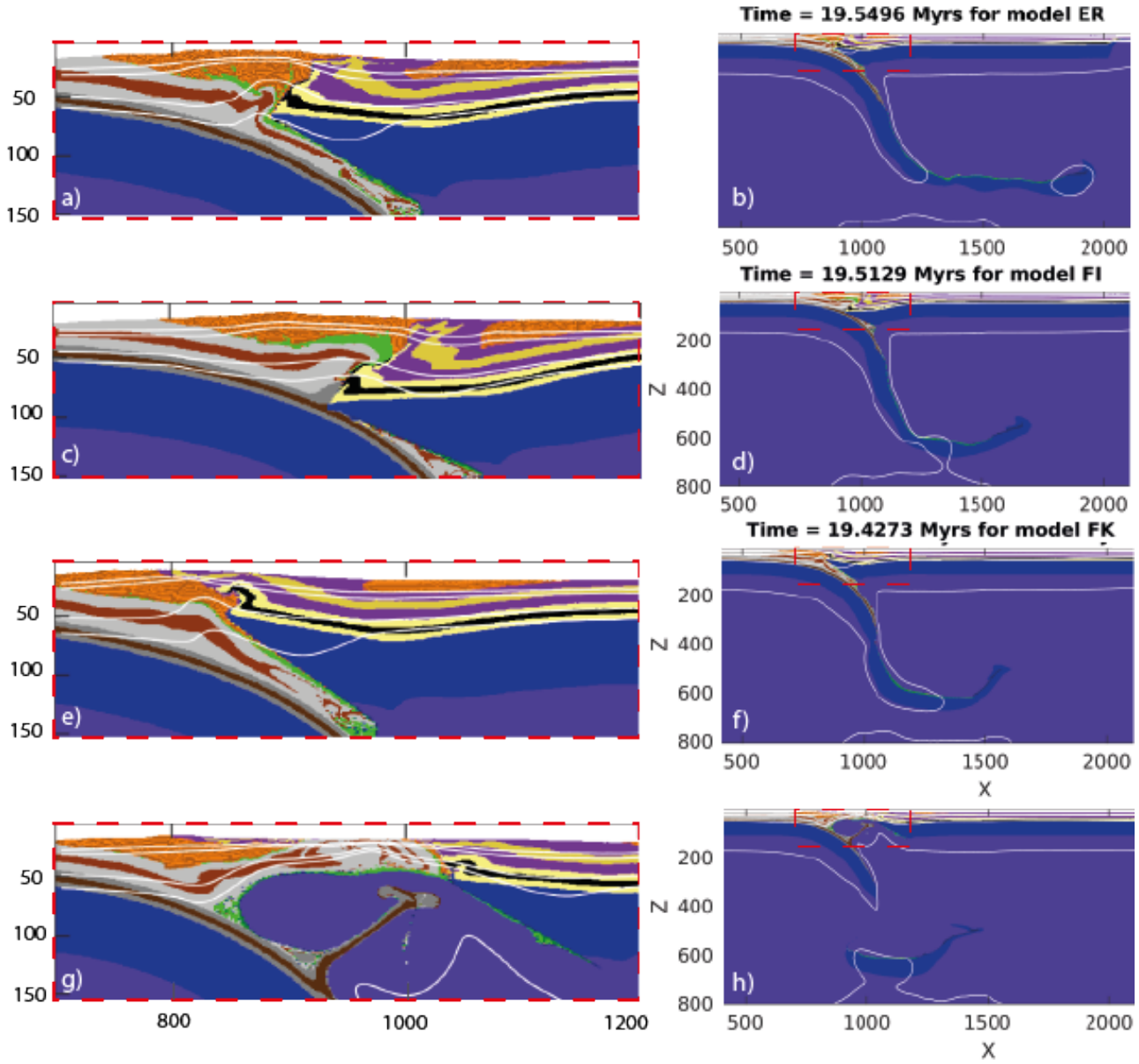

Figure 35: Composition of the reference model (610 km ocean) with models FI, FJ and FK with 510 km, 410 km and 310 km long oceanic plates, around 19.5 Myr. **a-b)** Upper crustal material is starting to exhume along the retro-shear. **c-d)** A large amount of continental upper crust, along with some lower crust, are being displaced along the prominent retro-shear, caused by the indentation by the lithospheric mantle. The retro-foreland basin is narrow and deep. **e-f)** Buoyant flow of upper crustal material has just started, while the slab is necking at depth. Note the upward position of the overriding plate tip and the shallow retro-foreland basin. **g-h)** An asthenospheric window has formed following crustal delamination. Additionally, the slab has rebounded by 20 km after detachment.

At t = 35 Myr, the slab pull becomes negative (Figure 36). When the slab starts to pull down, stresses near the subduction channel start to change from compressional to extensional, facilitating slow delamination of the lower crustal material that was trapped before (Movie S3). This lower crustal delamination is not observed in the reference model. The upward flow of lower crust induces minor amounts of uplift and extension of the orogen, which pushes the overriding plate to the right (Movie S3). This in turn enhances mantle flow to the right below the overriding plate. However, in contrast with the reference model some extension is observed to the left as well, which generates some 40 km of post-collisional trench retreat (Figure 38).

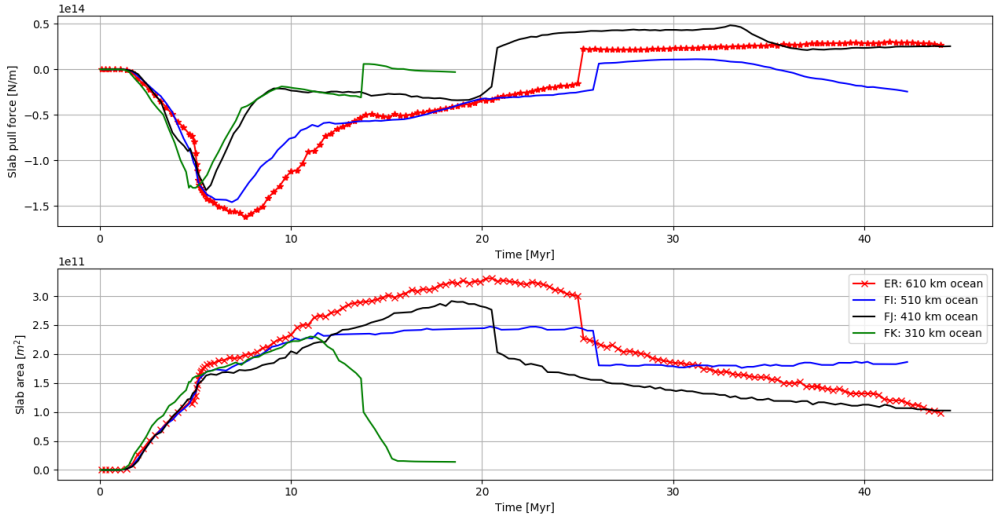

Figure 36: Visualisation of slab pull for ocean lengths of 610 km (reference), 510 km, 410 km and 310 km. A slightly shorter ocean (black line) gives reference-like results.

When decreasing the ocean length further, the forced convergence has more effects. Initially, models with ocean lengths of 410 and 310 km display very similar behaviour during the kinematic convergence stage (Figures 36 and 37). Instead of accelerating due to slab steepening-induced mantle flow, the wedge is being forced on top the left continent. The forced trenchward motion of the overriding plate prevents formation of a retro-shear. In both models the upper crust is not separated from the lower crust, so it reaches sub-lithospheric depths. Therefore, when the push is released the drag is larger than the slab pull (right panels in Figure 37). The slab pull diminishes to $-2.5 \cdot 10^{13}$ N/m just before 10 Myr is reached in both cases. Hereafter the models diverge.

For the case of an ocean length of 410 km (FJ) the collisional system slowly retreats between t = 10 and t = 16 Myr. The drag switches polarity at $t \approx 17.5$ Myr, indicating that subduction slows down and slab detachment is imminent. Indeed, the slab starts to neck at the ocean-continent transition at 380 km depth (Figure 35d), where it detaches around t = 20.5 Myr. The slab pull remains positive and dominant over the rightward drag for the rest of the simulation (Figure 36) . In the case of a 310 km long ocean, the continental upper crust delaminates from the subducting lower crust around 10.2 Myr and rapidly flows back into the core of the orogen. This material is immediately replaced by asthenosphere that heats up the orogen and generates extension. At the onset of extension around t = 13 Myr the slab detaches at the ocean-continent transition at 380 km depth. The slab rebounds during the next 3 Myr, by which point enough continental material has moved back to lithospheric levels to balance the buoyancy of the slab (Figure 35g-h).

These results indicate that the initial length of the oceanic plate present between the two converging continents does indeed exert a large control on the geometry of the resulting orogen. Longer oceanic plates seem to promote development of a double-vergent orogen.

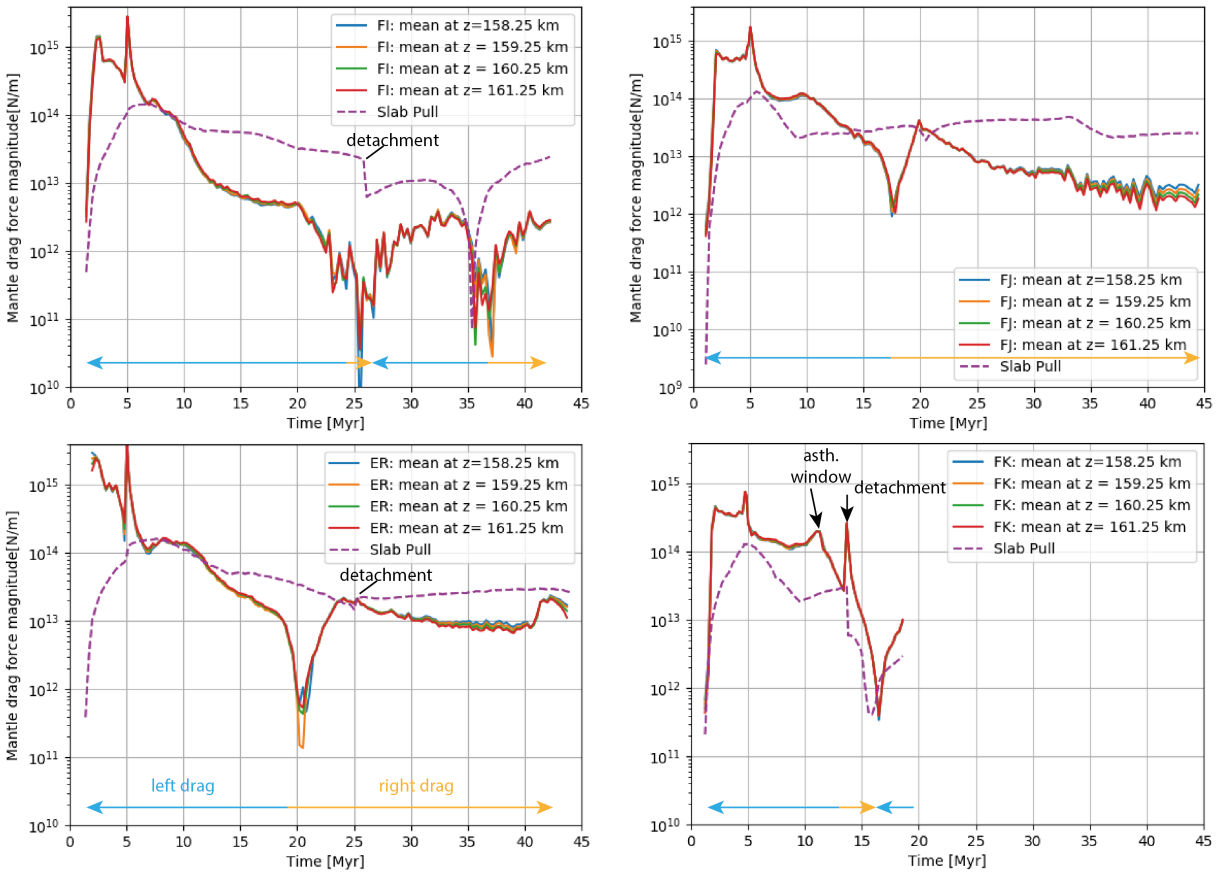

Figure 37: Mantle drag and slab pull magnitudes for various ocean lengths. ER (reference) 610 km long ocean, FI: 510 km ocean, FJ: 410 km ocean, FK: 310 km long oceanic plate. Drag directions are signified by the blue and yellow arrows.

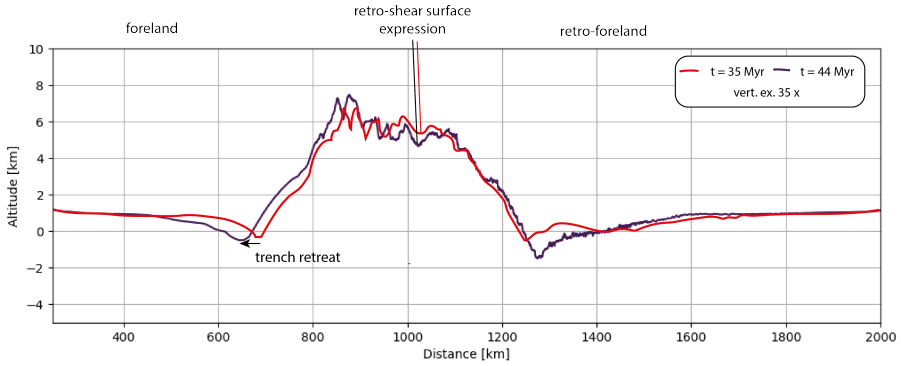

Figure 38: Topographic signature before and in a late stage of lower crustal delamination showing almost 40 km of trench retreat generated by orogenic extension.

4.10 Lithospheric mantle friction

In the reference model, the upper part of the lithospheric mantle of the down-going plate is characterised by large (on the order of 1 GPa) tectonic underpressures (Figure 11, which is thought to be a consequence of extension induced by bending of a rheologically strong slab (Burg and Gerya, 2005; Gerya, 2015). In addition, overpressures are present in the overriding lithospheric mantle due to compression in that area (Figure 12b) The pressure in the subduction channel itself follows a lithostatic pattern (compare e.g. the pressure at $z = 100 - 150$ km and $x = 700$ km with the subduction channel in Figure 11, which is in line with previous findings (Burov and Yamato, 2008). This dynamic pressure variation facilitates delamination and buoyant flow of crustal material. In Section 4.6 it has already been shown that a frictionally stronger continental upper crust better resists the pressure from the lithospheric mantle. Since the effective friction coefficient of the reference lithospheric mantle is about 10 times as high as that of the continental upper crust, it is useful to explore the behaviour of the model when the lithospheric mantle is weaker.

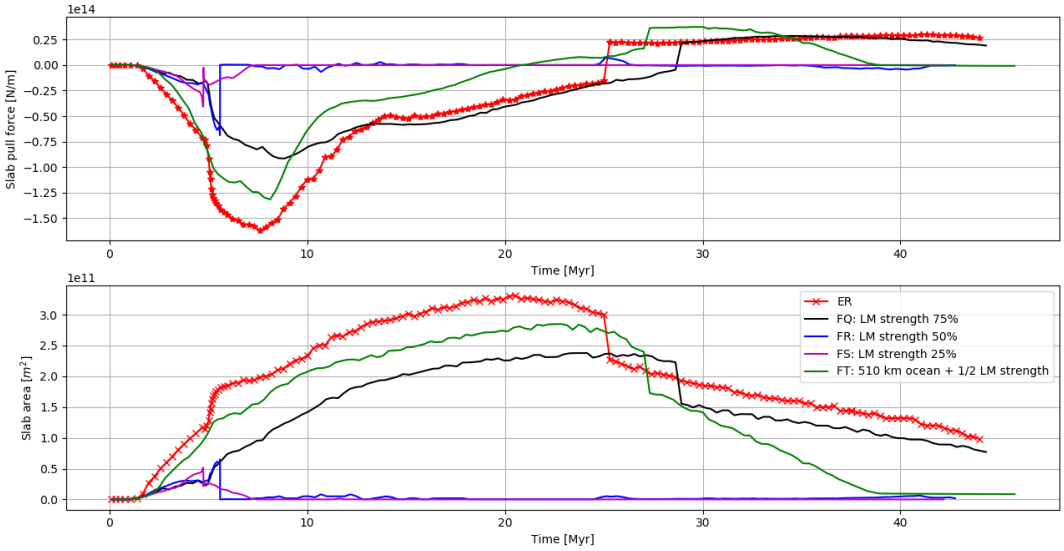

Figure 39: Evolution of the slab pull force for models FQ-FT and the reference model ER. The lithospheric mantle frictional strength has a large influence on the dynamics of the model.

From the slab pull evolution of models FQ-FT it is clear that the frictional strength of the lithospheric mantle significantly impacts the model dynamics. Decreasing frictional strength reduces the magnitude of driving forces especially in the first 10 Myr and changes the timing and depth of slab detachment. Strikingly, a 25% strength reduction results in a peak slab pull half as high as the reference model and 4 Myr later slab detachment (black line in Figure 39). Importantly, this model develops lower crustal indentation. Further reducing the strength results in early detachment (Figure 40), after which both forces are insufficient to sustain further convergence or rollback. In model FS (50% reduction), the slab detaches shortly after the push is released at a depth of 110 km. In the case of quartered frictional strength, detachment happens at the surface through the fast rifting as described earlier.

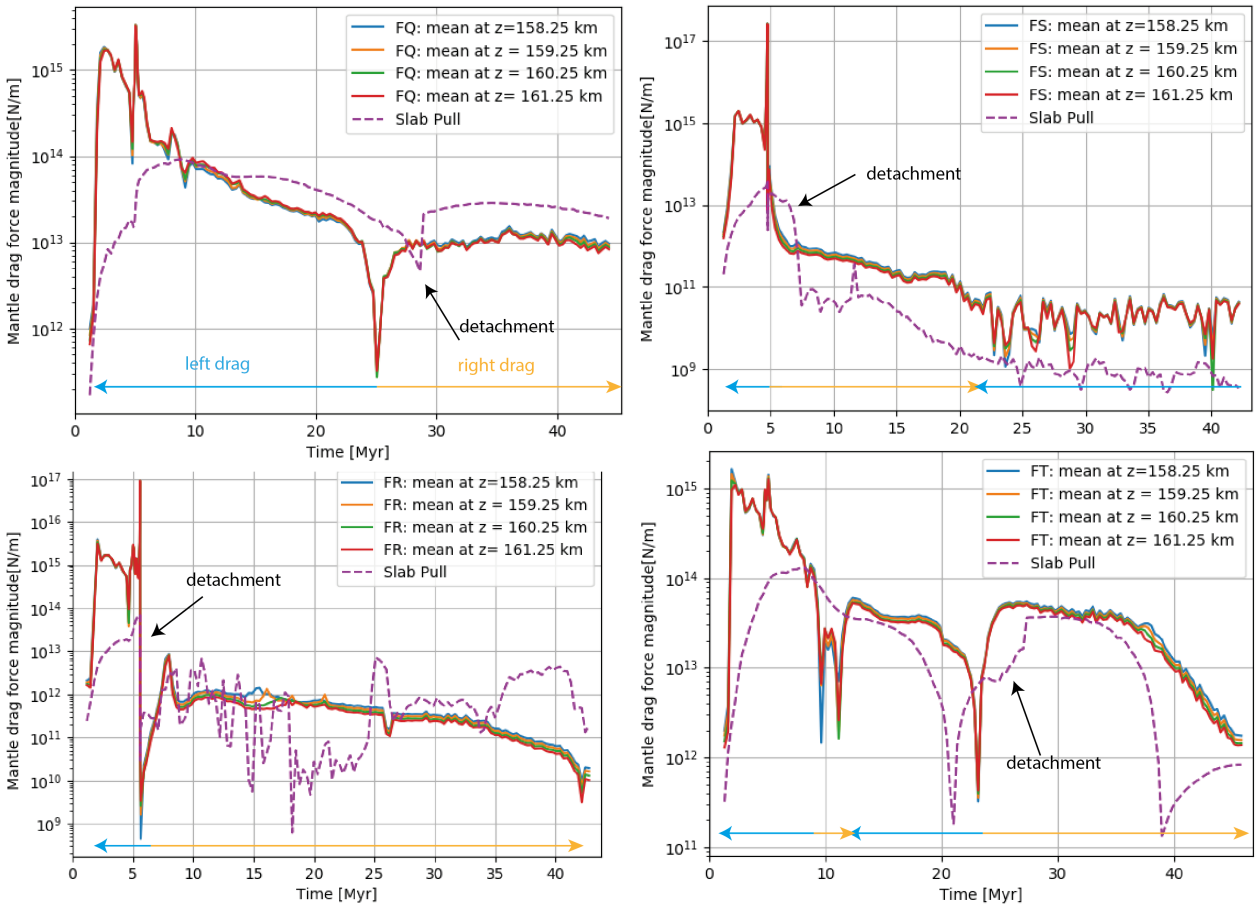

Figure 40: Mantle drag magnitudes for the lithospheric mantle friction parameter study. From left to right, top to bottom: FQ: $P_f/P_s = 0.75$, FR: $P_f/P_s = 0.50$, FS: $P_f/P_s = 0.75$ and special case FT: ocean length 510 km, $P_f/P_s = 0.50$. Dominant drag direction is indicated with blue (to the left) and yellow (to the right) arrows.

A 25% weaker lithospheric mantle (model FQ) decreases the viscosity (and hence the ductile/elastic strength) contrast between the overriding plate mantle lithosphere and the downgoing oceanic plate, increasing coupling across the plate interface, i.e. the interface becomes sticky. This reduces the amount of oceanic material that enters the mantle and results in a slightly flatter initial subduction. Together these observations explain the lower slab pull magnitude observed in Figure 39. The sticky plate interface also prevents the upper crust from subducting during the wedge emplacement on top of the left continental plate. As a result, lower crust makes up approximately 95% of the material in the subduction channel by $t = 8.5$ Myr. This lower crust decouples from the downgoing plate in the final stages of this model. The upper crust in the core of the orogen forces the sediments in the accretionary wedge to exhume along the retro-shear (Figure 41), decoupling the upper crust from the lower crust in the overriding plate. Simultaneously, the remaining lower crust of the overriding plate indents the core of the orogen.

Interestingly, when combined with a slightly shorter ocean of 510 km a 50% weaker lithospheric mantle does not lead to early and shallow detachment. Instead, the smaller negative buoyancy of the slab allows for a sign switch in slab pull at $t \approx 21$ Myr, 4.8 Myr prior to slab detachment (Figure 39), which slightly accelerates the rebound. Where 40 km of slab detachment-induced vertical rebound is observed in the reference model, 100 km of rebound is observed here (Figure 42). However, the overriding plate moves away from the trench by only 70 km. The other 30 km of vertical shortening is accommodated by upward movement of continental upper and lower crust. The pro-wedge uplifts and widens as a consequence (figure 43). At the very end of the simulation, the slab pull switches sign once more. This is caused by slow delamination and subsequent upward flow of the lower crust. The downward pull is not enough to generate slab rollback, as the larger mantle drag is still oriented to the right (Figure 40).

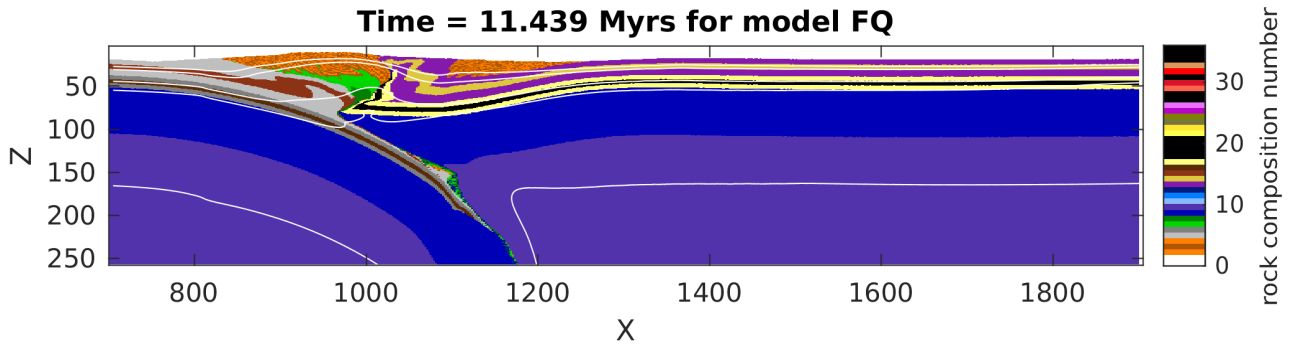

Figure 41: A 25% weaker lithospheric mantle leads to indentation of the orogen and (later) the subducting plate by the lower crust of the overriding plate. This is linked to large amounts of weak oceanic crust in the orogen that folds and breaks the tip of the lower crust.

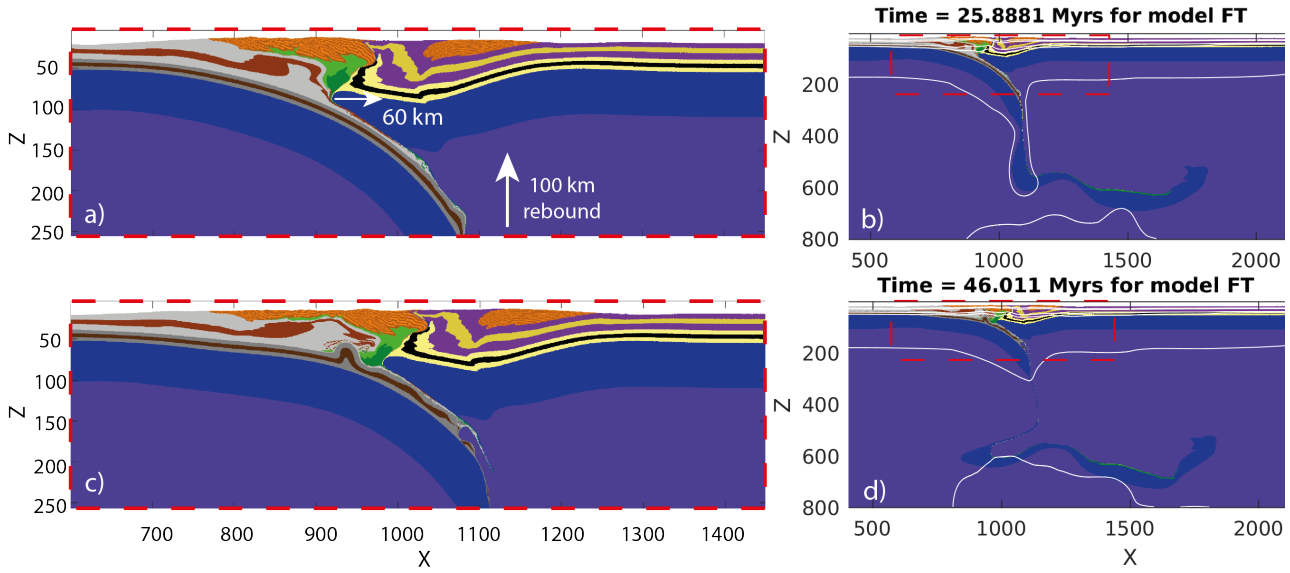

Figure 42: Model FT, which combines a 510 km ocean with a 50% weaker mantle, at the moment of slab detachment (a-b) and at the end of the simulation (c-d). Significant rebound of 100 km is observed, 2.5 times as much as the reference model. The lower crust slowly delaminates from the downgoing plate.

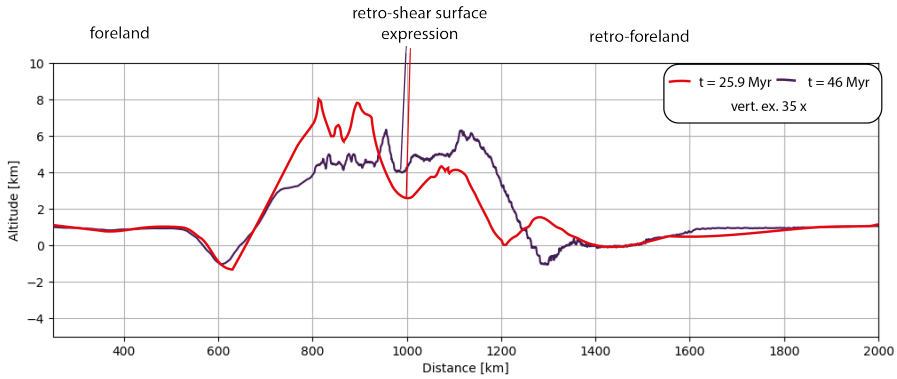

Figure 43: Illustration of the topographic response to slab detachment for model FT (510 km ocean, halved lithospheric mantle strength).

4.11 Peierls Creep

Peierls creep is a plastic stress-limiter active in the mantle lithosphere under slab conditions, i.e. HP/LT (Section 3). It is commonly included to promote slab detachment due to its weakening effect on the mantle lithosphere of slabs (e.g Duretz et al., 2011). It lowers the maximum effective viscosity, making the slab more susceptible to visco-plastic deformation and to slab bending. Peierls creep is therefore very likely to induce shallower and earlier slab detachment compared to the reference model, which does not include this mechanism. Indeed, including Peierls creep leads to 18 Myr earlier and 220 km shallower slab detachment with respect to the reference model (Figure 47). This is apparently too shallow to retain a large enough slab pull or drag to maintain convergence (Figures 44 and 45). Instead, the remaining slab educts and the overriding plate moves away from the trench. Buoyant upper continental crust decouples from the downgoing lower crust and rises to the core of the orogen (Movie S4. The model reaches steady state shortly after this event.

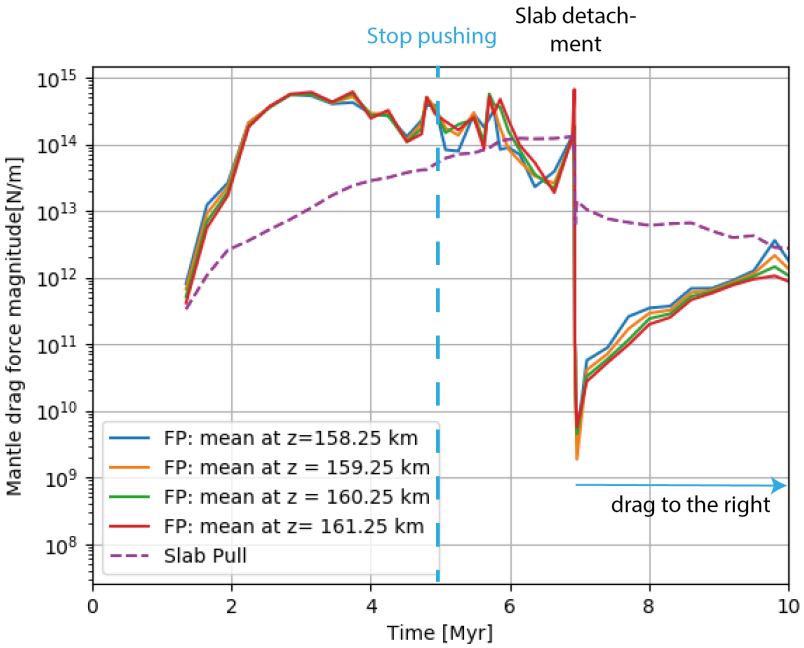

Figure 44: Mantle drag and slab pull magnitude during the first 10 Myr of the model with Peierls creep. Compared with Figure 18, the response to kinematic release at 5 Myr is slow and gradual. No spike in drag force is observed. Slab detachment occurs at the ocean-continent transition at 6.9 Myr. Thereafter, slow eduction occurs as the upper plate is forced back.

Inspection of viscosity, stress and strain rate reveals that the weakening of the slab by the Peierls creep is visible already during the beginning stage of subduction (Figure 46b and e compared to panels a and c). The weaker slab implies a more coupled subduction interface due to the reduced viscosity contrast across it, leading to a more gradual build-up of slab pull (Figure 45) and somewhat slower subduction. Another effect is seen in the slab dip: these amount to 27° and 22° at 3.0 Myr for models ER and FP, respectively. Moreover, where the release of the push is sharply depicted in the slab pull in the reference model (Figure 18), the response is much gentler with Peierls creep: the wedge is thrust over the left continent less rapidly. At the same time, the mantle drag is only slightly larger than the slab pull (Figure 44). The effective viscosity of the slab has been 2 orders of magnitude weaker compared to that of the reference model since t = 3 Myr, which decreases its elastic strength. This causes the slab to bend more easily (Figure 46e-h). Therefore, the slab with Peierls creep has a sharper kink at 5 Myr. The smaller drag is a consequence of this. Together, these observations explain the slower overthrusting. The weak slab is prone to detach at the transition to continental lithosphere, where Peierls creep is inactive. At 5.92 Mr, shearing starts here. Nearly exactly one million year later, the slab detaches (Figure 47).

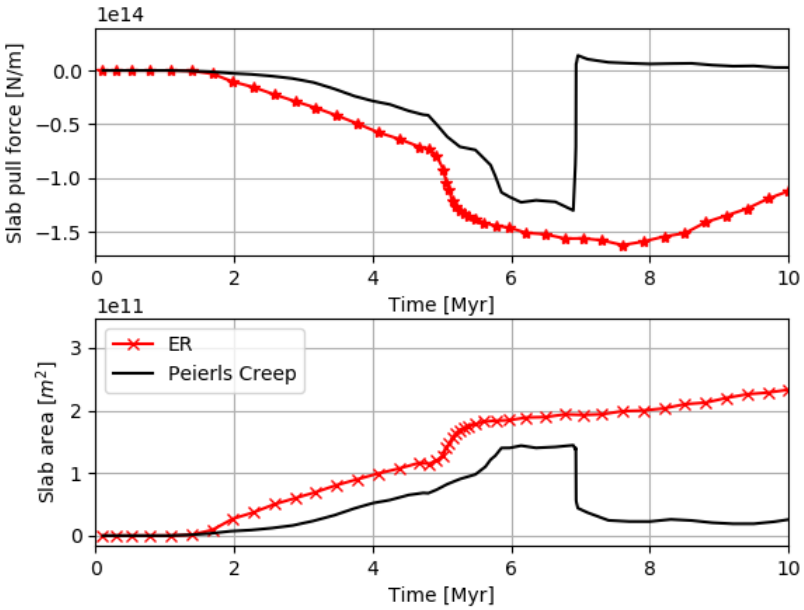

Figure 45: First 10 Myr evolution of the slab pull force and orientation for model FP and ER. Peierls creep results in flatter subduction due to a more coupled subduction interface. This means that slab area and pull grow more slowly. The push stop is less visible at 5 Myr due to delayed and slower overthrusting of the accretionary wedge. After detachment, the remaining continental slab slowly educts.

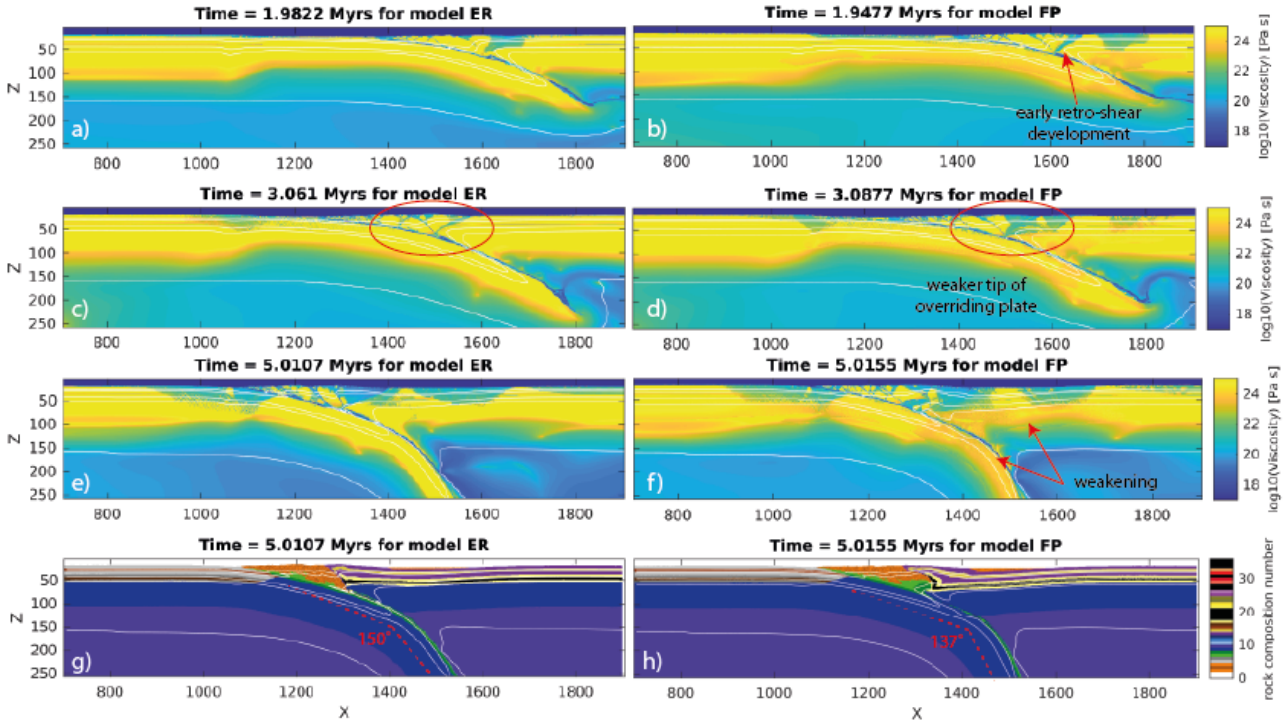

Figure 46: Viscosity plots of the reference model and model FP at three moments during the kinematic stage. The slab and overriding plate both are progressively weaker in model FP compared to the reference model ER. The weaker slab also allows for stronger slab bending (panels **g**-**h**).

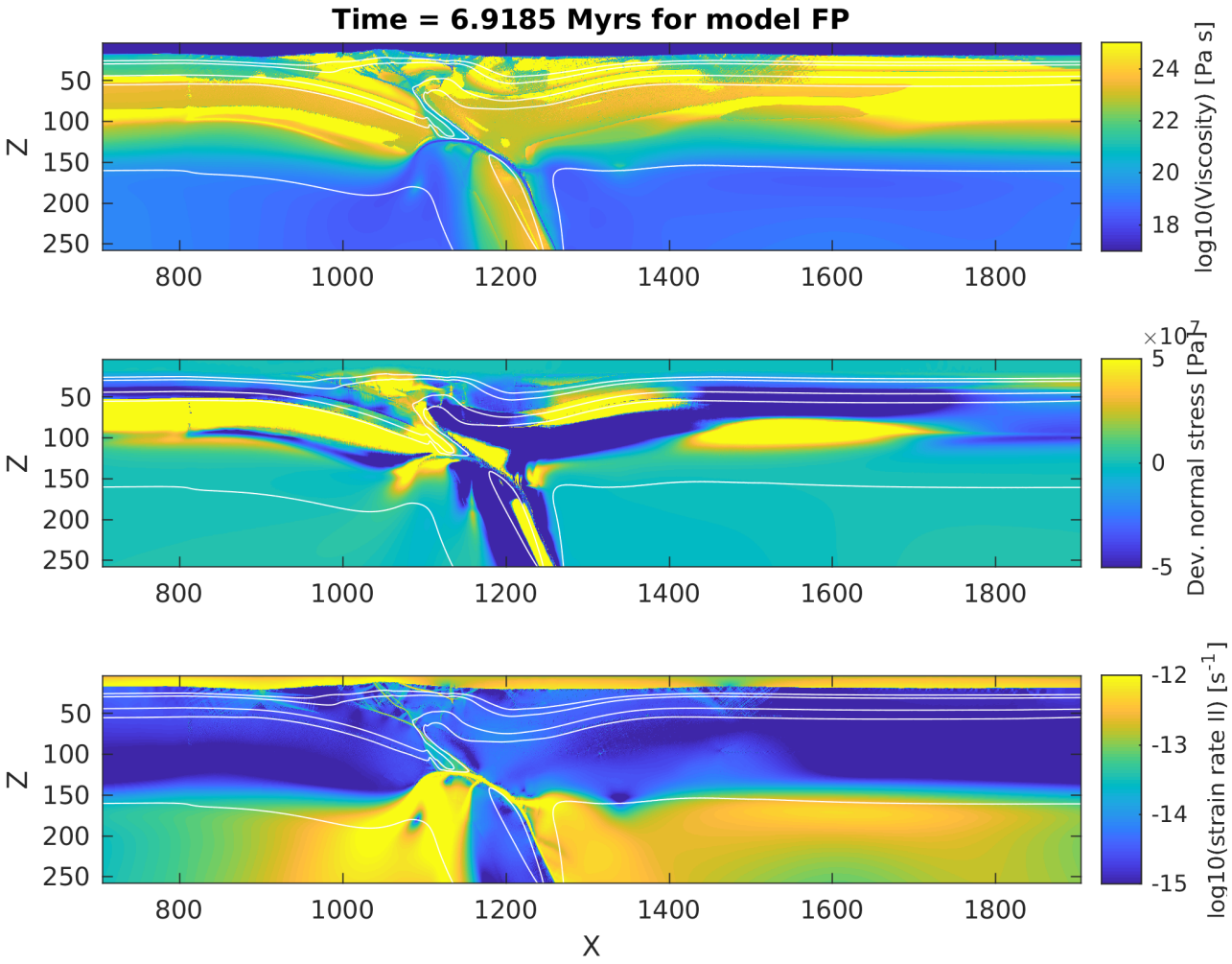

Figure 47: Model FP during slab detachment. Following 1 Myr of weakening, the slab rapidly shears off at z = 130 km, i.e. 110 km below the initial crust-air interface.

This significantly weaker collisional system inevitably affects other aspects of the model evolution. For example, a retro-shear can form already during the kinematic convergence stage (Figure 46b), as the overriding plate is weakened by the increased coupling across the subduction interface. Therefore, a deep and asymmetric retro-foreland basin is already present when the push is released. Furthermore, much more oceanic crust is scraped off during oceanic subduction than in the reference model (Figure 46g-h). The exhumation of this oceanic material is likely what causes retro-shear formation in this case.

5 Discussion

5.1 The role of the lower crust

The lower crusts of the down-going and overriding plates were shown to play an important role in continental collision. In the down-going plate the lower crust can essentially either subduct with (e.g. Figure 10) or delaminate from the mantle lithosphere (e.g. Figure 35c). The modelling results indicate that plagioclase and mafic granulite rheologies both lead to subduction of the lower crust to great depths (300-400 km), which usually only starts to delaminate from the lithospheric mantle in the final stages of the models. The difference is the degree of coupling between the upper and lower crust, as witnessed by the earlier upper crustal delamination in cases of mafic granulite lower crust. The higher degree of coupling in plagioclase models (FB) results in deep subduction of buoyant upper crust (Figure 31c). The later delamination then relieves a large positive component from the slab pull, causing a unique dynamic signature where the slab pull increases again (Figure 30). A wet quartzite lower crust in the lower plate implies a very low resistance to the overriding plate that accelerates after the push is released. This strength contrast results in indentation of the down-going crust by the lithospheric mantle. The subsequent near-closure of the subduction channel halts subduction, strongly promoting complete crustal delamination as well as early and shallow slab detachment (Figure 32). In reality, the lower crustal composition is highly variable, but commonly mafic (e.g. Rudnick and Taylor, 1987). The wet quartzite composition may therefore not be very realistic.

The lower crust of the overriding plate determines to a large extent whether a single- or double-vergent orogen forms. A weak lower crust and/or situations when the tip of the overriding plate is bent up promote the development of a single-vergent orogen. In case of a weak lower crust, shortening is accommodated by pure-shear thickening of the overriding crust, while with a bent overriding crust the subduction channel is funnel-shaped, directing transport of crustal material and sediments downward. The importance of initial behaviour of the tip of the overriding plate is not mentioned in other studies (e.g. Vogt et al., 2017, 2018; Dal Zilio et al., 2020; Faccenda et al., 2008, 2009). The single-vergent orogens record less trench retreat than the double-vergent orogens, as deformation is taken up by the weak crust of the overriding plate. The extreme similarities between mafic granulite and plagioclase lower crust in the overriding plate imply no significant difference in collision dynamics between intermediate and strong lower crust cases.

Furthermore, some interesting interactions have been observed between layers of the overriding plate. In most cases, the upper crust remains attached to the lower crust, despite the weak wet quartzite rheology of the upper crust that was constant for all models. However, in models with an ocean length of 510 km the overriding upper crust decouples from the lower crust allowing the lower crust to indent the orogen and downgoing plate. In previous studies, a relatively strong lower crust was also found to promote horizontal indentation (Gerbault and Willingshofer, 2004). However, lower crustal indentation is only observed in a few models despite the mafic granulite rheology. Therefore, different factors must influence the indentation process. The results of this study suggest that the strength of the lithospheric mantle plays a role in this, as the largest amount of indentation is observed in model FQ (25% weaker lithospheric mantle). The mantle lithosphere exerts pressure on the subduction interface. This coupling across the subduction interface increases as the mantle lithosphere strength decreases. When it has forced the upper crust to delaminate from the down-going plate and exhume along the subduction channel, a strong lower crust facilitates exhumation along the retro-shear as long as there is no oceanic crust in front of the rising upper crust. If there is, the upper crust will exhume vertically because the oceanic material is too heavy to push away.

These results are consistent with findings of some previous studies that investigated the role of the lower crust. For instance, the occurrence of subduction of lower crust and decoupling of the upper crust from the downgoing plate in situations in cases with Moho temperatures $< 450°C$ is commonly observed (Toussaint

et al., 2004; Vogt et al., 2018). In fact, this stable-type continental subduction (e.g. Figure 10 was found to require low Moho temperatures < 450°C (Toussaint et al., 2004). However, the results of the present study differ significantly from those of Faccenda et al. (2008). For instance, a mafic granulite lower crust in combination with 10 cm/yr convergence rate (during the first 10 Myr) results in plate decoupling (Faccenda et al., 2008) while the plates remain coupled in this study (Figure 10). There are numerous possible reasons for this, such as an older and longer slab (the slab age is not mentioned (Faccenda et al., 2008)), the higher radiogenic heating of sediments in combination with a high (0.9) pore fluid pressure ratio of sediments, which all contribute to weakening of the orogen and the subduction interface. Despite these differences, lower crustal subduction is observed in both cases. A common feature in the models in Faccenda et al. (2008) is the upward tilted ("upwarped") position of the tip of the overriding plate including the lithospheric mantle (e.g. their Figure 3) which is most likely a consequence of the position of the initial accretionary wedge. Accretion of sediments pushes the tip of the overriding plate up. Indeed, such a tilted overriding plate tip is much more rare in this study (e.g. Figure 31b) and Figure 26). Here it seems to be a consequence of basal accretion of oceanic and sedimentary material in the initial stages of the acrretionary wedge. In many cases the tip of the overriding plate is tilted downward instead of upward, promoting formation of a deep, asymmetric retro-foreland basin by burial of the lower crust during wedge emplacement, which promotes development of a retro-shear (e.g. Figure 35c or 42a).

5.2 Threshold strength ratios?

Sediments / upper crust
Analysis of the models with varying frictional strength ratio between sediments and upper continental crust revealed a relatively sharp transition in model behaviour around the threshold value of approximately 1.0. Models with a ratio smaller than this number are likely to develop a single-vergent orogen characterised by localised deformation inside the pro-wedge, while upper plate deformation is limited (Figures 28c-f). This is interpreted to be a consequence of the enhanced upper plate buttressing capability, since the sediments are weaker than the continental crust.

When the sediments to upper crustal strength ratio slightly exceeds 1, a highly double-vergent orogenic wedge develops, with a prominent, narrow retro-shear. The width of the retro-shear increases when the strength ratio is much larger than 1, i.e. in the reference model. Instead, deformation in the overriding plate upper crust is distributed in a pure-shear thickening sense (compare Figures 10c-e and 28c-f). In this case, shortening is accommodated in the overriding plate. Since development of a retro-shear is required for the formation of a double-vergent orogen, this threshold gives important information about interactions between the accretionary wedge and the overriding plate in orogens.

Comparing this result with the work of Vogt et al. (2018) is somewhat difficult due to differences in model setup, such as the lack of an oceanic plate between the continents. This means that the accretionary wedge is composed of continental crust instead of sediments. Due to the lack of sediments in between the continents the frictional strength ratio between the left and right upper crust may be used instead of the sediments/UC ratio. This amounts to 1 in their reference model, which develops a double-vergent orogen (Vogt et al., 2018). Interestingly, the "strong overriding plate" models B1 and B2, with a left UC/right UC strength ratio of 0.75 indeed develop single-vergent orogens where the overriding plate is relatively undeformed (Vogt et al., 2018). Despite differences in model setup the result of lateral strength contrast of two colliding units thus seems to hold.
Upper crust / lithospheric mantle
The sediments/upper crust and lithospheric mantle strength parameter studies hinted at the existence of another threshold strength ratio, between the upper crust and lithospheric mantle. Its value appears to lie around 0.3. However, the mechanisms behind this threshold are less obvious than for the sediments/upper crust ratio. For instance, models FR (50% weaker mantle) and FF (twice as strong upper crust) both have a upper crust/lithospheric mantle strength ratio of 0.2, but the slab detaches early and at shallow depth in the model with a weakened mantle lithosphere. This seems surprising at first, but both the nominator and denominator of the ratio are twice as high as in the strong crust model as in the weak lithospheric mantle model. The sediments and lower crust are therefore relatively strong compared to the mantle lithosphere in model FR. Hence, the shallow and early detachment in model FR at the ocean-continent transition is likely caused by insufficient resistance of

the downgoing plate to the wedge emplacement and positive buoyancy of subducting continental crust. This interpretation is further supported by the detachment at the surface observed in model FS (i.e. 75% weaker lithospheric mantle). In this case, the lithospheric mantle of the overriding plate is completely coupled to the quickly steepening oceanic slab, rotating the slab clockwise. These processes severely weaken the frontal part of the accretionary wedge (Figure 48), paving the way for detachment near the surface through symmetric rifting.

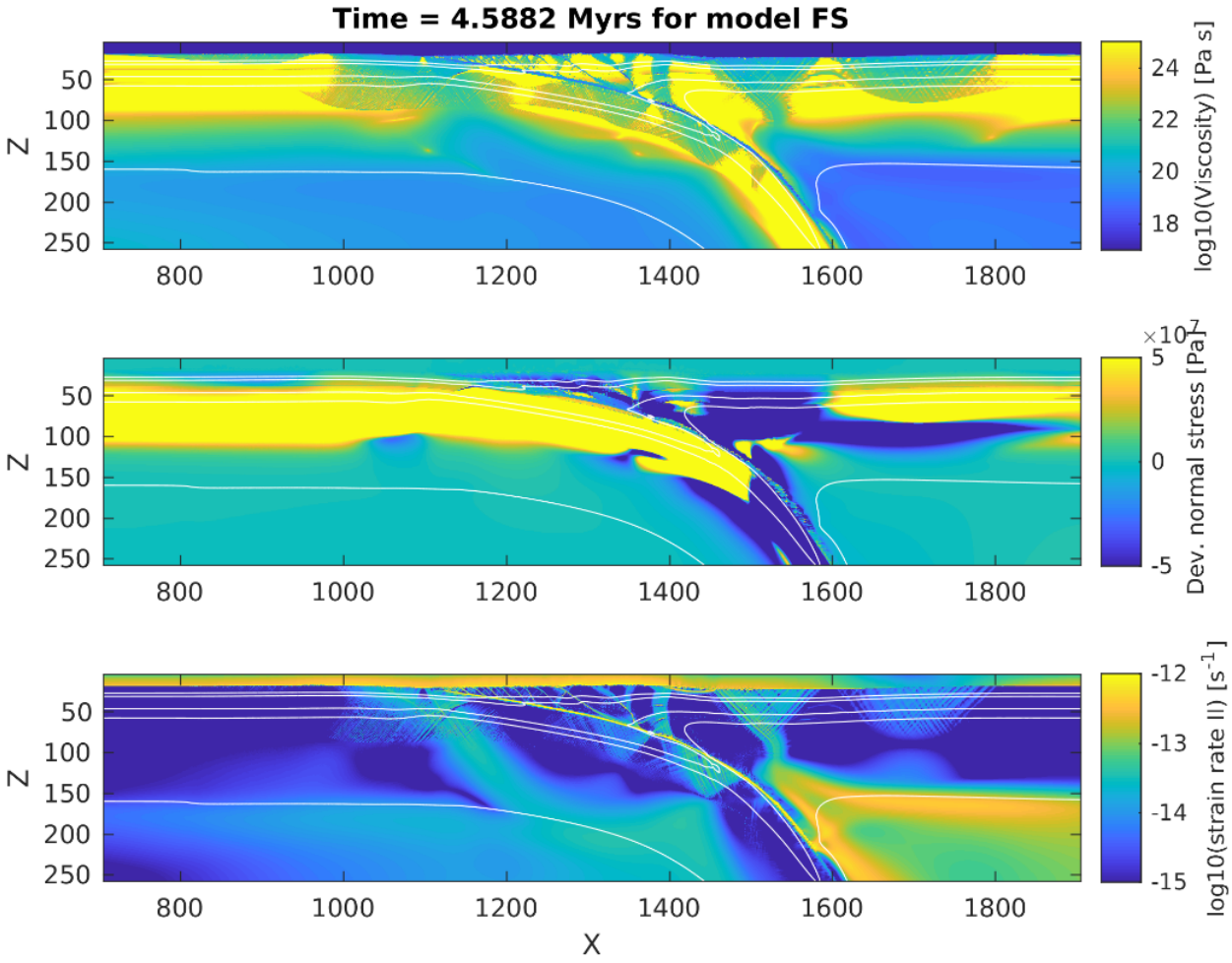

Figure 48: Viscosity, normal stresses and strain rate plots of model FS (75% weaker lithospheric mantle) at the onset of slab steepening during the kinematic stage. The slab drags the highly coupled lithospheric mantle down, causing serious weakening (4 orders of magnitude) of the lithosphere beneath the frontal part of the accretionary wedge. The slab detaches 140 kyr later through symmetric rifting at the weakened location.

In model FQ, the upper crust of the overriding plate decouples from its corresponding lower crust, and proceeds to indent the orogen and down-going plate (Figure 41). This decoupled behaviour is otherwise only seen in model FI (510 km ocean). Therefore, it is important to understand why this occurs. First of all, more oceanic material is scraped off during subduction. When the push is released, the overriding plate advances toward the down-going plate. In model ER, this happens horizontally. However, due to the abundance of oceanic material in the core of the wedge the tip of the overriding plate lower crust and lithospheric mantle is forced upward. During further convergence, the tip of the lower crust is folded until the relatively strong wedge slowly separates this segment of lower crust and the upper crust from the remaining lower crust (Figure 41).

The threshold value likely is not constant, suggested by the reference-like results of model FT (Section 4.3). There, the weak lithospheric mantle does not lead to early or shallow slab detachment. This is probably caused by the combination of a smaller peak mantle drag (Figure 40c-d) and the fact that the wedge emplacement occurs during the kinematic stage. Regardless, some general patterns can be identified concerning the influence of the UC/LM strength ratio. Models with a relatively strong lithospheric mantle show compression of the subduction channel by the mantle lithosphere. On the other hand, weaker mantle lithospheres display either indentation of the down-going plate by the lower crust (model FQ) or the lithospheric mantle (models FF, FT).

The transition from mantle lithosphere subduction to indentation tectonic style is consistent with the findings of Ellis (1996), who provided a simple but useful analysis of forces in continental collision. Furthermore, the lithospheric mantle plays a role in maintaining the integrity of plates during continental collision. It should be kept in mind that the lithospheric mantle should be stronger than the crust and sediments.

5.3 Detachment at the surface

The parameter studies exposed a somewhat troubling issue in the current model setup: detachment at the surface caused by lithospheric extension. This is not the same as shallow detachment described in other studies (e.g. Duretz et al., 2011, 2012), because the mode of detachment is different. The surface detachment occurs through extremely fast rifting (asymmetric or symmetric), while the shallow detachment is facilitated by plastic shearing. Instead, the surface detachment appears to reflect extreme tension around the left passive margin, sharply reducing the local effective viscosities. Deformation becomes completely viscous, explaining why the plate loses its integrity. Before the current reference model ER was established, this surface detachment was a much more prevailing issue. The reference model at that time had a Moho temperature of 500°C and a thinner lithosphere (120 km i.s.o. 140 km), amongst other minor differences.

In the models described in this work, surface detachment is observed in models EX, ET, and FS. Models EX and FS have in common that large parts or the entire lithosphere were much weaker than in the reference model. Model ET (slab age 100 Ma) has a stronger oceanic slab, as well as an increased slab pull due to the older slab. The fixed lower plate condition seems to promote this cross-lithosphere failure in all these cases by effectively forcing lower plate extension to be accommodated intra-plate. The effect of removing the fixed lower plate condition was briefly tested in an early stage of this research. These showed that when the lower plate is not fixed, the kinematic release induces highly accelerated subduction in one-sided convergence models. This occurred at non-realistic velocities, leading to complete crustal subduction and asthenosphere windows in many models.

Another factor in this process is a weakness in the initial temperature distribution of the left passive margin. At the start of the model run, there is a temperature contrast of about 80-100°C between the tip of the passive margin and the rest of the continent. While this difference has always largely equilibrated within 3-4 Myr (Figure 49), it may contribute to the weakening of the passive margin leading to surface detachment, because the difference is larger with higher Moho temperatures. The problem does not occur in the right passive margin, because it is twice as long. Attempts to solve the issue were unsuccessful. Since the viscosity and stress/strain rate figures do not show a visible weak spot either, it was assumed that the issue is not that important.

In summary, the parameter space under which realistic results are produced is sensitive to initial conditions, as was already suggested above. This applies to the surface detachment as well. However, in most cases the detachment can be easily explained.

5.4 Comparison with the Central Alps

To interpret the results in context of the Central Alps, similar zoomed composition and non-elastic strain rates are shown for the three best candidates in Figure 50. When compared to the geological cross-sections through the Central Alps (Figures 2 and 3), all three have features in common with the Central Alps, such as an intermediate (200 km) depth of slab detachment and exhumation of crustal material along a retro-shear. In addition, these models display lower crustal subduction (therefore a deep Moho) as well as buoyant return flow of upper crust along the subduction interface. The orogens are also highly double-vergent.

Out of these three models, it can be argued that model FI best produces an orogenic architecture in the style of the Central Alps. In the first place, the lower crust of the overriding plate is too rigid in models ER and FQ. In addition, the decoupling between the upper and lower crust occurs mostly in the down-going plate in the reference model. This is likely what prevented the lower crust from indenting the orogen further. On the other hand, both continents display a clear mid-crustal décollement in models FI and FQ (Figure 50). However, in model FI the retro-shear can be traced better from the surface down to the tip of lower crust indenting the down-going plate. The retro-foreland of the Alps is under compression (Dal Zilio et al., 2020). After careful analysis of deviatoric stress plots of these three models, model FI shows most compression in that area. This compression is caused by the exhuming upper and lower crust, which induces vertical shortening that is taken

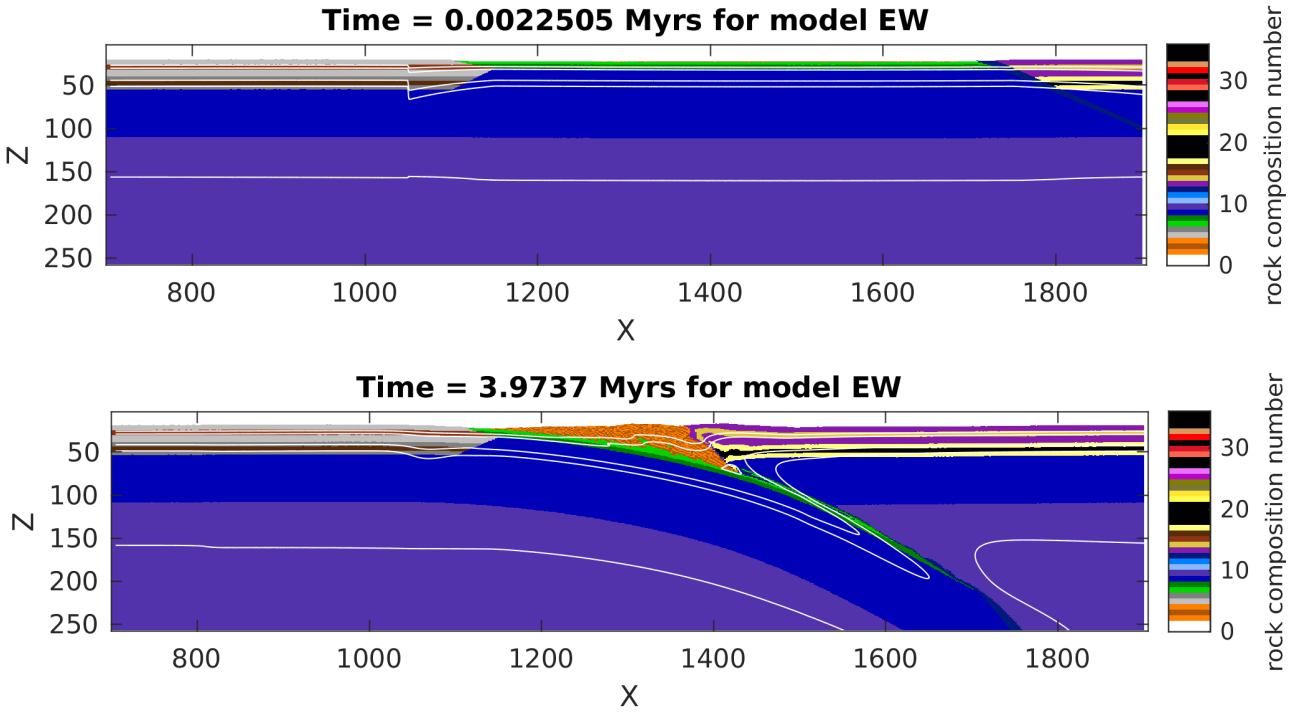

Figure 49: Visualisation of the sharp transition in temperature (white lines) from continent to passive margin on model EW. The second panel shows that it equilibrates within a few Myr.

up by orogenic extension to both sides. Finally, the negative slab pull observed in the final stage of model FI would very likely grow further if run for longer, potentially leading to slab rollback.

Despite the good fit to nature in terms of orogenic architecture, some differences between models and nature should be noted. For instance, the post-detachment slab rollback argued for by Dal Zilio et al. (2020) is not observed in any of the models investigated here. Since Adria is still advancing at a slow rate toward Europe (1-2 mm/yr, Handy et al., 2010), the overriding plate should advance during the final stages of the models as well. There may be several explanations for this discrepancy between model and nature. For instance, transmission of slab pull in the direction perpendicular to the trench to areas where slab detachment has not yet occurred could lead to convergence after detachment (Duretz and Gerya, 2013). Those authors also put forward mantle drag as a possible driving force for post-detachment convergence, after earlier studies indicated the significance of this force (Alvarez, 2010). However, they did not quantify it, neither was it quantified in other studies researching the Central Alps (Vogt et al., 2018; Dal Zilio et al., 2020). The dynamic analyses performed in this research confirm that mantle drag below the overriding plate is as significant as slab pull, but it does not induce late-stage convergence (yet).

Furthermore, in models FI and FQ a slight discrepancy of surface topography exists between the models and the Central Alps. The maximum elevation in the Central Alps is $\approx$ 4 km (Dal Zilio et al., 2020). This is exceptionally well reproduced in the final stage of the reference model (Figure 15), but models FI and FQ show slightly higher maximum topographies of about 6-6.5 km. This is addressed in the model limitations below. Widening of the orogen following slab rebound is not observed (yet) in models FI and FQ. In model FI this is a consequence of the downward slab pull being larger than the rightward mantle drag (Figures 36 and 37), while in model FQ the slab rebound is very small in the first place.

Additionally, the choice for an initial Moho temperature of 450°C requires some attention. Deformation inside the orogen in the models discussed here is mainly ductile, indicated by the distributed strain rate pattern in Figure 50. Seismic events were found to occur mostly in the orogenic wedge top and the subduction interface (Figures 19 and 21). In the Central Alps earthquakes occur throughout the orogen, foreland and retro-foreland (Singer et al., 2014). On the other hand, thermorheological models of the NFP-20 East cross-section suggest a brittle-ductile tansition located at 15-20 km depth (Vigano and Martin, 2007). Those results indicate Moho temperatures of 500°C (in the foreland areas) to 800°C (directly below the orogen), arguing for a ductile lower crust. In the present study only the lower plate lower crust is ductile. This paradox of lower crustal earthquake

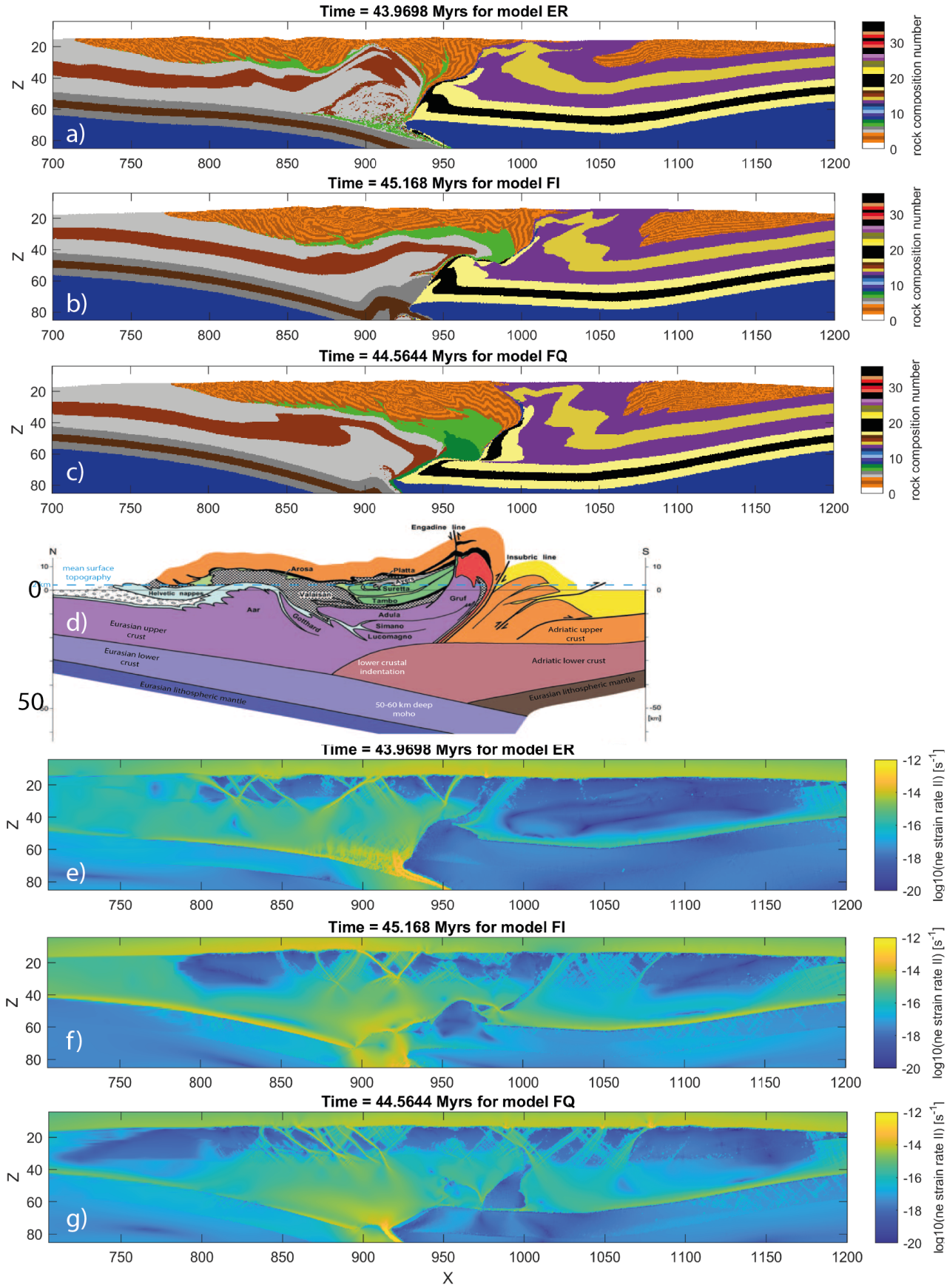

Figure 50: Comparison of the three most Alps-like models in terms of composition (**a-c**) and non-elastic strain rate (**e-g**) . All three bear characteristics of the Central Alps crossection (**d**) which is a miniature version of Figure 2). Model FI best resembles the Central Alps.

observations while at the same time deformation is ductile was addressed by Watts and Burov (2003), who concluded that this type of seismicity is not indicative of lithospheric strength. The fact that models presented here produce similar deformation patterns may imply that initial Moho temperatures were on the order of 450°C.

Overall, the modelling results are consistent with natural observations and the results of modelling studies concerning the Central Alps. An ocean plate length of 510 km gives the best results, and is within bounds of estimates of subducted oceanic material (Handy et al., 2010; Van Hinsbergen et al., 2020). The oceanic plate is necessary, as it better resembles the Central Alps tectonic history. Additionally, the deformation in the upper plate caused by exhumation of deep crustal material and lower crustal indentation is consistent with a recent 3D modelling study (Liao et al., 2018) as well as 2D numerical modelling studies (Liao and Gerya, 2017). In the study of Dal Zilio et al. (2020), it is unclear why the slab rolls back after detachment, while very similar rheological parameters and model setup were used. Importantly, those models do not show a pronounced retro-shear, which is a key feature of the Central Alps. The post-detachment upward tilting of the Adriatic lower crust is also not reproduced. The exact cause of these considerable discrepancies remains elusive. The colder Moho temperature (350°C) might explain part of it, as this will make deformation less ductile.

Recently a different interpretation for the lower crustal structure beneath the Central Alps was made (Schlunegger and Kissling, 2015) where the lower crust of the downgoing plate forms a crustal root and lower crustal indentation by the overriding plate is less pronounced. Model B1 (weak downgoing plate, strong overriding plate, slow convergence) of Vogt et al. (2018) has a similar structure. However, deformation in the Central Alps has been approximately equally taken up by both the down-going and overriding plates (Rosenberg and Kissling, 2013). Therefore, if a lower crustal root is indeed present beneath the Central Alps it is likely not caused by a strong lateral strength contrast. Instead, it may be an expression of ongoing lower crustal delamination as in Figure 50b,f which occurs after lower crustal indentation.

5.5 SRO model evaluation

The slab rollback orogeny (SRO) model in its current definition has been argued to apply to the Central Alps (Schlunegger and Kissling, 2015; Kissling and Schlunegger, 2018; Dal Zilio et al., 2020). The modelling and dynamic analyses performed in this research allow for an evaluation of this model in a dynamic context. The most important characteristics of the Alps that inspired the application of the SRO model are the constant (fixed) position of the lower plate, rapid exhumation of upper crustal material into the core of the orogen and detachment of the oceanic plate initially present between the continents. The fixed lower plate condition is necessary to induce rollback subduction in the present study. If it is not fixed, rebound after detachment is more likely to be accommodated by eduction and less by uplift of the orogen. However, in the parameter space investigated here this boundary condition can lead to rifting of the left continent (see above).

According to Kissling and Schlunegger (2018), the primary driving forces in the SRO model are vertical. Dynamic analysis performed here shows that rollback or trench retreat happens when a positive (i.e. leftward) mantle drag exceeds a negative (downward) slab pull for a few Myr (e.g. Figure 18). The overriding plate retreats when a rightward drag is dominant over slab pull (negative or positive). While trench retreat is very common before detachment, a negative final slab pull is rare in the models. In addition, drag is almost always oriented to the right in the final stages, even in the 'best' model FI (Figure 37). In models with any significant slab rebound or unbending following detachment, the displaced asthenosphere material generates flows to the right. Since detachment induced rapid uplift of the Alps to their present topography (Kissling and Schlunegger, 2018), the Eurasian slab must have rebounded as well, and mantle drag was likely oriented to the south (i.e. away from the trench). However, plate tectonic reconstructions indicate constant slow convergence between 20-0 Ma (Handy et al., 2010; Van Hinsbergen et al., 2020). This discrepancy is addressed below.

The modelling results also show that slab pull often remains directed upward until the end of the simulation. Two exceptions to this are models with an ocean length of 510 km (FI and FT). This late pull is strongest in model FI, but there is still no rollback or trench retreat at the end, although the slab pull is growing due to slow delamination of lower crust from the down-going lithosphere. This may lead to rollback in even later stages of the collision. The fact that the slab below the Alps reaches shallower depth (i.e. 200 km) than in the best models implies that the slab pull is even smaller than in the models, making it unlikely that the slab pull drives post-detachment rollback by itself, unless the slab is uncommonly dense or the overriding plate is shorter, as the drag force scales with the length of the overriding plate (Duretz and Gerya, 2013).

Despite the lack of post-detachment rollback, the orogenic architecture is well reproduced by the models

presented in this thesis. A fixed lower plate, an initially 510 km long ocean, an upper crust that is about as strong as the wedge sediments and an intermediate to strong lower crust are key parameters that promote the development of a double-vergent orogen in the style of the Central Alps. These results suggest that the SRO model overestimates the magnitude of the slab pull in the final stages of collision and underestimates the role of mantle tractions below the overriding plate. Quantifying these two forces has proven to be an excellent first step in explaining the model kinematics. Thus, it is strongly suggested to incorporate these in the SRO model to make it physically more viable.

5.6 Model limitations

Although the modelling approach used in this study allows us to study complex processes involved in continental collision, there are several shortcomings that are discussed here. For instance, the 2D modelling approach was chosen to limit the computation time. Already the models took 3-4 weeks to reach 45 Myr. The lack of a third dimension has consequences for the partitioning of deformation inside the model, since the third dimension is horizontal, the vertical component of deformation is overestimated in 2D models (Gerbault and Willingshofer, 2004)). Another consequence is that orogen-perpendicular deformation such as strike-slip components and lateral extrusion (sensu Ratschbacher et al. (1991)) can not occur. Since the lower crustal indentation interpreted in the Central Alps is likely linked to 3D processes (Van Hinsbergen et al., 2020), the two-dimensional approach may explain why extensive lower crustal indentation is relatively rarely observed in the models. A third dimension also enables toroidal mantle flow. This horizontal flow around the slab is most important during rapid slab steepening and trench retreat (Schellart and Moresi, 2013). The steady trench positions observed in the present study imply that toroidal flow has by itself little influence on post-detachment convergence. However, slab movements in surrounding areas could have affected flow patterns in the Central Alps.

Another simplification is the uniform lithosphere thickness used in many of the models. The LAB temperature is reached at 140 km depth. In nature, the lithosphere thickness is defined by the depth to an isotherm of around 1600 K Turcotte and Schubert (2002). This depth depends on the time since the last heating event (thermo-tectonic age) for continents and slab age for oceans (Equation 24). However, continental lithospheres are usually thicker than the oceans (Turcotte and Schubert, 2002). The 140 km thickness used in this study can be seen as a compromise: it is relatively thin for continental lithosphere and relatively thick for oceanic lithosphere. With this thickness, the LAB temperature beneath the ocean is reached at the same depth as below the continents. In model ET (slab age 100 Ma) the LAB depth is overwritten by the thermal boundary condition at 160 km. This will likely have little effect on the modelling results, since the thermal gradient in oceanic lithosphere decreases with depth.

The instantaneous erosion/sedimentation implementation governed by prescribed topographic levels pose a possibly more significant approximation with respect to nature. This is simpler than for instance diffusion or transport equations based on erosion and sedimentation rates as used in a number of other studies (e.g. Vogt et al., 2017; Duretz and Gerya, 2013). Some test runs with their approach were attempted, but resulted in surface detachment as described above. Before the detachment, the accretionary wedge had much fewer sediments than previous models. Therefore, the instantaneous method applied here may overestimate the amount of sediments in the accretionary wedge. This was partly countered by lowering the sedimentation level from 20 km to the current 22 km in the models described in this study. Still, the amount of sediments is relatively large. This may lead to a wider orogen (Vogt et al., 2017). The relatively high erosion level used in this study (10 km) leads to lower amounts of exhumation along the retro-shear. Even so, many models display a modest to large extent of exhumation of lower plate material (Section 4.3).

In reality, the subduction of the Alpine Tethys included a thin and small continental margin: the Briançonnais continental sliver (Section 1). If this would be included in a model, it would introduce an extra component of positive buoyancy to the collisional system may have significant effects on the model evolution. For instance, it may slow down subduction earlier, change the timing and depth of slab break-off. However, this remains speculative until further research has been undertaken.

5.7 Future work

Future research should further develop and confirm these initial findings. For instance, quantification of the strength of the plate interface would be useful, as analogue models have emphasised its relevance for e.g. the

formation of a retro-foreland basin (Willingshofer and Sokoutis, 2009). This could improve the connection of processes in the slab to behaviour inside the orogen and overriding plate. In addition, evolution of the topographic load at the surface and at the crust-mantle interface could be very useful to further quantify the SRO model. As indicated above, it would also be very interesting to document the effects of including a continental sliver in the oceanic plate in this Central Alpine setting on the model dynamics. The parameter study of initial ocean length should be repeated with accordingly adjusted durations of prescribed convergence to better isolate the effect of this parameter on model dynamics.

Furthermore, the stress-limiting mechanism of Peierls creep has been proven to strongly influence the depth of slab detachment, leading to shallow detachment (Duretz et al., 2012). It would be interesting to test the effect of including this mechanism on more than only the reference model. Instead of varying parameters between model runs, it is also important to verify the robustness of the modelling results by rerunning some models with identical parameters, since Model EW produced different results after being restarted abruptly by a cluster reboot. It is still unclear why the second run was different from the first, i.e. whether a human or numerical mistake was made.

In addition to the above, more short-term models could be run to help verify the modelling results against earthquake observations in the Central Alps. The STM runs require setting of many different parameters, such as the x positions in between which events are registered and the threshold velocity above which marker data are saved. Careful experimentation with these parameters could produce a more complete picture of seismicity in the models. Moreover, a better sedimentation and erosion implementation should be tested further, with different erosion and sedimentation rates.

Finally, the model setup requires a minimum horizontal and vertical grid resolution of 500 m to accurately resolve the interfaces between different layers in the models. Recently, a promising step has been made in removing the grid dependency of modelling results by introducing a visco-elasto-viscoplastic rheology (Duretz et al., 2019). Including this in future models will certainly improve the reliability of any model outcomes.

6 Conclusions

For the first time, the buoyancy force slab pull and horizontal drag below the overriding plate have been monitored in 2D numerical models of continental collision. This was done to improve understanding and test the viability of the slab rollback orogeny model, which has been proposed for the Central European Alps (Kissling and Schlunegger, 2018; Schlunegger and Kissling, 2015; Dal Zilio et al., 2020). Analysis of these forces indicates that post-detachment rollback requires a trenchward drag in combination with a significant downward slab pull force. While this combination prevails before the slab detaches, it is not observed in any of the analysed models after slab detachment. Instead, slab unbending following detachment induces persistent mantle drag away from the trench, accompanied by 10-100 km of vertical shortening. This is taken up by extension in the orogen and slow movement away from the trench of the overriding plate. The findings of this thesis thus emphasise that vertical forces do not necessarily dominate in late stages of continental collision, contrasting with the postulate of the SRO model. In addition, horizontal forces dominate during wedge emplacement on top of the down-going plate. Despite the lack of post-detachment slab rollback, a number of models produce orogens and slabs with important characteristics in common with the Central Alps. Among many parameters investigated an intermediate ocean length (510 km), weak upper crust and intermediate to strong lower crust gave the most promising results.

The idea for this thesis started with the striking lower crustal indentation interpreted beneath the Central Alps, asking for an assessment of the relative roles of the lower crust of the overriding and down-going plates. While the lower crust of the down-going plate plays a relatively passive role by remaining coupled to the lithospheric mantle, the lower crust of the overriding plate was found to be much more important. It can indent the orogen if the lithospheric mantle below is somewhat weak and the upper crust is decoupled from the lower crust. More often the upper and lower crust stay coupled in spite of their strength contrast. Importantly, the overriding plate lower crust determines for a large part whether a single- or double-vergent orogen develops by tilting up (single-vergent), down (double-vergent) or staying horizontal. Finally, the results of this thesis hint at the importance of effective friction ratios between the sediments and the upper crust, as well as sediments and lithospheric mantle, as strong sediments promote retro-shear growth and indentation of the orogen and

down-going plate by the lithospheric mantle and/or lower crust.

Acknowledgements
First and foremost, this research would not have been possible without the help of dr. Ylona van Dinther (Utrecht University). The personal yet scientific tone during the regular meetings was invaluable for coping with the pandemic situation while writing a MSc thesis. Her great mix of compliments and suggestions for improvement made for very fruitful, motivated working conditions. My second supervisors dr. Ernst Willingshofer and prof. dr. Liviu Matenco (both Utrecht University) were a perfect fit for this research with their vast knowledge about both models of contintental collision and the natural prototypes they try to simulate. I thank them for their advice on connecting the modelling work to the geological observations and other studies, as well as their invaluable comments during discussions of my draft results. I am also very grateful to István Bozsó for his amazing will to help me solve difficult problems with my models. Finally, I want to express my gratitude to prof. dr. Taras Gerya (ETH Zürich) for his time to discuss ideas to research at the very beginning of my thesis.

References

Alvarez, W. (2010). Protracted continental collisions argue for continental plates driven by basal traction. *Earth and Planetary Science Letters*, 296(3-4):434–442.

Andrews, E. R. and Billen, M. I. (2009). Rheologic controls on the dynamics of slab detachment. *Tectonophysics*, 464(1-4):60–69.

Argand, E. (1916). *Sur l'arc des Alpes occidentales*. G. Bridel.

Auzemery, A., Willingshofer, E., Yamato, P., Duretz, T., and Sokoutis, D. (2020). Strain localization mechanisms for subduction initiation at passive margins. *Global and Planetary Change*, page 103323.

Baumann, C., Gerya, T. V., and Connolly, J. A. (2010). Numerical modelling of spontaneous slab breakoff dynamics during continental collision. *Geological Society, London, Special Publications*, 332(1):99–114.

Beaumont, C., Fullsack, P., and Hamilton, J. (1994). Styles of crustal deformation in compressional orogens caused by subduction of the underlying lithosphere. *Tectonophysics*, 232(1-4):119–132.

Beaussier, S. J., Gerya, T. V., and Burg, J.-P. (2019). Near-ridge initiation of intraoceanic subduction: Effects of inheritance in 3d numerical models of the wilson cycle. *Tectonophysics*, 763:1–13.

Bird, P. (1979). Continental delamination and the colorado plateau. *Journal of Geophysical Research: Solid Earth*, 84(B13):7561–7571.

Blaser, L., Krüger, F., Ohrnberger, M., and Scherbaum, F. (2010). Scaling relations of earthquake source parameter estimates with special focus on subduction environment. *Bulletin of the Seismological Society of America*, 100(6):2914–2926.

Bonney, T. (1885). Iii.—preliminary note on some traverses of the crystalline district of the central alps. *Geological Magazine*, 2(11):494–496.

Bousquet, R., Schmid, S., Zeilinger, G., Oberhänsli, R., Rosenberg, C., Molli, G., Robert, C., Wiederkehr, M., and Rossi, P. (2012). *Tectonic framework of the Alps= Carte tectonique des Alpes*. University_of_Basel.

Brouwer, F., Van De Zedde, D., Wortel, M., and Vissers, R. (2004). Late-orogenic heating during exhumation: Alpine ptt trajectories and thermomechanical models. *Earth and Planetary Science Letters*, 220(1-2):185–199.

Buiter, S. J., Babeyko, A. Y., Ellis, S., Gerya, T. V., Kaus, B. J., Kellner, A., Schreurs, G., and Yamada, Y. (2006). The numerical sandbox: comparison of model results for a shortening and an extension experiment. *Geological Society, London, Special Publications*, 253(1):29–64.

Burg, J.-P. and Gerya, T. (2005). The role of viscous heating in barrovian metamorphism of collisional orogens: thermomechanical models and application to the lepontine dome in the central alps. *Journal of Metamorphic Geology*, 23(2):75–95.

Burov, E. and Yamato, P. (2008). Continental plate collision, p–t–t–z conditions and unstable vs. stable plate dynamics: insights from thermo-mechanical modelling. *Lithos*, 103(1-2):178–204.

Dal Zilio, L., Kissling, E., Gerya, T., and van Dinther, Y. (2020). Slab rollback orogeny model: A test-of-concept. *Geophysical Research Letters*, page e2020GL089917.

Dal Zilio, L., van Dinther, Y., Gerya, T. V., and Pranger, C. C. (2018). Seismic behaviour of mountain belts controlled by plate convergence rate. *Earth and Planetary Science Letters*, 482:81–92.

Dewey, J., Helman, M., Knott, S., Turco, E., and Hutton, D. (1989). Kinematics of the western mediterranean. *Geological Society, London, Special Publications*, 45(1):265–283.

Dinther, Y. v. (2013). *Seismo-thermo-mechanical modeling of subduction zone seismicity*. ETH Zurich.

Duretz, T., de Borst, R., and Le Pourhiet, L. (2019). Finite thickness of shear bands in frictional viscoplasticity and implications for lithosphere dynamics. *Geochemistry, Geophysics, Geosystems*, 20(11):5598–5616.

Duretz, T. and Gerya, T. (2013). Slab detachment during continental collision: Influence of crustal rheology and interaction with lithospheric delamination. *Tectonophysics*, 602:124–140.

Duretz, T., Gerya, T., and Spakman, W. (2014). Slab detachment in laterally varying subduction zones: 3-d numerical modeling. *Geophysical Research Letters*, 41(6):1951–1956.

Duretz, T., Gerya, T. V., and May, D. A. (2011). Numerical modelling of spontaneous slab breakoff and subsequent topographic response. *Tectonophysics*, 502(1-2):244–256.

Duretz, T., Schmalholz, S., and Gerya, T. (2012). Dynamics of slab detachment. *Geochemistry, Geophysics, Geosystems*, 13(3).

Ellis, S. (1996). Forces driving continental collision: Reconciling indentation and mantle subduction tectonics. *Geology*, 24(8):699–702.

Evans, B. and Goetze, C. (1979). The temperature variation of hardness of olivine and its implication for polycrystalline yield stress. *Journal of Geophysical Research: Solid Earth*, 84(B10):5505–5524.

Faccenda, M., Gerya, T. V., and Chakraborty, S. (2008). Styles of post-subduction collisional orogeny: influence of convergence velocity, crustal rheology and radiogenic heat production. *Lithos*, 103(1-2):257–287.

Faccenda, M., Minelli, G., and Gerya, T. (2009). Coupled and decoupled regimes of continental collision: Numerical modeling. *Earth and Planetary Science Letters*, 278(3-4):337–349.

Fourel, L., Goes, S., and Morra, G. (2014). The role of elasticity in slab bending. *Geochemistry, Geophysics, Geosystems*, 15(11):4507–4525.

Gerbault, M. and Willingshofer, E. (2004). Lower crust indentation or horizontal ductile flow during continental collision? *Tectonophysics*, 387(1-4):169–187.

Gerya, T. (2015). Tectonic overpressure and underpressure in lithospheric tectonics and metamorphism. *Journal of Metamorphic Geology*, 33(8):785–800.

Gerya, T., Perchuk, L., and Burg, J.-P. (2008). Transient hot channels: perpetrating and regurgitating ultrahigh-pressure, high-temperature crust–mantle associations in collision belts. *Lithos*, 103(1-2):236–256.

Gerya, T. V. (2019). *Introduction to numerical geodynamic modelling*. Cambridge University Press, 2 edition.

Gerya, T. V. and Yuen, D. A. (2003). Characteristics-based marker-in-cell method with conservative finite-differences schemes for modeling geological flows with strongly variable transport properties. *Physics of the Earth and Planetary Interiors*, 140(4):293–318.

Gerya, T. V. and Yuen, D. A. (2007). Robust characteristics method for modelling multiphase visco-elasto-plastic thermo-mechanical problems. *Physics of the Earth and Planetary Interiors*, 163(1-4):83–105.

Gerya, T. V., Yuen, D. A., and Maresch, W. V. (2004a). Thermomechanical modelling of slab detachment. *Earth and Planetary Science Letters*, 226(1-2):101–116.

Gerya, T. V., Yuen, D. A., and Maresch, W. V. (2004b). Thermomechanical modelling of slab detachment. *Earth and Planetary Science Letters*, 226(1-2):101–116.

Graveleau, F., Malavieille, J., and Dominguez, S. (2012). Experimental modelling of orogenic wedges: A review. *Tectonophysics*, 538:1–66.

Handy, M. R., Schmid, S. M., Bousquet, R., Kissling, E., and Bernoulli, D. (2010). Reconciling plate-tectonic reconstructions of Alpine Tethys with the geological-geophysical record of spreading and subduction in the Alps. *EARTH-SCIENCE REVIEWS*, 102(3-4):121–158.

Ito, E., Akaogi, M., Topor, L., and Navrotsky, A. (1990). Negative pressure-temperature slopes for reactions formign mgsio3 perovskite from calorimetry. *Science*, 249(4974):1275–1278.

Katayama, I. and Karato, S.-i. (2008). Low-temperature, high-stress deformation of olivine under water-saturated conditions. *Physics of the Earth and Planetary Interiors*, 168(3-4):125–133.

Kissling, E. and Schlunegger, F. (2018). Rollback orogeny model for the evolution of the swiss alps. *Tectonics*, 37(4):1097–1115.

Liao, J. and Gerya, T. (2017). Partitioning of crustal shortening during continental collision: 2-d thermomechanical modeling. *Journal of Geophysical Research: Solid Earth*, 122(1):592–606.

Liao, J., Gerya, T., and Malusà, M. G. (2018). 3d modeling of crustal shortening influenced by along-strike lithological changes: Implications for continental collision in the western and central alps. *Tectonophysics*, 746:425–438.

Lombardi, D., Braunmiller, J., Kissling, E., and Giardini, D. (2008). Moho depth and poisson's ratio in the western-central alps from receiver functions. *Geophysical Journal International*, 173(1):249–264.

Luth, S., Willingshofer, E., Sokoutis, D., and Cloetingh, S. (2010). Analogue modelling of continental collision: Influence of plate coupling on mantle lithosphere subduction, crustal deformation and surface topography. *Tectonophysics*, 484(1-4):87–102.

Luth, S., Willingshofer, E., Sokoutis, D., and Cloetingh, S. (2013). Does subduction polarity changes below the alps? inferences from analogue modelling. *Tectonophysics*, 582:140–161.

Malusà, M. G., Anfinson, O. A., Dafov, L. N., and Stockli, D. F. (2016). Tracking adria indentation beneath the alps by detrital zircon u-pb geochronology: Implications for the oligocene–miocene dynamics of the adriatic microplate. *Geology*, 44(2):155–158.

Ratschbacher, L., Frisch, W., Linzer, H.-G., and Merle, O. (1991). Lateral extrusion in the eastern alps, part 2: structural analysis. *Tectonics*, 10(2):257–271.

Rosenberg, C. L., Berger, A., Bellahsen, N., and Bousquet, R. (2015). Relating orogen width to shortening, erosion, and exhumation during alpine collision. *Tectonics*, 34(6):1306–1328.

Rosenberg, C. L. and Kissling, E. (2013). Three-dimensional insight into central-alpine collision: Lower-plate or upper-plate indentation? *Geology*, 41(12):1219–1222.

Rudnick, R. and Taylor, S. (1987). The composition and petrogenesis of the lower crust: a xenolith study. *Journal of Geophysical Research: Solid Earth*, 92(B13):13981–14005.

Sandiford, M., Coblentz, D., and Schellart, W. P. (2005). Evaluating slab-plate coupling in the indo-australian plate. *Geology*, 33(2):113–116.

Schellart, W. P. and Moresi, L. (2013). A new driving mechanism for backarc extension and backarc shortening through slab sinking induced toroidal and poloidal mantle flow: Results from dynamic subduction models with an overriding plate. *Journal of Geophysical Research: Solid Earth*, 118(6):3221–3248.

Schlunegger, F. and Kissling, E. (2015). Slab rollback orogeny in the alps and evolution of the swiss molasse basin. *Nature communications*, 6:8605.

Schmid, S. M., Fügenschuh, B., Kissling, E., and Schuster, R. (2004). Tectonic map and overall architecture of the alpine orogen. *Eclogae Geologicae Helvetiae*, 97(1):93–117.

Schmid, S. M., Kissling, E., Diehl, T., van Hinsbergen, D. J., and Molli, G. (2017). Ivrea mantle wedge, arc of the western alps, and kinematic evolution of the alps–apennines orogenic system. *Swiss Journal of Geosciences*, 110(2):581–612.

Schmid, S. M., Pfiffner, O.-A., Froitzheim, N., Schönborn, G., and Kissling, E. (1996). Geophysical-geological transect and tectonic evolution of the swiss-italian alps. *Tectonics*, 15(5):1036–1064.

Singer, J., Diehl, T., Husen, S., Kissling, E., and Duretz, T. (2014). Alpine lithosphere slab rollback causing lower crustal seismicity in northern foreland. *Earth and Planetary Science Letters*, 397:42–56.

Sokoutis, D. and Willingshofer, E. (2011). Decoupling during continental collision and intra-plate deformation. *Earth and Planetary Science Letters*, 305(3-4):435–444.

Stern, R. J. and Gerya, T. (2018). Subduction initiation in nature and models: A review. *Tectonophysics*, 746:173–198.

Toussaint, G., Burov, E., and Jolivet, L. (2004). Continental plate collision: Unstable vs. stable slab dynamics. *Geology*, 32(1):33–36.

Turcotte, D. L. and Schubert, G. (2002). *Geodynamics*. Cambridge university press.

Van Dinther, Y., Gerya, T., Dalguer, L., Mai, P. M., Morra, G., and Giardini, D. (2013). The seismic cycle at subduction thrusts: Insights from seismo-thermo-mechanical models. *Journal of Geophysical Research: Solid Earth*, 118(12):6183–6202.

van Dinther, Y., Gerya, T., Dalguer, L. A., Corbi, F., Funiciello, F., and Mai, P. M. (2013). The seismic cycle at subduction thrusts: 2. dynamic implications of geodynamic simulations validated with laboratory models. *Journal of Geophysical Research: Solid Earth*, 118(4):1502–1525.

Van Dinther, Y., Mai, P. M., Dalguer, L., and Gerya, T. (2014). Modeling the seismic cycle in subduction zones: The role and spatiotemporal occurrence of off-megathrust earthquakes. *Geophysical Research Letters*, 41(4):1194–1201.

Van Hinsbergen, D. J., Torsvik, T. H., Schmid, S. M., Maţenco, L. C., Maffione, M., Vissers, R. L., Gürer, D., and Spakman, W. (2020). Orogenic architecture of the mediterranean region and kinematic reconstruction of its tectonic evolution since the triassic. *Gondwana Research*, 81:79–229.

Vigano, A. and Martin, S. (2007). Thermorheological model for the european central alps: brittle–ductile transition and lithospheric strength. *Terra Nova*, 19(5):309–316.

Vogt, K., Matenco, L., and Cloetingh, S. (2017). Crustal mechanics control the geometry of mountain belts. insights from numerical modelling. *Earth and Planetary Science Letters*, 460:12–21.

Vogt, K., Willingshofer, E., Matenco, L., Sokoutis, D., Gerya, T., and Cloetingh, S. (2018). The role of lateral strength contrasts in orogenesis: A 2d numerical study. *Tectonophysics*, 746:549–561.

von Hagke, C., Oncken, O., Ortner, H., Cederbom, C., and Aichholzer, S. (2014). Late miocene to present deformation and erosion of the central alps—evidence for steady state mountain building from thermokinematic data. *Tectonophysics*, 632:250–260.

Watts, A. and Burov, E. (2003). Lithospheric strength and its relationship to the elastic and seismogenic layer thickness. *Earth and Planetary Science Letters*, 213(1-2):113–131.

Wells, D. L. and Coppersmith, K. J. (1994). New empirical relationships among magnitude, rupture length, rupture width, rupture area, and surface displacement. *Bulletin of the seismological Society of America*, 84(4):974–1002.

Willingshofer, E. and Sokoutis, D. (2009). Decoupling along plate boundaries: Key variable controlling the mode of deformation and the geometry of collisional mountain belts. *Geology*, 37(1):39–42.